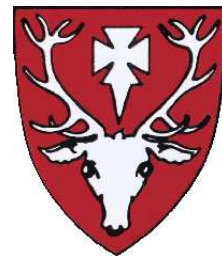


High P_T leptons and single W boson production at HERA

Katherine Korcsák-Gorzó

—
Hertford College
University of Oxford



Thesis submitted in partial fulfilment of the
requirements for the degree of Doctor of Philosophy.
University of Oxford, Michaelmas Term 2009

To Dean and my family.

Abstract

A search for isolated electrons and muons with high transverse momentum in events with large missing transverse momentum has been conducted. The results have been found to be compatible with the Standard Model expectations. The cross section for single W production has been measured and the total cross section in electron-proton collisions at HERA has been found to be $\sigma(ep \rightarrow eWX) = 0.93_{-0.23}^{+0.26}(\text{stat.}) \pm 0.08(\text{syst.})$ pb. The measurements are based on the complete available ZEUS data sets from the HERA I and II running periods taken between 1994–2007.

Acknowledgements

Research in high energy physics relies on the expertise and help of many people and so it is impossible to acknowledge the contribution of everyone. However, a DPhil requires a lot of support from individuals who dedicate themselves beyond their duties in order to educate the DPhil candidate and help to overcome problems in whichever shape they present themselves. It is these people whom I would like to thank in the following. I was very lucky to have worked with individuals who have not just advised and taught me but who also gave me their friendship.

My special thanks go to Professor Robin Devenish for his outstanding and enduring support over many years, both as a dedicated tutor who taught me as an undergraduate for years and as my DPhil supervisor who not just took on the task enthusiastically but also always ensured that my research was conducted under the best conditions possible. An excellent mentor, he provided invaluable advice along the way and always sacrificed his time for me whenever I asked for his help. He crucially ensured that at the end of my undergraduate studies I picked the right field of physics for my DPhil and that I persevered with that choice. For this I feel deeply grateful. Furthermore, it is thanks to him that this thesis was possible in the first place: He submitted my case to the particle physics department for financial support who upon his strong recommendation agreed to fund me for the duration of the DPhil project, covering not just my tuition fees but also my subsistence. It is thus to Professor Robin Devenish and the particle physics department of the University of Oxford that I fundamentally owe any future success that I derive from this degree.

The person who provided extensive help and support for my main analysis was James Ferrando who also educated me in the maintenance of the central tracking detector. The many useful discussions with him helped me to reign in the problems with the analysis along the way. But I would like to thank him especially for his never fading patience and for his reliably speedy help over all these years.

At the beginning of my DPhil, I worked on the alignment of the ZEUS microvertex detector using cosmic muon tracks. For that project, I would like to thank Takanori Kohno for providing me with his track fitting program and for many helpful discussions. My subsequent work using the laser alignment system of ZEUS benefited from the help of Grzegorz Grzelak who introduced me to the software framework. Roberto Carlin and Uli Koetz deserve special credit as their insight led me to the results of the laser alignment system, which in turn verified and explained the surprising results of the alignment based on cosmic muon tracks. Chris Youngman and Uwe Schneekloth provided me with the environmental information used to interpret the results of the laser alignment. The work of Mike Dawson and Tony Hanford in repairing the laser system and tracking down old documentation was invaluable and I am particularly indebted to them for the wisdom and optimism that they brought to the project.

As part of the group looking after the central detector, I am particularly thankful for the help of John Loizides and Tim Namssoo, who taught me a lot about physics and life beyond. It is thanks to them as well as Philip Allfrey, Mark Bell, Billy Dunne, Hartmut Stadie, Tom Danielson, Homer Wolfe and Trevor Stuart that my time at DESY was so enjoyable. In Oxford, I would like to thank Andy Powell, Cecilia Uribe-Estrada and Patrick Brockill for their friendship that kept me sane.

I would like to thank Sunil Patel for helping me to get started at DESY and for many interesting discussions about the wider world and Andrew Cottrell for the jolly spirit he brought to the group. Roman Walczak deserves credit for many interesting insights and

physics discussions. I am also grateful for a one-off grant from the Newby Trust at the beginning of my DPhil that helped me to cover part of the living expenses in my first year.

My very special thanks, however, I would like to dedicate to Dean who, with his love and support, helped me to complete this work and who enriched my life in many more ways I ever thought possible. I could never put into words the full extent of my appreciation, I can only hope to return his support throughout our life.

I would like to express my deepest gratitude to my family who through a long chain of events made (my life in the first place and subsequently) my academic life possible thanks to their never-ending efforts and self-sacrifice. I would like to apologise to my siblings, Ágnes and Péter, for my absence from their childhood and their teenage years due to my studies abroad. I am going to do my utmost to catch up with all the time that we spent apart.

My thanks to you all.

Contents

1	Introduction	1
2	Theoretical overview	5
2.1	The Standard Model	5
2.2	Quark-Parton Model and kinematic variables	7
2.3	Deep inelastic scattering	8
2.3.1	Neutral Current	9
2.3.2	Charged Current	10
2.4	Photoproduction	12
2.5	QED Compton	13
2.6	Lepton pair production	14
2.7	Single W production	14
3	The ZEUS experiment at HERA	18
3.1	HERA collider	18
3.1.1	Bunch structure	20
3.1.2	The pre-accelerator system	20
3.1.3	Run periods and upgrade	21
3.1.4	Beam polarisation	23
3.1.5	Transverse polarimeter	25
3.1.6	Longitudinal polarimeter	25
3.2	ZEUS detector	26
3.2.1	Calorimeter	27
3.2.2	Presampler	29
3.2.3	Central Tracking Detector	29
3.2.4	The microvertex detector	31
3.2.5	Luminosity monitoring	32
3.2.6	Background veto system	34
3.2.7	Trigger	34
3.2.8	Offline event reconstruction	37
4	Monte Carlo simulation	38
4.1	Simulation procedure	38
4.2	QED radiation	40
4.3	QCD radiation and hadronisation	41
4.4	Single W production	42
4.4.1	NLO reweighting	45
4.5	Neutral and Charged Current sample	45

4.6	Lepton pair production	50
4.7	Photoproduction	52
4.8	Monte Carlo corrections	52
5	Data sets, event reconstruction and backgrounds	53
5.1	Data sets	53
5.2	Event reconstruction	53
5.2.1	Electron identification	54
5.2.2	Muon identification	55
5.2.3	Vertex reconstruction	55
5.2.4	Event variables	56
5.2.5	Jet finding	59
5.2.6	Reconstruction methods for DIS processes	59
5.3	Corrections	63
5.3.1	Calorimeter noise	64
5.3.2	Electron corrections	64
5.4	Hadronic corrections	65
5.5	Backgrounds	68
5.5.1	Cosmic muons	68
5.5.2	Beam-gas interactions	70
5.5.3	Halo-muons	70
6	Isolated leptons and single W boson production	71
6.1	Event selection	72
6.2	Results of the isolated lepton search	79
6.3	Cross section measurement	87
6.3.1	Cross sections from background subtraction	88
6.3.2	Cross sections from the likelihood method	88
6.3.3	Cross sections from the likelihood method with Gaussian smearing	89
6.4	Systematic uncertainties	90
6.4.1	Luminosity uncertainty	92
6.4.2	Energy scale	92
6.4.3	NLO uncertainty on single W boson production	92
6.4.4	Background uncertainties	93
6.4.5	Muon finding efficiency	99
7	Conclusions	109

Chapter 1

Introduction

The state of knowledge in elementary particle physics is incorporated in the theoretical framework that is known as the *Standard Model*. It has been developed over the course of the 20th century with the aim of explaining experimental observations whilst achieving mathematical consistency. Particle physics can be said to have started in the late 19th century with the first discovery of an elementary particle, the electron, by J.J. Thomson in 1897 [1] whose existence was suggested by G.J. Stoney in 1891 [2]. It culminated in the year 2000 with the first direct detection of the tau-type neutrino, ν_τ , by the DONUT experiment [3]. The latter is the last new type of elementary particle to have been observed to date.

One particle that is theoretically part of the Standard Model still remains to be discovered: the Higgs boson. It is the particle that is assumed to provide a mechanism, through which the gauge bosons (the elementary particles that propagate the forces of nature) acquire mass. This is important because in the Standard Model all elementary particles are otherwise massless to accommodate the symmetry requirements that form the foundations of the model. One of the main goals of the new Large Hadron Collider (LHC) at CERN is to find evidence for this important piece of the Standard Model.

Particle physics will not be finalised with the discovery of the Higgs boson since there are theoretical considerations and observations from cosmology that indicate that the Standard Model is incomplete in that it cannot describe all phenomena to infinitely large energies. Furthermore, the model does not explain e.g. individual masses of the elementary particles and their mass hierarchy that stretches from the mass of the neutrinos at a few eV/c^2 ¹ to the top quark mass of $171 \text{ GeV}/c^2$ [4]. So, it is hoped that in addition to the discovery of the Higgs boson, the LHC might provide evidence for phenomena beyond the Standard Model exploring the hitherto unachieved energy regime of 14 TeV.

Despite all its shortcomings, the Standard Model has proved very resilient over the past 30 years. The only major modification it had to undergo from its original form was to accommodate non-zero neutrino masses that had to be incorporated after the discovery of neutrino oscillations. These were first detected in the 1960's but only conclusively proved by the SNO

¹Electron Volt (eV) is a unit of energy that is defined as the amount of kinetic energy acquired by a free electron in an electrostatic potential of one Volt. In particle physics the most common uses of this unit are in Mega electron Volt ($\text{MeV} = 10^6 \text{ eV}$) and Giga electron Volt ($\text{GeV} = 10^9 \text{ eV}$).

experiment in 2001 [5]. Apart from these exceptions, every high energy experiment to date has contributed to testing the Standard Model's predictions and measuring its parameters but all failed to find evidence for processes, in which it breaks down.

The HERA collider in Germany was one of the last high energy accelerators to operate before the start of the LHC. Therefore, the physics program of the experiments at HERA was mainly defined by precision measurements of the Standard Model and its known processes. However, several searches were also conducted for signatures of new physics that would have been the first hints of what the LHC might uncover. This thesis incorporates both these aspects.

The initial motivation for the work presented here, was a signal that could have been an indication of physics beyond the Standard Model: Events containing isolated leptons and a large imbalance in transverse momentum arose a lot of interest at HERA when the H1 experiment observed an excess of such events above the Standard Model expectation in its HERA I data sets [6, 7]. Figure 1.1 shows the plot from the search for isolated electrons and muons published by H1 in 2003 [7]. The excess can be seen mainly at large hadronic transverse momentum, labelled P_T^X , in the bottom left plot.

An unknown physics process could have contributed the additional events, e.g. if it produced a new particle, which did not interact noticeably within the detector. This particle would then have carried away transverse momentum that would appear to be 'missing' and thus create the large momentum imbalance observed in the transverse plane. One possible scenario that was put forward, amongst others, stipulated the existence of R-parity violating Supersymmetry and explained the excess observed by H1 with the production of single stop particles, the supersymmetric partners of the top quark [8–14].

The main Standard Model process that gives rise to such events is the production of single W bosons. As a consequence of the large rest mass of the W , these bosons are created closer to rest in the lab frame of the experiment than most other particles. Therefore, the subsequent decay of the W is observed almost in its rest frame and the daughter particles can have large transverse momenta. When a W boson decays leptonically the neutrino escapes undetected, thereby giving rise to the large 'missing' transverse momentum (denoted P_T^{miss}), whilst the other lepton is observed as isolated from the rest of the event.

Searches for isolated leptons have been conducted at ZEUS, but failed to confirm the excess seen by the H1 experiment [15, 16]. However, the search for tau leptons observed two events in the data taken until 2000 where only 0.2 ± 0.05 were expected from the simulation of the Standard Model expectation [17]. In 2006, the H1 Collaboration published a search for isolated tau leptons based on the data sets taken until 2000 but did not see an excess of those type of events [18].

The analysis in this thesis, i.e. my own work, is presented in Chapters 6–7. It is based on the complete available ZEUS data sets 1994–2007 and aims to provide the final outcome of the search for events containing isolated electrons and muons with large P_T^{miss} , as seen by the ZEUS detector. Furthermore, I used the results of this search to measure the single W boson production cross section. As mentioned above, the decay of single W bosons is the dominant Standard Model process that gives rise to events selected by the search. An accurate knowledge of the production cross section is, therefore, a vital pre-requisite for the detection of new physics processes as it forms a major background in such exotic searches.

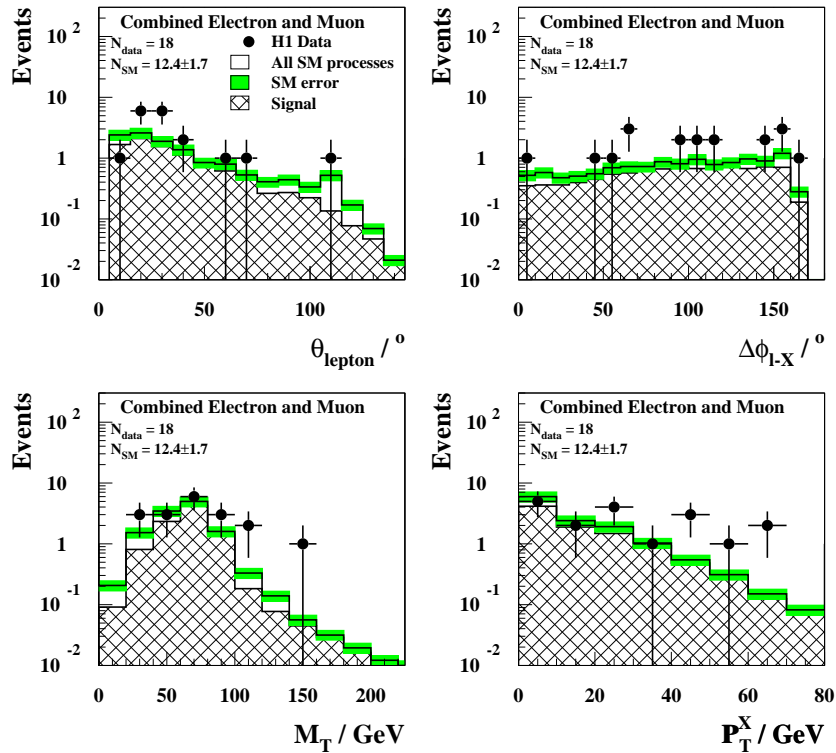


Figure 1.1: Results of the H1 experiment's search for isolated leptons as published in 2003 [7]. The variables shown are the polar angle of the scattered lepton (top left), the difference in azimuthal angle between the lepton and the hadronic system (top right), the transverse mass (bottom left, see Equation 5.18 for the definition) and the hadronic transverse momentum (bottom right).

The results of the search and the cross section measurement presented here have been published by the ZEUS Collaboration in 2008 [19], whereby the analysis presented in this thesis formed one of the main contributions.

The preceding chapters summarise previous results (Chapter 1), introduce theoretical foundations (Chapter 2) as well as the experimental setup (Chapters 3, the simulations 4) and quantities (Chapter 5) used for the analysis.

The simulated data was generated and certified centrally by the ZEUS Structure Functions and Exotics Group. The real data were taken in a large collaborative effort by the members of ZEUS over the lifetime of the experiment. The data-taking was divided into three shifts per day and was conducted by a shift leader and a deputy with the aid of on-call experts who were available in case of problems. I contributed to this effort as a shift leader as well as an on-call expert for the Central Tracking Detector (see Section 3.2.3) during the years 2005–2007.

Throughout this thesis a set of units (called *natural units* in particle physics) is used, such that equations can be written with $\hbar = c = 1$, where \hbar is Planck's constant and c is

Chapter 1

the speed of light. Using this convention, mass and energy are measured in the same units.

Chapter 2

Theoretical overview

The HERA collider is often called a 'Standard Model machine' reflecting that during its operational period HERA probed many aspects of the Standard Model (SM) of particle physics and enriched our knowledge with many high-precision measurements. Constrained by its centre-of-mass collision energy and its luminosity performance, it did not find any evidence for new physics phenomena beyond the SM, which to this day remains the only viable model of particle physics. The following sections give a brief outline of the Standard Model, the main physics processes at HERA, single W boson production and other SM processes that give rise to physics background in the studies presented in this thesis.

2.1 The Standard Model

The Standard Model of particle physics describes the properties and interactions of the elementary particles of nature. It is based on renormalisable gauge theories, in which forces are mediated by the exchange of virtual gauge bosons that are a consequence of the local gauge symmetries of the relevant fields. The forces of nature possess symmetries that determine their nature and that can be described by mathematical groups¹: the strong force (mediated by 8 gluons) obeys the symmetry of the $SU(3)_C$ group and the electromagnetic and weak forces (mediated by the photon, W^\pm and Z bosons) are unified under $SU(2)_L \times U(1)_Y$, which represents the so called *electroweak* force. The SM lacks a description of gravity.

With regards to the masses of the gauge bosons, nature is highly asymmetric as gluons and photons are massless as in both cases the gauge symmetry is exact ($SU(3)_C$ and $U(1)$, respectively), whereas, the W^\pm and Z bosons are very heavy at 80 GeV and 91 GeV [4], respectively. The Higgs mechanism is thought to be responsible for the spontaneous breaking of the electroweak symmetry, in which the weak gauge bosons acquire their mass. In this theoretical framework the Higgs field permeates the universe and is also responsible to give mass to all other fundamental particles via the exchange of the spinless Higgs boson. Despite

¹ $U(n)$ is the group comprising all unitary $n \times n$ matrices, whereas, $SU(n)$ represents the group of all unitary $n \times n$ matrices with a determinant of 1. The subscripts are C for colour, the charge the strong force couples to, Y for hypercharge, the sum of the baryon and the strangeness quantum numbers, and L , which indicates that the weak force couples only left-handed fermions and right-handed anti-fermions

the fact that the Higgs boson is generally considered to be part of the Standard Model, it is the last elementary particle of the model that has so far eluded detection [4].

In addition to the gauge bosons that mediate the elementary forces, the SM also incorporates all known elementary fermions, namely, the quarks and leptons as shown in Table 2.1. All quarks and leptons are fermions, which means that they are particles with half-integer spin that thus obey Fermi-Dirac statistics. In contrast, the gauge bosons have integer spin and are governed by Bose-Einstein statistics. All SM fermions have a corresponding anti-particle that has opposite quantum numbers but the same mass.

Grouping the fermions into generations reveals further patterns: The lepton pairs combine a particle with electromagnetic charge $Q_{EM} = -1$ with a much lighter neutral neutrino, whereas generations of quarks pair fermions with $Q_{EM} = +2/3$ and $-1/3$. Furthermore, a mass hierarchy becomes apparent as the mass of the particles increases with every generation for both leptons and quarks, thereby keeping the heaviest particle in the same half of the generation - with the possible exception of the u and d quarks (see Tab. 2.2). Whilst being the exception to that rule, the two lightest quarks are so close in mass that they can be described by their own approximate symmetry that forms the basis of *isospin*. The generation structure plays a particularly important role for the weak force, in which only leptons within a generation can couple directly. That also holds for the quarks with the modification that the weak force couples within generations that are related by the *CKM matrix* to those seen by the strong and electromagnetic force.

As a consequence of the symmetry properties of the strong force, all colour states are confined to an overall colourless state, known as a colour-singlet. Hence, quarks only occur in combinations that allow them to be overall colourless: $q\bar{q}$ are called *mesons*, whereas, qqq are referred to as *baryons* and both fall into the category of *hadrons*. Single free quarks do not occur in nature due to the confinement property of the strong force. In practice, this means that if a single quark inside a hadron exchanges energy and momentum in an interaction with another particle (e.g. during a high-energy scattering with a lepton), such that the quark begins to separate from its partners inside the hadron then the energy stored in the field between the quarks increases rapidly with separation distance until it becomes large enough that $q\bar{q}$ pairs can be created from this field energy. These additional particles form hadrons until all energy is used up and all quarks and anti-quarks are again bound into hadrons. The result of such a hard interaction is thus a large number of hadrons that

Fermions	Generations			Q_{EM}	Q_C	$I_W(f_L)$
	I	II	III			
Quarks	$\begin{pmatrix} u \\ d \end{pmatrix}$	$\begin{pmatrix} c \\ s \end{pmatrix}$	$\begin{pmatrix} t \\ b \end{pmatrix}$	$\begin{matrix} +\frac{2}{3} \\ -\frac{1}{3} \end{matrix}$	R,G,B	$\begin{matrix} +\frac{1}{2} \\ -\frac{1}{2} \end{matrix}$
Leptons	$\begin{pmatrix} e \\ \nu_e \end{pmatrix}$	$\begin{pmatrix} \mu \\ \nu_\mu \end{pmatrix}$	$\begin{pmatrix} \tau \\ \nu_\tau \end{pmatrix}$	$\begin{matrix} -1 \\ 0 \end{matrix}$	0	$\begin{matrix} -\frac{1}{2} \\ +\frac{1}{2} \end{matrix}$

Table 2.1: The three generations of quarks and leptons with their corresponding quantum numbers of electromagnetic charge (Q_{EM}), strong 'colour' charge (Q_C) and weak isospin (I_W). The values of the latter stated above apply to the left-handed component of the fermions, whereas the right handed component carries $I_W = 0$.

Fermions	Mass [GeV]	Fermions	Mass [GeV]	Fermions	Mass [GeV]
u	$\mathcal{O}(10^{-3})$	c	1.3	t	171.2
d		s	0.1	b	4.2
e	5×10^{-4}	μ	0.1	τ	1.7
ν_e	$< \mathcal{O}(10^{-6})$	ν_μ	$< \mathcal{O}(10^{-4})$	ν_τ	$< \mathcal{O}(10^{-2})$
Bosons	Mass [GeV]	Bosons	Mass [GeV]	Bosons	Mass [GeV]
γ, g	0	W^+, W^-	80	Z^0	91

Table 2.2: The mass of the quarks, fermions and bosons.

appear in form of a *jet*.

With these foundations the SM explains most of subatomic physics and all of the elementary particles known so far.

2.2 Quark-Parton Model and kinematic variables

In the Quark-Parton Model (QPM) the proton is made up of many point-like partons that move independently inside the proton without interacting. The electron-proton interaction then occurs between these scattering centres and the lepton probe, so that the overall interaction cross section is the total sum of these incoherent scatters.

The interaction is shown diagrammatically in Fig. 2.1, for which the following kinematic variables can be defined:

$$Q^2 = -q^2 = -(k - k')^2 \quad (2.1)$$

$$x = \frac{-q^2}{2p \cdot q} \quad (2.2)$$

$$y = \frac{p \cdot q}{p \cdot k} \quad (2.3)$$

$$s = (k + p)^2, \quad (2.4)$$

where k , k' and p are the four-momenta of the incoming and the scattered beam electron and of the incoming proton, respectively. The difference between k and k' gives q , which is the four-momentum of the exchanged virtual boson. The quantity s is the square of the centre of mass energy and therefore fixed at HERA (see Section 3.1). The variable x represents the fraction of the proton momentum carried by the interacting parton and y is a measure of the fractional energy loss of the lepton probe in the fixed target frame; hence, their values are in the range of $0 \leq x, y \leq 1$. The above variables can all be related through:

$$Q^2 = sxy, \quad (2.5)$$

, thus, only two of the variables are independent. The kinematic variables can be re-expressed in terms of quantities measured directly by the experiment (and from these the equation for

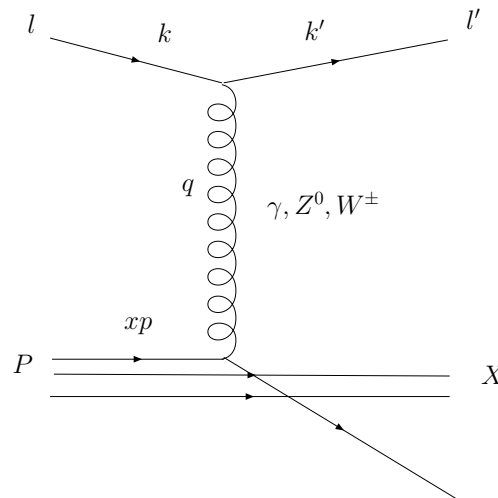


Figure 2.1: Electron-proton interaction in the Quark-Parton Model.

x can be obtained using Equation 2.5):

$$s = 4E_p E_e, \quad (2.6)$$

$$Q^2 = 2E_e E'_e (1 + \cos \theta_e), \quad (2.7)$$

$$y = 1 - \frac{E'_e}{2E_e} (1 - \cos \theta_e), \quad (2.8)$$

where E_p, E_e (E'_e) are the energies of the proton and the electron before (after) the interaction and θ_e is the polar angle of the scattered lepton measured relative to the z-axis defined by the incident proton direction. From the last equation one can see that, for a given E'_e , y is related to the scattering angle of the lepton such that high y events occur when the incident lepton is scattered backwards along the z-direction. Alternatively, high y events can occur when $E'_e \ll E_e$ due to which y is sometimes referred to as the inelasticity of the proton system.

As can be seen from Equation 2.1, Q^2 is a measure of the invariant mass squared of the exchanged virtual boson. It is also a measure of the resolving power of the electron probe: The higher the value of Q^2 the smaller the structure that is probed. At HERA, values up to $Q^2 \approx 40\,000 \text{ GeV}^2$ are measured. Using Q as the energy scale in Heisenberg's uncertainty principle, the corresponding length scale that is probed is obtained as $\lambda \approx \hbar c / \sqrt{Q^2} \approx 10^{-18} \text{ m}$. Comparing this to the size of a proton, which is about 10^{-15} m , it becomes clear that proton sub-structure plays an important role for the measurements at HERA.

2.3 Deep inelastic scattering

Deep inelastic scattering (DIS) refers to electron-proton interactions at sufficiently large Q^2 to probe the sub-structure inside the proton (hence 'deep') and to break up the proton (hence 'inelastic') by transferring enough four-momentum to one of its constituent quarks so that it separates from the proton. Due to the nature of QCD, single quarks cannot exist freely

and therefore, the quark that is ‘knocked out’ in a DIS process ends up inside a meson or baryon and the energy involved in removing it from the proton produces a large number of additional hadrons. The scattered quark is thus observed as a jet.

Deep inelastic scattering consists of two processes, Neutral Current (NC) and Charged Current (CC), explained in the following sections.

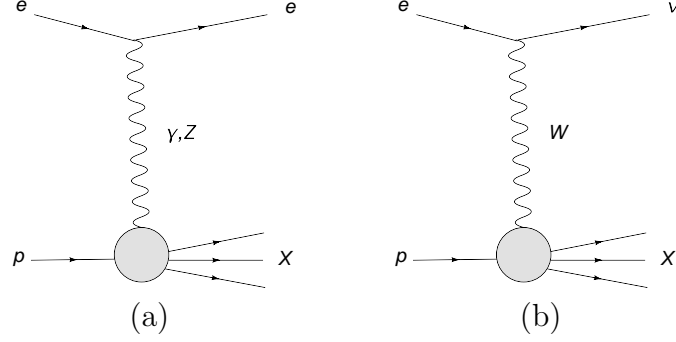


Figure 2.2: Deep inelastic scattering via (a) Neutral Current and (b) Charged Current.

2.3.1 Neutral Current

Neutral Current, shown in Fig. 2.2a, is the process $e^\pm p \rightarrow e^\pm X$, where X represent the hadronic final state. It can proceed via the exchange of a photon or a Z^0 . The double differential cross section for NC is [20–22]:

$$\frac{d^2\sigma_{NC}(e^\pm p)}{dx dQ^2} = \frac{2\pi\alpha^2}{xQ^4} \left(Y_+ \tilde{F}_2(x, Q^2) \mp Y_- x\tilde{F}_3(x, Q^2) - y^2 \tilde{F}_L(x, Q^2) \right), \quad (2.9)$$

where α is the electromagnetic fine structure constant and \tilde{F}_2 , \tilde{F}_3 and \tilde{F}_L are *generalised structure functions*. The variables Y_\pm are given by:

$$Y_\pm = 1 \pm (1 - y)^2 \quad (2.10)$$

The term containing \tilde{F}_L is small (zero in the QPM) and only contributes at large values of y due to the y^2 coefficient, therefore, it can be neglected in the following. The remaining generalised structure functions are given by:

$$\tilde{F}_2 = F_2^\gamma - (v_e - P_e a_e) \chi_Z F_2^{\gamma Z} + (v_e^2 + a_e^2 - 2 P_e v_e a_e) \chi_Z^2 F_2^Z, \quad (2.11)$$

$$x\tilde{F}_3 = -(a_e - P_e v_e) \chi_Z x F_3^{\gamma Z} + (2 v_e a_e - P_e (v_e^2 + a_e^2)) \chi_Z^2 x F_3^Z, \quad (2.12)$$

where $v_e = -1/2 + 2 \sin^2 \theta_W$ and $a_e = -1/2$ are the vector and axial vector couplings of the electron to the Z (with θ_W representing the Weinberg angle) and P_e is the polarisation of the lepton probe calculated from the numbers of right- and left-handed leptons in the beam, given by N_R and N_L , respectively:

$$P_e = \frac{N_R - N_L}{N_R + N_L} \quad (2.13)$$

The generalised structure functions depend on the terms F_2^γ , F_2^Z and $F_2^{\gamma Z}$ (and similarly for F_3), which represent the contributions from pure photon and pure Z exchange and the γ - Z interference. At leading order, these terms can be expressed in terms of the (anti-)quark density functions $\langle \bar{q} \rangle(x, Q^2)$ inside the proton:

$$F_2(x, Q^2) = \sum_f A_f x (q_f(x, Q^2) + \bar{q}_f(x, Q^2)) , \quad (2.14)$$

$$xF_3(x, Q^2) = \sum_f B_f 2x (q_f(x, Q^2) - \bar{q}_f(x, Q^2)) , \quad (2.15)$$

with the sum running over the quark flavours f and using different coefficients A_f , B_f for the processes involving γ , Z and γ - Z interference:

$$F_2^\gamma : A_f = e_q^2 , \quad F_2^{\gamma Z} : A_f = 2 e_q v_q , \quad F_2^Z : A_f = v_q^2 + a_q^2 \quad (2.16)$$

$$xF_3^\gamma : B_f = e_q^2 , \quad xF_3^{\gamma Z} : B_f = 2 e_q v_q , \quad xF_3^Z : B_f = v_q^2 + a_q^2 \quad (2.17)$$

This uses the electric charge (e_f), as well as the vector (v_f) and axial vector (a_f) couplings of quark flavour f to the Z .

In Equations 2.11 and 2.12, the contributions involving Z exchange are scaled by the propagator term:

$$\chi_Z = \frac{1}{\sin^2 2\theta_W} \frac{Q^2}{M_Z^2 + Q^2} , \quad (2.18)$$

with $1/\sin^2 2\theta_W \approx 1.4$. Noting that the $\gamma - Z$ interference term depends linearly on χ_Z , whereas it enters the term for pure Z exchange quadratically, it can be seen that F_2^γ dominates the cross section in the region of $Q^2 \ll M_Z^2$, with pure Z exchange increasing its contribution with higher Q^2 . The interference term and the pure Z exchange become comparable in size when $\chi_Z \approx 1$, i.e. at $Q^2 = M_Z^2/0.4 \approx 20\,000 \text{ GeV}^2$. Above these values the pure Z is the largest contribution.

The typical experimental signature of Neutral Current events is a scattered electron, as well as a jet and the proton remnant, whereby the latter two are detected in the forward region. Furthermore, the transverse momentum in the event is balanced in the transverse plane.

2.3.2 Charged Current

Charged Current, shown in Fig. 2.2b, is the process $e^\pm p \rightarrow (\bar{\nu}) X$, where X represent the hadronic final state. It proceeds via the exchange of W^+ or W^- bosons, due to which the cross section depends strongly on the polarisation of the lepton beam as can be seen in the expression for the double differential cross section [23]:

$$\frac{d^2\sigma^{\text{CC}}(e^\pm p)}{dx dQ^2} = (1 \pm P_e) \frac{G_F^2}{2\pi x} \frac{M_W^2}{(Q^2 + M_W^2)^2} (Y_+ F_2^{\text{CC}} \mp Y_- x F_3^{\text{CC}} - y^2 F_L^{\text{CC}}) , \quad (2.19)$$

where G_F is the weak coupling constant, M_W is the mass of the W boson and F_2^{CC} , F_L^{CC} and xF_3^{CC} are the CC structure functions of the proton. The variables Y_\pm are defined in

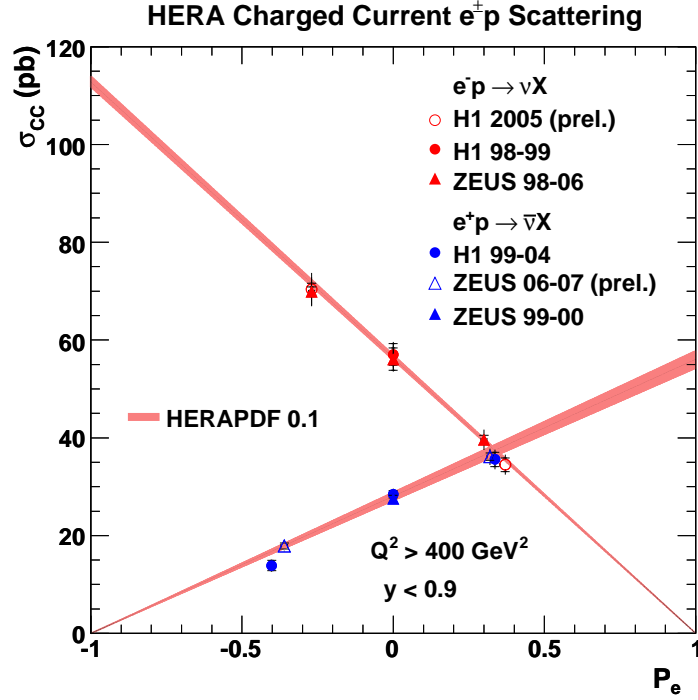


Figure 2.3: Measurements with the ZEUS and H1 detectors of the Charged Current cross section with e^+p (blue) and e^-p (red) data versus lepton beam polarisation P_e in the region of $y < 0.9$ and $Q^2 > 400 \text{ GeV}^2$ [24]. The straight bands indicate the corresponding SM prediction and the uncertainty on it from the parton density functions.

Equation 2.10. The term containing F_L^{CC} is small and its contribution is suppressed by the y^2 factor, so is neglected in the following. The term $(1 \pm P_e)$ implies that the cross section becomes zero for $e^\pm p$ interactions when the beam polarisation becomes $P_e = \mp 1$. This is a consequence of the weak interaction that couples W bosons only to left-handed particles and right handed anti-particles. The measurements of the CC cross section confirm the linear dependence on the lepton beam polarisation, as can be seen in Fig. 2.3.

Simplifying the equation by defining the *reduced cross section*,

$$\tilde{\sigma}(e^\pm p) = \left[\frac{G_F^2}{2\pi x} \frac{M_W^2}{(Q^2 + M_W^2)^2} \right]^{-1} \frac{d^2 \sigma^{\text{CC}}(e^\pm p)}{dx dQ^2}, \quad (2.20)$$

the cross section can be expressed, at leading order, in terms of the parton density functions of the proton, as follows:

$$\tilde{\sigma}(e^+p) = x [(\bar{u} + \bar{c}) + (1 - y)^2(d + s)] \quad (2.21)$$

$$\tilde{\sigma}(e^-p) = x [(u + c) + (1 - y)^2(\bar{d} + \bar{s})] \quad (2.22)$$

Charged Current events are characterised by missing transverse momentum observed in the event that is due to the final state neutrino escaping the detector. The large mass of the exchanged W boson in CC events suppresses them at low Q^2 relative to NC events, since the latter can proceed via photon exchange in that regime. However, in the region $Q^2 > M_W^2$,

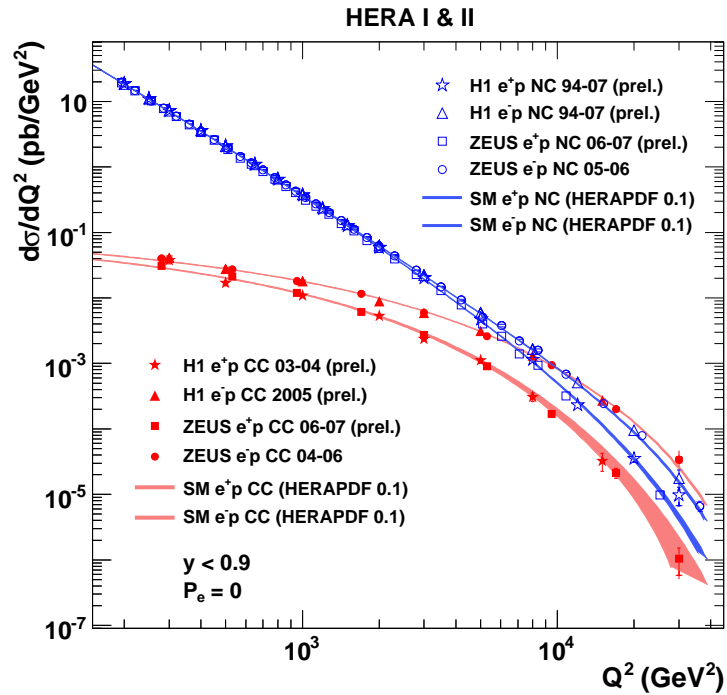


Figure 2.4: Measurements from the ZEUS and H1 detectors of the Neutral Current (blue) and Charged Current (red) differential cross sections $d\sigma/dQ^2$ versus Q^2 in the region of $y < 0.9$ [24]. The curves indicate the corresponding SM prediction.

Charged and Neutral Current have a similar cross section, see Fig. 2.4, as a consequence of electroweak unification.

The typical experimental signature of Charged Current is a jet and the proton remnant in the forward region of the detector that are not balanced in the transverse plane, as can be seen in the transverse plane (see Fig. 2.5).

2.4 Photoproduction

The term photoproduction (PHP) refers to electron-proton interactions in the limit of $Q^2 \approx 0$, i.e. where the exchanged photon is quasi-real or close to being *on-shell*. These interactions at very low Q^2 result in an electron scattering angle, θ_e , close to 180° (see Equation 2.7). Experimentally, these events were thus characterised by the absence of the scattered beam electron in the main ZEUS detector as it escaped through the rear beampipe.

Photoproduction interactions dominated the electron-proton interactions at low Q^2 . Most of these events contained final state particles with very low transverse energies, however, hard interactions could also occur. The experimental signature of hard PHP interactions were, typically, two back-to-back jets with large transverse energies. Photoproduction can be categorized into direct or resolved processes.

In direct PHP, the entire photon energy is involved in the hard scatter and the photon

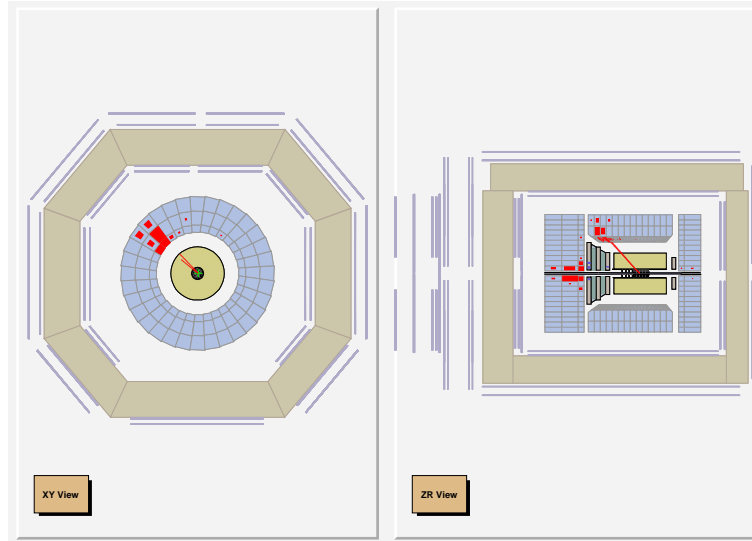


Figure 2.5: A typical Charged Current event measured by ZEUS.

can be treated as point-like for the interaction. Two Feynman diagrams contribute at leading order: QCD Compton, shown in Fig. 2.6a, and boson-gluon fusion, shown in Fig. 2.6b. At leading order, the final state thus consists of two jets, the scattered beam electron and the proton remnant.

In resolved PHP, the photon converts into a $q\bar{q}$ pair and one of these particles is subsequently involved in the hard sub-process. Hence, only a fraction of the initial photon four-momentum is available for the interaction. The second parton of the photon gives rise to additional hadronic deposits, which are referred to as the ‘photon remnant’. At leading order, the final state of resolved PHP consists of two jets, as well as the scattered electron and the proton remnant.

Finally, it should be noted that at higher orders, the distinction between direct and resolved PHP is no longer clearly defined.

2.5 QED Compton

In the QED Compton (QEDC) process, $ep \rightarrow e'\gamma p$ (shown in Fig. 2.7), the electron radiates a hard photon and, as a consequence, both the scattered electron and the photon can have large transverse momenta. This can result in QED Compton events mimicking the signature of DIS events. This can occur, even though QEDC (like PHP, discussed above) peaks at $Q^2 \approx 0$, since using the QEDC-scattered electron without the associated photon for calculating the event kinematics can reconstruct the event at high Q^2 .

Hence, QEDC processes contribute to event selections designed to pick out Neutral Current and thus, they played a role in the study of the DIS background, described in Section 6.4.4. However, they did not affect the search for single W bosons due to the requirement on large missing transverse momentum (see Section 6.1) that rejected QEDC events.

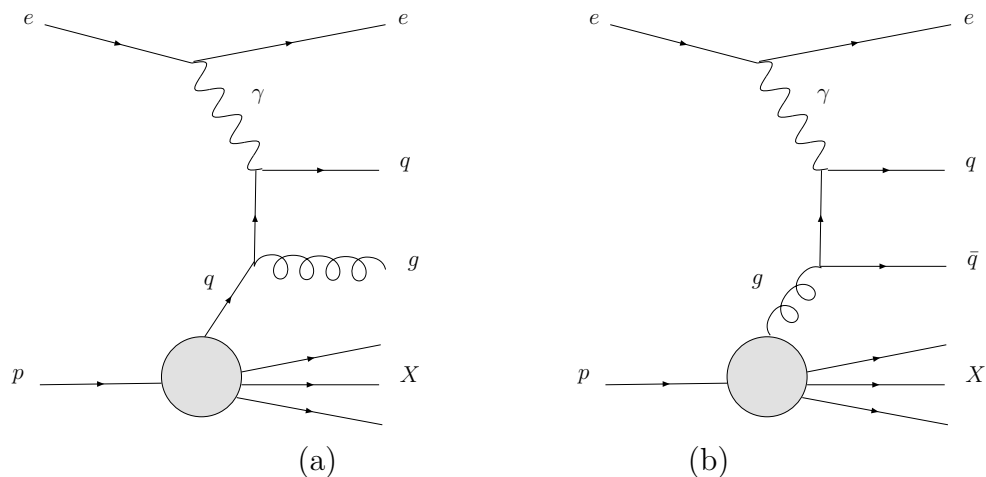


Figure 2.6: Feynman diagrams of Photoproduction: (a) QCD Compton process, (b) boson-gluon fusion.

2.6 Lepton pair production

Lepton pair production can proceed via two mechanisms. The first is the Bethe-Heitler process, in which a photon, radiated off the beam electron, interacts with a photon from the proton to produce a lepton pair, as shown in Fig. 2.8a. Events of this type dominate the total lepton pair production cross section² of about 120 pb. Their main signature is a pair of oppositely charged, back-to-back leptons. Furthermore, three different cases can be distinguished: In *elastic* interactions the proton stays intact, whereas, in a *quasi-elastic* process the proton is excited and decays predominantly to pions and a nucleon. *Inelastic* scatter breaks up the proton producing a large number of hadrons and if the momentum transfer to the beam electron is sufficiently high, the scattered electron falls into the acceptance of the main detector.

The second type of interaction amounts to less than 1% of the total cross section [25] and is formed by Compton-like events, in which the beam electron radiates a photon or a Z boson that converts to an l^+l^- pair, shown in Fig. 2.8b. This type of process is also characterised by two leptons with opposite charge. However, due to the production mechanism via the Z boson, the cross section for these events also peaks at the invariant mass of the Z in addition to the peak at low invariant masses.

2.7 Single W production

Within the Standard Model events containing isolated leptons and large missing transverse momentum are the signature of single W boson production where the W subsequently decays via the leptonic channel to an electron, muon or to a (leptonically decaying) tau and the

²The cross section is quoted for the case that at least one of the leptons falls into the acceptance of the ZEUS detector and has a transverse momentum above 5 GeV. At lower transverse momenta, the cross section increases rapidly.

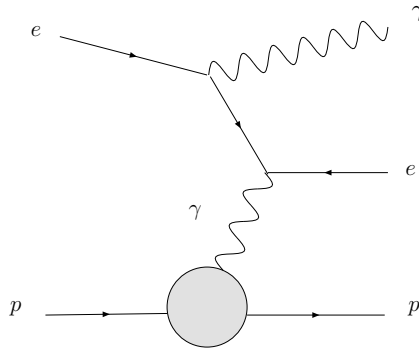


Figure 2.7: The QED Compton process

corresponding neutrino. As a consequence of the large rest mass of the W , both daughter leptons can be produced with a large transverse momentum. In these events, the neutrino creates the missing transverse momentum by escaping undetected.

Single W boson could be produced at HERA in Neutral or Charged Current interactions, according to:

$$e^\pm p \rightarrow e^\pm W^\pm X, \quad (2.23)$$

$$e^\pm p \rightarrow (\bar{\nu}) W^\pm X, \quad (2.24)$$

respectively, where X represents the hadronic final state. The latter process contributes only about 5% to the total W production cross section and therefore, the following discussion focuses on the Neutral Current mechanism. Events of type $e, p \rightarrow e, Z(\rightarrow \nu\nu) X$ can imitate single W production as they contain an isolated electron and large missing transverse momentum, however, the cross section is less than 3% of the single W production cross section, as calculated by EPVEC [26], and therefore this process can be neglected.

At leading order, single W production can be described by the Feynman diagrams shown in Fig. 2.9 [26]. The dominant diagrams are (a) and (b), in which the W boson is radiated from an initial or final state quark line, respectively. This is due to the dependence of the cross section on a term $Q^4/(Q^2 - M_W^2)^2$ introduced by the W boson propagator. In the integral over the four-momenta of the final state particles, this term diverges at $Q^2 = M_W^2$, which means that there is a large contribution to the cross section from diagrams (a) and (b) in which the W boson is on mass-shell. Diagram (a) is further enhanced as both the photon as well as the internal quark line can also be on mass-shell simultaneously. In contrast, in diagrams (d) and (e) the W is off shell since its propagator is combined with two real quark lines, so the contributions of these graphs to the cross section is smaller. The remaining diagrams shown in Fig. 2.9 contain a second W propagator and are therefore suppressed. The total cross section for single W production at HERA, including NLO QCD corrections, is 1.0 pb at the centre of mass energy of $\sqrt{s} = 300$ GeV and 1.3 pb at $\sqrt{s} = 318$ GeV. The theoretical uncertainty on these cross sections is 15% and arises from the uncertainties on the parton density functions and the scale used in the calculations [27].

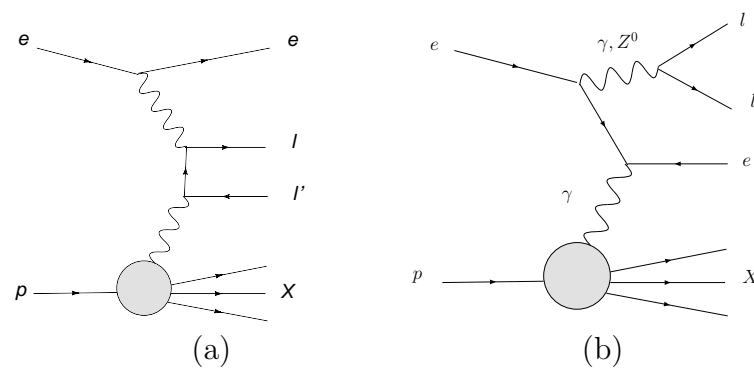


Figure 2.8: Feynman diagrams of lepton pair production: (a) Bethe-Heitler process, (b) Compton-like process.

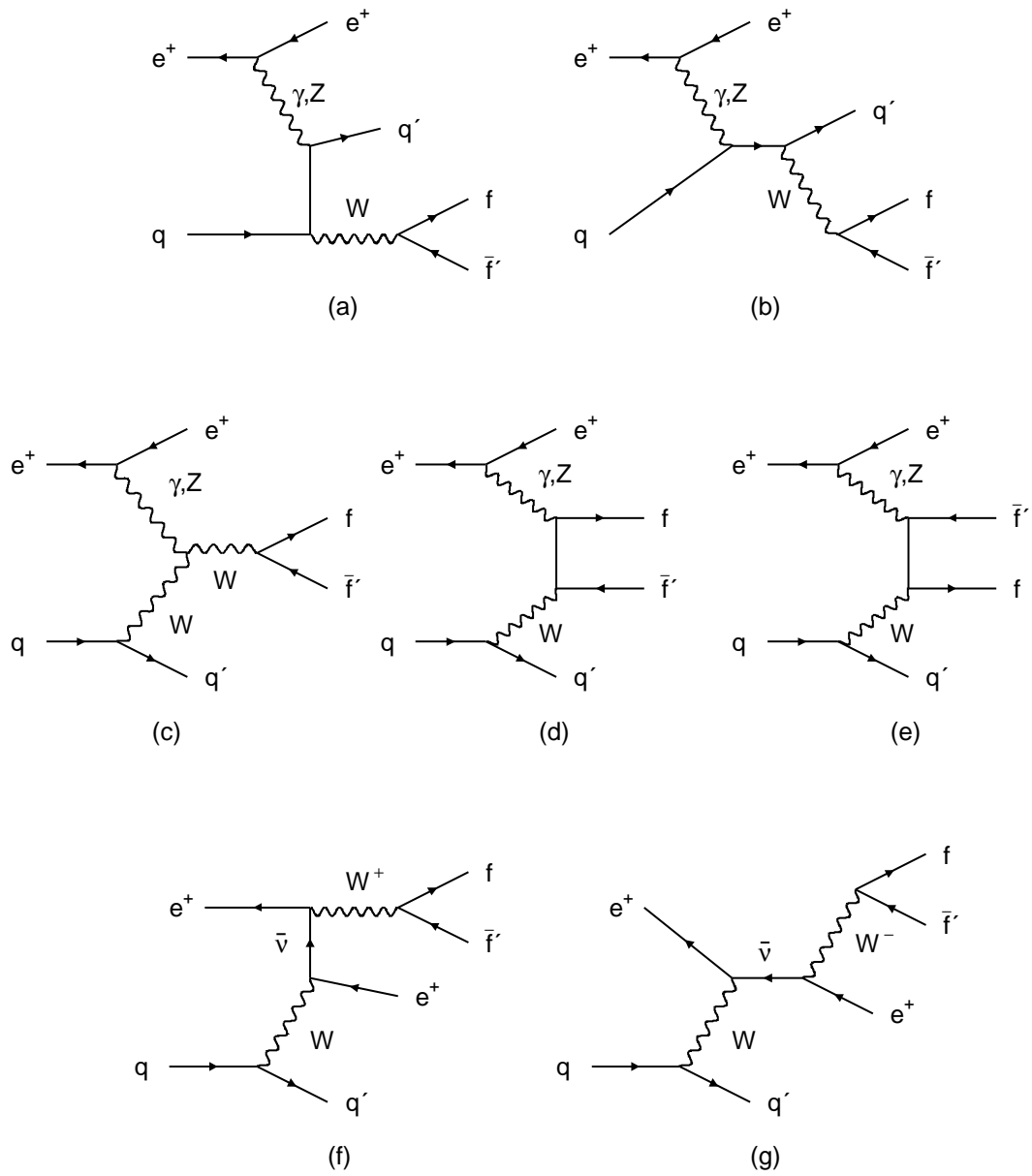


Figure 2.9: Main Feynman diagrams for single W production: (a) and (b) are the dominant diagrams, (c) involves a triple gauge coupling, (d) and (e) contain off-shell W bosons, (f) and (g) contain a second W propagator and are therefore suppressed.

Chapter 3

The ZEUS experiment at HERA

Probing length scales smaller than the size of a proton and producing real electroweak bosons requires very high energies, which can only be achieved with the help of accelerators that boost beams of particles to very near the speed of light and that can focus such beams sufficiently to create collisions between them. Furthermore, detectors are required, on one hand, to have enough bulk material to contain the collision remnants and, on the other hand, measure their properties well enough to draw precise conclusions about the underlying nature of the interactions.

Using the technology currently available, these requirements can only be satisfied with accelerators that are several kilometres long and detectors that usually weigh several thousand tons. The dimensions of such experiments, therefore, pose an enormous engineering, scientific and also financial challenge that cannot be met by a single team of researchers or even a single country. Instead high energy particle physics experiments are the fruit of an international collaboration between several countries involving several hundred scientists, as well as engineers and technicians. As such they form the largest scientific instruments in the world and one of mankind's most advanced achievements.

The following sections describe the HERA accelerator and the ZEUS detector that were used for this analysis.

3.1 HERA collider

The data used in this thesis were generated by the large accelerator called the "Hadron Electron Ring Anlage" (HERA) [28] that was situated at the Deutsches Elektronen SYNchrotron (DESY) laboratory in Hamburg, Germany. HERA was commissioned in 1991 [29] and during its operational period, which spanned a decade and a half, it formed the only high-energy lepton-hadron collider in the world to date. It collided electrons¹ or positrons of 27.56 GeV with protons of 820 GeV (1992–1997) and 920 GeV (1998–2007), thus providing a centre-of-mass energy, $\sqrt{s} \approx \sqrt{4E_p E_e}$, of 301 and 318 GeV, respectively.

¹In this thesis "electron" refers to both electrons and positrons unless specified.

The choice of asymmetric beam energies took account of the energy loss through synchrotron radiation. That loss is proportional to m^{-4} [30], where m is the mass of the accelerated particle, and means that it requires twelve orders of magnitude more energy to accelerate electrons than protons. So, employing more energetic protons allowed HERA to operate with the same energy consumption at an overall higher centre of mass energy. However, it also required the magnets used for bending the proton beam to provide a higher field strength. This was 4.65 T for protons, in contrast to only 0.165 T for electrons, and could only be achieved with superconducting magnets that had to be cooled using liquid helium.

HERA consisted of a ring tunnel with a 6.45 km circumference located about 25 m underground, see Fig. 3.1. Inside the tunnel, counter-circulating electron and proton beams were accelerated in two separate machines, which were brought together at two collision points in the centre of the H1 [31] and ZEUS [32] detectors in the north and south experimental hall, respectively. Two further experiments were situated on the HERA ring: HERMES [33] in the east hall was a fixed target experiment that used the polarised lepton beam from HERA on a polarised H, ^2D or ^3He gas target to study the spin-dependent structure function of the nucleon. HERA-B [34] occupied the west hall and was conceived to study CP violation in B-meson decays by passing the HERA proton beam halo through wires inside the beam-pipe.

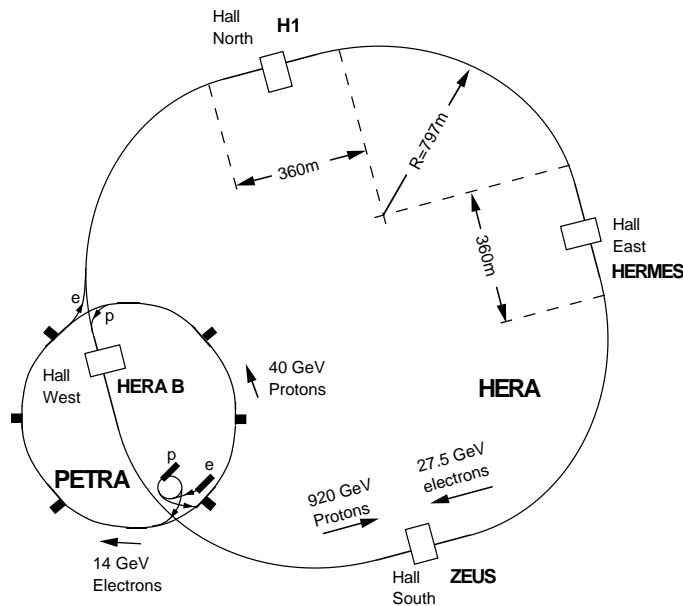


Figure 3.1: The HERA ring collider with the four experiments H1, HERMES, HERA-B and ZEUS and the pre-accelerator PETRA.

To minimise the background from synchrotron radiation inside the detectors, the 6.45 km HERA ring consisted of four straight sections of length 360 m connected by arcs with a 797 m radius as shown in Fig. 3.1. Protons and electrons were injected into the HERA storage ring from a set of pre-accelerators described below. Once the typical beam current of $I_e \approx 35\text{ mA}$ ($I_p \approx 100\text{ mA}$) for electrons (protons) was accumulated, the injection stopped and the beams could then circulate for hours with design lifetimes of 10 – 15 h for electrons and 200 h for protons. Once the beam currents dropped below 10 – 15 mA - or in case of problems - the beams were dumped.

The acceleration of the particles was achieved with radio-frequency (RF) cavities that created an electromagnetic field in which the beam particles experienced a longitudinal accelerating force along the HERA ring. The frequency of oscillation of the field was then tuned to the particles' circulation frequency around the HERA ring such that they were driven to ever higher speeds by the electromagnetic field until they reached the nominal energy for the given accelerator. The HERA magnets were used to bend the particles into a circular orbit around the ring and to focus the particles into bunches. The experiments on the HERA ring received the timing of the bunch crossings from HERA, termed the HERA clock, which allowed them to synchronise the detector trigger and readout systems to bunch crossings.

3.1.1 Bunch structure

The electrons and protons were accelerated separately in bunches that were formed by pockets in the electromagnetic field created by the accelerating RF cavities and the HERA magnets. HERA was commissioned to hold about 170 bunches in each beam, but as the familiarity with the machine grew, that was increased to 210 bunches. Out of these, 174 were colliding bunches, which were paired between the electron and the proton beams. The remaining number were unfilled bunches reserved for the estimation of the beam backgrounds. They consisted of 15 electron *pilot* bunches, which were unpaired, i.e. the corresponding proton bunch was empty and therefore did not produce a collision, 6 proton pilot bunches and 15 entirely empty bunch pairs. Empty bunches also acted as a safety feature in case an emergency beam dump was required.

At HERA, the bunch separation was such that electron and proton bunches were brought into collision inside the H1 and ZEUS detectors at 96 ns intervals. The longitudinal size of the bunches was 0.83 cm for electrons and 8.5 cm for protons. The horizontal dimension of both beams measured around 190 μm in HERA I and 110 μm in HERA II (see Section 3.1.3 for a definition of the run periods), whereas the vertical dimension was much smaller at 50 μm in HERA I and 30 μm in HERA II [35]. The separation between bunches was 4.8 (2.0) ns and 144 (60) cm for the proton (electron) beam [36].

3.1.2 The pre-accelerator system

Several accelerators on the DESY site were used to pre-accelerate protons and electrons and inject them into the main HERA ring.

The proton system's initial stage was formed by a LINear ACcelerator (LINAC) that boosted H^- ions from a magnetron [37] to an energy of 50 MeV and passed them into the DESY III proton synchrotron, where they were stripped of their electrons by passing through a thin foil. The resulting protons were accelerated in 11 bunches with the same 96 ns time separation as the HERA ring until they reached 7.5 GeV. At that point they were injected into PETRA (Positron Elektron Tandem Ring Anlage), which could store up to 70 bunches and accelerated them to an energy of 40 GeV. Upon reaching that, the protons were injected into HERA.

The lepton system could run with both electrons and positrons. The former were obtained directly from an electron gun, whereas positrons were produced from photon conversions by interacting electrons in a tungsten target, where the Bremsstrahlung photons pair produced. The e^+e^- pairs were then separated with a magnetic field.

In the first stage, LINACs I and II increased the lepton energy in stages to 220 and 450 MeV, respectively, before passing them into the DESY II synchrotron to be accelerated to 7.5 GeV. The leptons were then stored in bunches separated by 96 ns in PETRA II until they reach 14 GeV and could be injected into HERA's lepton ring, where they finally achieved their nominal energy of 27.5 GeV.

3.1.3 Run periods and upgrade

Regular beam operation with data-taking started in 1992 and continued until the year 2000, alternating over the years between electron and positron beams. A phase of operation with one type of lepton beam is called a run period. The periods between 1992 and 2000 are referred to as HERA I.

In the year 2000, HERA underwent a major upgrade, in which the luminosity performance was increased by about a factor four by reducing the cross sectional area of the beam (see Section 3.1.1) with an improved beam focus around the interaction point and by increasing the beam currents. The resultant increase in the performance of the machine can be seen in Fig. 3.2, which shows the integrated luminosity delivered by HERA for the different run periods. The steeper slope of the curve for the HERA II (post-upgrade) phase is clearly visible above the HERA I graph. The HERA II phase lasted until March 2007, at which point HERA reduced its proton beam energy to allow the measurement of the longitudinal structure function F_L . For this purpose, HERA delivered 15.7 pb^{-1} at $E_p = 460 \text{ GeV}$ (low energy run, LER) between March and May 2007 and another 9.4 pb^{-1} at a proton beam energy of 575 GeV (medium energy run, MER) in June of the same year. Despite its importance for obtaining F_L , the data taken at lower centre-of-mass energies are not relevant for the topics discussed in this thesis and shall therefore be ignored henceforth.

In addition to the increase in luminosity, HERA was also equipped during the upgrade with spin rotators around the experiments H1 and ZEUS (described below). These produced a longitudinally polarised lepton beam that allowed the measurement of the chirality-dependence of the NC and CC cross sections, see Sections 2.3.1–2.3.2. In the analysis presented here the polarisation was taken into account for the normalisation of the CC background, as outlined in Section 4.5.

In the HERA II run period operations continued with electron and positron beams, but in addition, the lepton beam polarisation was also varied between left- and right-handed leptons. Table 3.1 lists the different data taking periods in HERA I and II with the beam types used, the luminosities delivered by HERA and gated by ZEUS and the mean polarisation of the data sets averaged over both longitudinal lepton polarisations during that period². The luminosity gated by ZEUS is significantly below the luminosity delivered by HERA due to

²The polarisation value of the TPOL (see Section 3.1.5) was used if the LPOL (see Section 3.1.6) was offline.

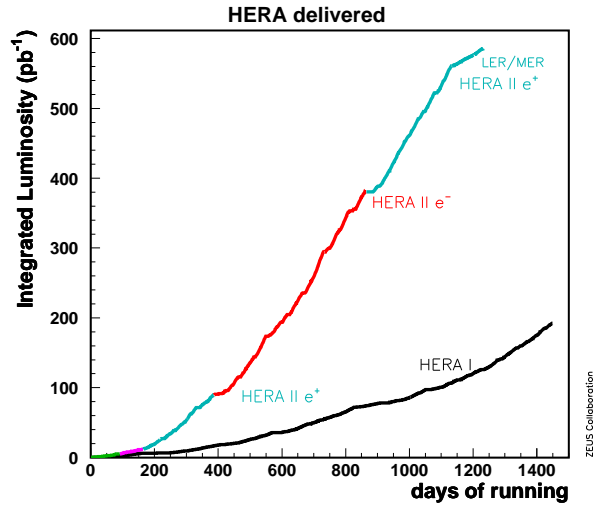


Figure 3.2: The luminosity delivered by HERA over the period 1992–2007. Run periods are split into high energy runs, denoted by HERA I and II, as well as medium (MER) and low energy runs (LER).

Period	Years	Beams	$\mathcal{L}_{\text{HERA}}$ (pb^{-1})	$\mathcal{L}_{\text{ZEUS}}$ (pb^{-1})	P_e (mean)
HERA I	1992 – 1994	e^-p	2.2	0.8	0
	1994 – 1997	e^+p	70.9	48.2	0
	1998 – 1999	e^-p	25.2	16.7	0
	1999 – 2000	e^+p	94.9	65.1	0
HERA II	2003 – 2004	e^+p	89.7	40.8	+0.034
	2005 – 2006	e^-p	290.9	190.9	-0.018
	2006 – 2007	e^+p	180.5	142.4	+0.035
HERA I+II	Total	e^+p	438.2	296.5	+0.035
	Total	e^-p	316.1	208.4	-0.018
	Total	$e^\pm p$	754.3	504.9	+0.013

Table 3.1: Data sets from different years with their beam type, luminosity delivered by HERA and gated by ZEUS and average lepton beam polarisation as measured at the ZEUS detector.

the dead-time caused by temporary detector failures and maintenance requirements which are unavoidable in large and complex detectors like ZEUS.

3.1.4 Beam polarisation

Particles in beams have a random orientation of their spins, in general. However, in storage rings leptons naturally acquire a transverse polarisation through a process called the Sokolov-Ternov effect [38]. In this process lepton-spins in the magnetic field generated by the accelerator magnets are gradually aligned through the emission of synchrotron radiation.

In any magnetic field lepton-spins align themselves along the field lines, but can be parallel as well as anti-parallel. When a photon of synchrotron radiation is emitted the spin of the lepton flips to conserve angular momentum. The Sokolov-Ternov effect results from a difference between the transition probability from parallel to anti-parallel alignment and the reverse. That leads to the gradual build-up of transverse polarisation.

At HERA the characteristic rise-time for the beam to acquire sufficient transverse polarisation was about 37 min [39]. After the HERA upgrade, a pair of spin rotators consisting of dipole magnets enabled HERA to flip the polarisation from transverse to longitudinal before the leptons passed through the H1 and ZEUS detectors. The spins were rotated back to transverse downstream from the experiments to preserve the polarisation as the leptons travelled around the ring.

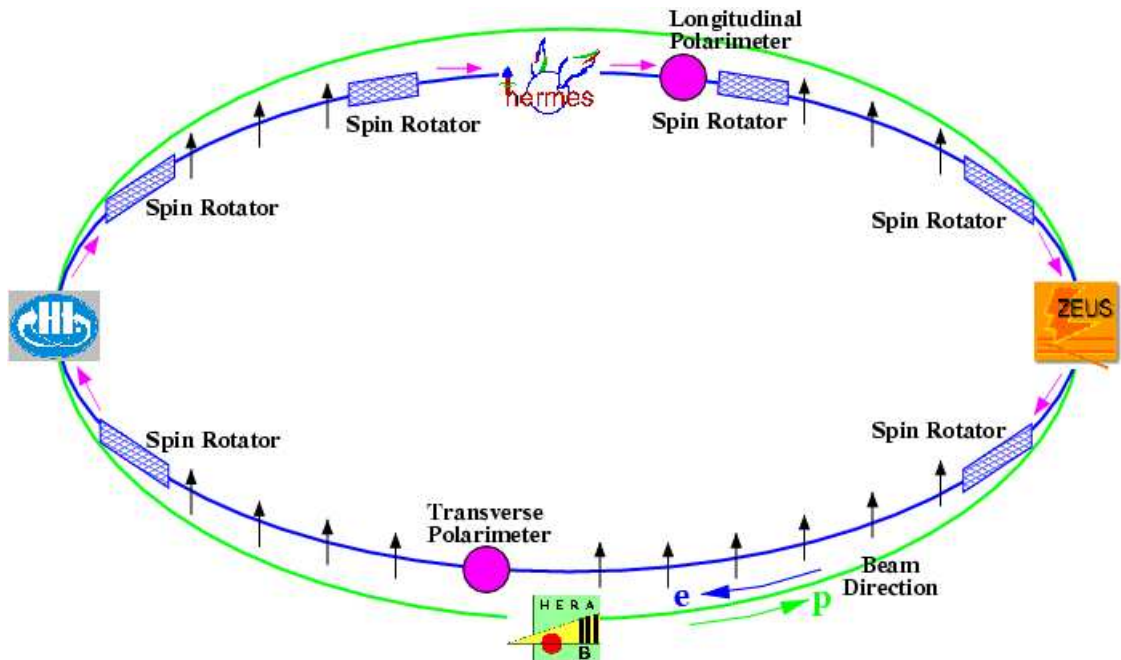


Figure 3.3: The position of the longitudinal and transverse polarimeter and the spin rotators around the experiments on the HERA ring. The direction of the lepton spin is indicated with black (transverse) and pink (longitudinal polarisation) arrows.

The theoretical limit on the polarisation is 92.4%. However, there are several depolarising effects in a real accelerator, due to which the polarisation is in practice much lower.

These can be beam-beam interactions, misaligned magnets or field errors within magnets, as well as stochastic kicks the electron energy receives from emitting a photon of synchrotron radiation [40]. At HERA the typical polarisation was about $\pm 30\%$ although peak values could range between 40 – 50% [41].

A transverse (TPOL) and a longitudinal polarimeter (LPOL) were used to measure the respective polarisation of the beam. The position of the TPOL, LPOL and the spin rotators on the HERA ring is shown in Fig. 3.3.

The lepton beam polarisation was determined by Compton scattering circularly polarised laser beams off the leptons [42] and measuring the energy, E_γ , and the azimuthal angle, ϕ , of the scattered photons, as shown in Fig. 3.4.

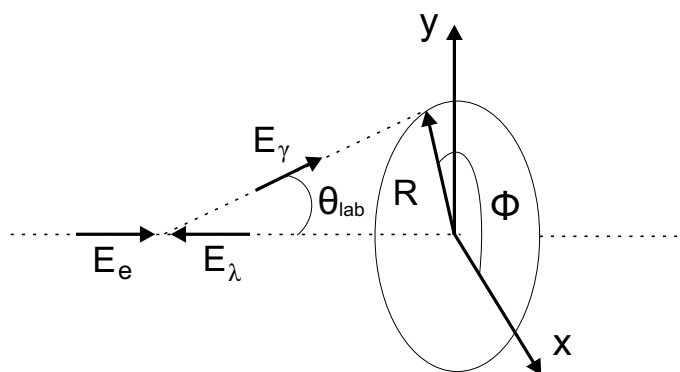


Figure 3.4: Compton scattering of an incident photon with energy E_λ off an electron with energy E_e . The scattered photon travels with energy E_γ in the direction specified by θ_{lab} and ϕ .

This method exploits the fact that the spin dependent cross section for Compton scattering is of the form [43]:

$$\frac{d^2\sigma}{dEd\phi} = \Sigma_0 + S_1\Sigma_1 \cos 2\phi + S_3[P_Y\Sigma_{2Y} \sin \phi + P_Z\Sigma_{2Z}], \quad (3.1)$$

where the transverse and longitudinal components of the lepton polarisation are represented by P_Y and P_Z . The linear and circular components of the laser beam polarisation are S_1 and S_3 , respectively, and the Σ s are known functions dependent on the energy of the scattered photon.

By varying the helicity of the circularly polarised laser light, the lepton polarisation can be determined by measuring the scattered photon energy as well as the angle ϕ and comparing the measured cross sections:

$$\frac{d^2\sigma}{dEd\phi}(S_3 > 0) - \frac{d^2\sigma}{dEd\phi}(S_3 < 0) = 2|S_3|[P_Y\Sigma_{2Y} \sin \phi + P_Z\Sigma_{2Z}] \quad (3.2)$$

At HERA, the experimental setup was such that the transverse position y was measured instead of the angle ϕ . The simple relationship $\phi = \sin^{-1}(y/R(E_\gamma))$ can be used to relate

the two variables since the polar angle, θ_{lab} , and thus also the scattering radius, R , depend only on the energy, E_γ , of the scattered photon.

From Fig. 3.3 it can be seen that at the position of the LPOL the beam was longitudinally polarised. So, with $P_Y \approx 0$ that polarimeter determined P_Z by measuring E and the scattering cross section. Similarly, at the TPOL $P_Z \approx 0$ and hence, P_Y could be obtained from measuring E and y .

The following sections describe the experimental setup of the TPOL and the LPOL.

3.1.5 Transverse polarimeter

The core element of the transverse polarimeter (TPOL) [44] was a 10 W continuous wave laser with a wavelength of 514 nm. The circular polarisation of the laser light was obtained by passing the laser beams through a Pockels cell [45] that also switched between positive and negative helicity with a frequency of 90 Hz. The polarisation measurement [46] was conducted in 1 min cycles, during which a light chopper was used to block the laser beam for the first 20 sec to measure the energy spectrum of the background. After that the chopper opened and passed the laser light into a system of mirrors and lenses, which guided it into the tunnel, where the photons interacted with the leptons. The scattered cross section was measured for both states of circular photon polarisation and the energy distribution measured with the laser off (i.e. chopper closed) was subtracted to eliminate the background, which was mostly formed by Bremsstrahlung.

The scattered photons were measured 65 m downstream from the Compton interaction using the curvature of the HERA ring to separate the scattered photons from the electron beam. The x and y positions of the scattered photons were measured with a silicon strip detector sandwiched between a lead plate and a calorimeter. The lead plate had a thickness of one radiation length and converted the Compton photons into e^+e^- pairs. The calorimeter was used to measure the energy of the shower. It consisted of twelve alternating layers of tungsten and scintillator and was separated into two halves, up and down. The energy was measured by reading out the upper and lower sections of the TPOL calorimeter with separate photomultiplier tubes (PMT).

The uncertainty on the polarisation measurement from the TPOL was 4.2% for the 2004–2006 e^+p data set [47] and very similar to that value for all other HERA II run phases, i.e. less than 5% [22, 48].

3.1.6 Longitudinal polarimeter

The longitudinal polarimeter (LPOL) [49] was very similar to the TPOL, described above. It operated with a 532 nm pulsed laser that acquired a circular polarisation by passing through a Pockels cell and an optical system of mirrors and lenses guided the laser light into the tunnel, where it Compton scattered off the lepton beam. The major difference between the LPOL and the TPOL lay in the detector that measured the scattered photons.

At the LPOL, the transverse component of the polarisation was $P_Y \approx 0$, so the ϕ dependence in Equation. 3.2 vanished and P_Z could be determined by measuring only the energy of the scattered photons. Therefore, the LPOL detector, in contrast to the TPOL, consisted purely of calorimetric devices. These were made up of lead plates in front of four $\text{NaBi}(\text{WO}_4)_2$ crystals that formed the calorimeter, wherein the crystals were each read out individually by a PMT. The energy of the scattered photons was measured by first converting them into electromagnetic showers in the lead plates. Subsequently, the Cherenkov light produced by the charged particles in the $\text{NaBi}(\text{WO}_4)_2$ crystals was read out with the PMTs.

With this setup, the energy asymmetry, A , could be measured through:

$$A = \frac{E_+ - E_-}{E_+ + E_-}, \quad (3.3)$$

where E_{\pm} represents the energy measured by the LPOL for positive or negative helicity of the laser beam. Then the asymmetry was used to deduce the longitudinal component of the lepton beam polarisation through the relation [49]:

$$A = |S_3|P_Z\Pi_{\text{LPOL}} \quad (3.4)$$

It required knowledge of S_3 , the average circular polarisation of the laser, and of Π_{LPOL} , which is the analysing power of the LPOL. The former was known to be greater than 0.999 and the latter was estimated with a Monte Carlo simulation.

The uncertainty on the polarisation measurement from the LPOL was 3.6% for the 2004–2006 e^+p data set [47] and very similar to that value for all other HERA II run phases, i.e. less than 5% [22, 50]. The LPOL was given preference over the TPOL for providing the polarisation measurement, as it had a smaller uncertainty than the TPOL. However, for runs during which the LPOL was offline, the TPOL was used instead.

3.2 ZEUS detector

ZEUS was a multi-purpose detector built and operated by the eponymous international collaboration between 18 countries, comprising over 400 physicists from more than 50 different institutes. It was a joint endeavour between these scientists and a similar number of technicians.

The ZEUS detector consisted of many specialised sub-components, as can be seen in Fig. 3.5. The two centre-pieces, which were vital for data taking, were the central tracking detector (CTD) and the calorimeter (CAL). A microvertex detector (MVD), a presampler, a backing calorimeter (BAC), muon chambers (FMUON, BMUO, RMUO), as well as forward and rear tracking devices (FDET, RTD) then helped to exploit the detector's full capabilities, but could optionally be excluded from the data taking if they worked erratically or failed.

The following sections describe the main components of the ZEUS detector that have been used for this analysis. A more detailed description can be found elsewhere [32].

Positions in the ZEUS detector were measured relative to an orthogonal right-handed coordinate system with z along the proton direction, y vertically upward and x pointing

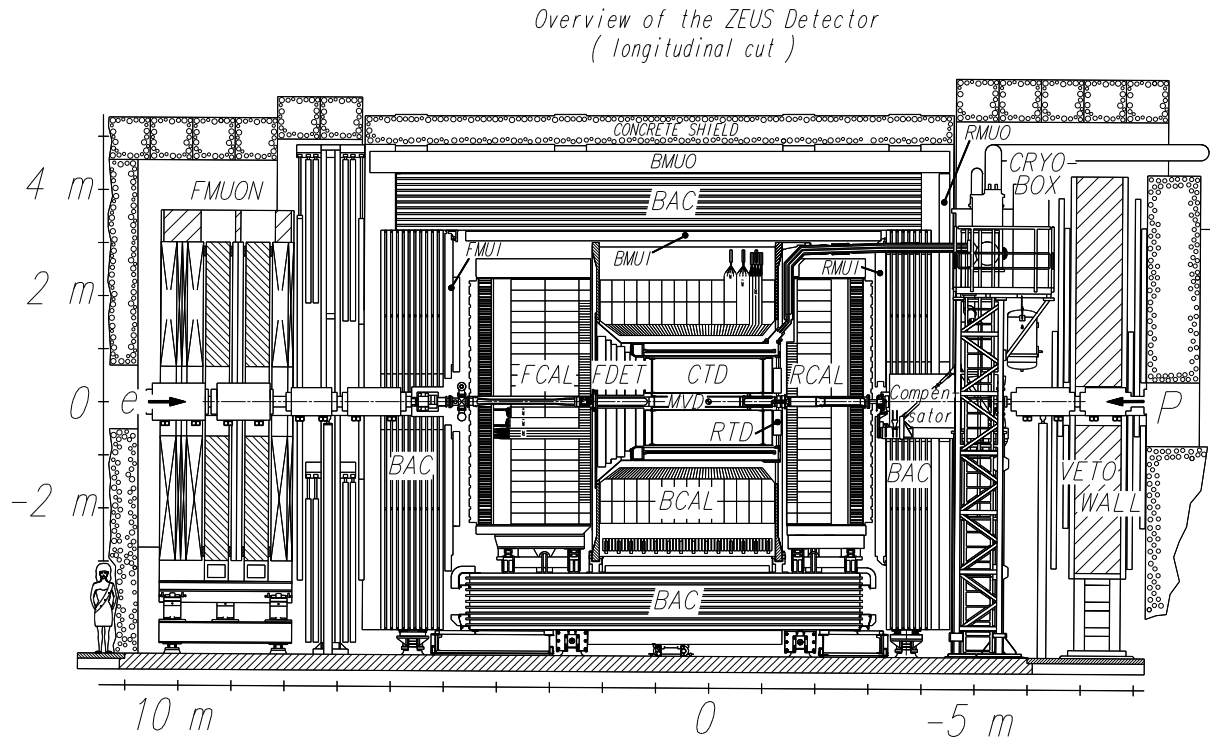


Figure 3.5: A cross sectional view of the ZEUS detector highlighting its subcomponents. The human on the left is drawn to indicate the scale.

towards the centre of the HERA ring (and out of the plane on Fig. 3.5). The origin was the nominal interaction point at the centre of the detector and the transverse plane was defined by the x and y axes. An alternative coordinate system, based on cylindrical coordinates, allowed to describe the motion of high-energy particles in a Lorentz invariant manner using the z axis combined with the azimuthal angle, ϕ , about z and the pseudo-rapidity, η (defined in Equation 5.20), which was derived from the polar angle, θ , relative to the z axis.

The ZEUS detector was asymmetrical along the z direction. That design had been chosen in accordance with the asymmetry in the colliding beam energies. The protons, which were over an order of magnitude more energetic than the electrons, boosted the proton remnant after the interaction along the positive z axis, where the detector thus required the largest amount of bulk material to contain the decay products. This was the region of most activity and is referred to as the front of the detector. Similarly, the section of the detector along negative z is called the rear region.

3.2.1 Calorimeter

The ZEUS uranium-scintillator calorimeter (CAL), which was used to measure the energy of particles, was considered one of the best calorimeters in the world due to its *compensating* response to hadronic activity. Generally, electromagnetic showers deposit more energy than hadronic cascades, which is problematic as jets have an unknown electromagnetic admixture. To circumvent that, the ZEUS calorimeter employed alternating layers of 3.3 mm depleted uranium and 2.6 mm plastic scintillator plates, which had the advantage that the uranium

had a large cross section for absorbing neutrons with subsequent emission of photons. These photons increased the electromagnetic content of the jet and thus, compensated for the lower energy deposited by hadronic showers. Through this mechanism the ZEUS calorimeter achieved an equal response to electromagnetic and hadronic showers of the same energy within 0.5%. Furthermore, the natural radioactivity of the depleted uranium, which was an alloy of ^{238}U (98.2%), Nb(1.7%) and ^{235}U (0.2%), could be used to check and calibrate the calorimeter response.

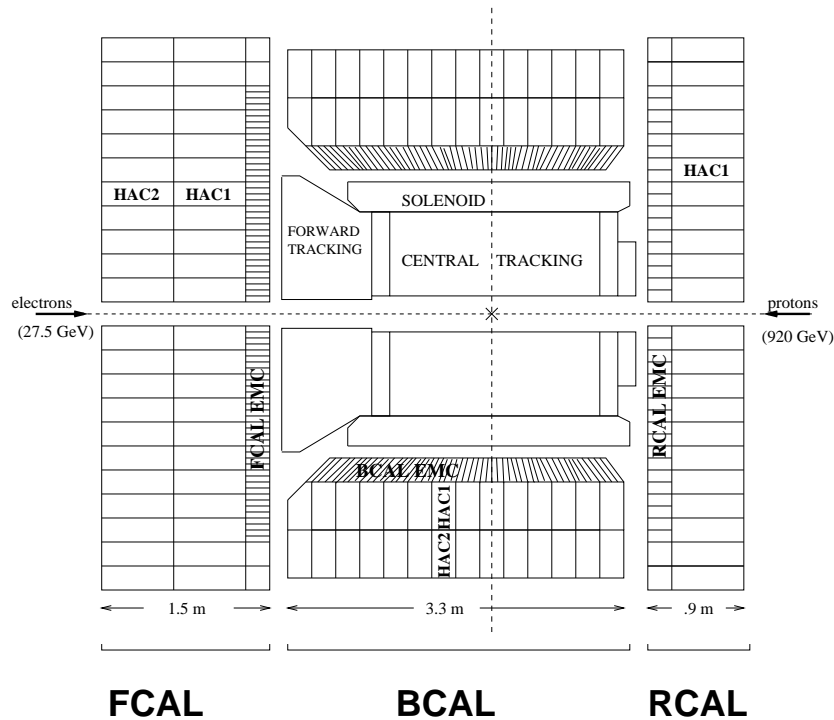


Figure 3.6: The sub-divisions of the ZEUS calorimeter.

The CAL was divided longitudinally into three sections, as shown in Fig. 3.6: the forward (FCAL) [51] at $z > 220$ cm, the barrel (BCAL) [52] in the region of $205 < z < -125$ cm and the rear (RCAL) [51] at $z < -148.5$ cm. It had hermetic coverage around the beampipe, amounting to 99.7% of the solid angle. Radially, the CAL was further divided into one absorption length, λ , of electromagnetic cells (EMC) and an outer layer of hadronic cells (HAC). The FCAL and BCAL experienced most of the activity and were, therefore, equipped with two layers of HAC cells, amounting to 6λ (FCAL) and 4λ (BCAL), in contrast to only a single layer of 3λ in the RCAL.

Cells were arranged into towers with a cross sectional area of 20×20 cm², the area of a HAC cell. The FCAL and BCAL towers had four 5×20 cm² EMC cells per HAC cell, whereas the RCAL contained only two with 10×20 cm². A group of towers then formed a module. The FCAL and RCAL consisted of 24 modules along x with width 20 cm and varying heights in y , such that the face of the FCAL and RCAL in the transverse plane approximated a circle. The 32 BCAL modules sat side-by-side in ϕ but were rotated by 2.5° in azimuth relative to the radial direction to avoid particles escaping undetected by travelling down the length of the module gap.

Each cell was read out by a pair of photomultiplier tubes (PMT) either side. Light

from a scintillator passed via a wavelength shifter into a PMT, where it was converted into electrical signals. The redundancy in the number of PMTs per cell helped to identify CAL ‘sparks’ (see Section 5.3.1) and prevented the loss of cell information if one of the PMTs broke. Furthermore, the spatial resolution of the CAL, which was mainly determined by the granularity of the cells, could be refined by measuring the energy imbalance between the two PMTs.

The energy resolution of the CAL had been measured with a test beam before installation and was found to be $35\%/\sqrt{E} \oplus 2\%$ for hadronic deposits and $18\%/\sqrt{E} \oplus 1\%$ for electromagnetic showers, where the values apply for E measured in GeV [53]. The CAL resolution improved with increasing energy, thus, the CAL became especially important for measuring very energetic particles whose transverse momentum was too large for the central tracking detector (see below) to determine precisely.

The CAL also provided timing information for every deposit with a resolution better than 1 ns for energies above 4.5 GeV. In conjunction with the timing from the HERA clock, this could be used to reject background, as described in Section 5.5.

3.2.2 Presampler

The presampler [54, 55], added to the ZEUS detector in 1998, was a device that was used to correct the energy measurement for showering in inactive material between the interaction point and the CAL. It consisted of scintillator tiles placed in front of the CAL towers that counted the number of minimum ionising particles (MIPs) produced in these showers. That number is proportional to the energy of the shower and was used to correct the energy on an event-by-event basis.

3.2.3 Central Tracking Detector

The central tracking detector (CTD) [56] was a cylindrical wire drift chamber with an inner (outer) radius of 18.2 cm (79.4 cm) and an active volume of about 5 m³. It was situated around the beam pipe at $-100 < z < 105$ cm with full azimuthal and polar angle coverage of $15^\circ < \theta < 164^\circ$. The CTD measured charged particle tracks by recording their ionisation traces created in the chamber’s gas mixture of 83.4% argon, 13.8% ethane and 2.8% CO₂.

Ionised gas molecules were detected using 24192 gold-plated tungsten wires that were divided into 4608 sense wires and 19584 field shaping wires. The latter provided an electrical field, see Fig. 3.7a, in which the free electrons and ions drifted to the positive sense wires and negative field wires, respectively. Near the sense wires the drifting charge freed further electrons and the subsequent avalanche enhanced the signal by a factor of 10^4 . With such amplification even MIPs that only ionise a few tens of atoms per centimetre could be measured efficiently. The electrical pulse created by a charge deposit on a sense wire was recorded as a ‘hit’, including pulse height and time of arrival, and several such hits were combined to fit a particle track. However, the maximum drift time of the charge to the sense wires was around 500 ns, which was too slow for any track reconstruction to be done at the first trigger level, see Section 3.2.7. Nonetheless, from the time of arrival and the known

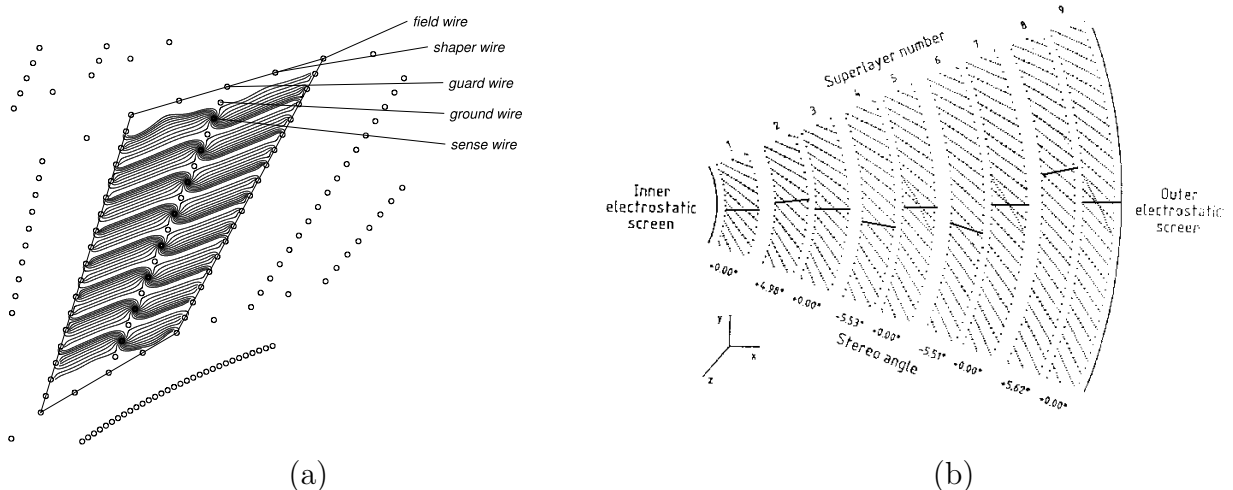


Figure 3.7: (a) Distribution of wires and the resultant field in a CTD cell. (b) The nine super-layers of the CTD with cells inclined by the Lorentz angle.

drift velocity accurate positions were determined for track reconstruction that could be used at the second trigger level.

Groups of eight sense wires were organised into 576 cells that populated 72 radial layers, that in turn were grouped into 9 so called super-layers, shown in Fig. 3.7b. A common requirement for good quality tracks in physics analyses was that they pass the third inner super-layer. That criterion equates to an angular coverage of $18.4^\circ < \theta < 160.7^\circ$. The electric field inside the cells was oriented at a Lorentz angle of 45° to the radial direction so that the drift was at right angles to the radius. That alignment resolved the right-left ambiguity in reconstructing the hits. Sense wires in odd numbered super-layers ran parallel to z (axial layers), whereas, wires in even numbered super-layers were inclined by a stereo angle of $\sim 5^\circ$ (stereo layers) to give equal resolutions in azimuth and polar angles. In addition, layers 1, 3 and 5 were equipped with a dedicated z -by-timing system that provided fast z information with a resolution of $\sigma_z \approx 4$ cm that could be used for triggering [57].

The CTD provided a momentum measurement for every track. This was facilitated by a superconducting solenoid around the CTD that provided a magnetic field of 1.43 T with the \mathbf{B} -field lines in the direction of positive z . The curvature of charged particle tracks in the transverse plane was used to obtain the transverse momentum of the particles by measuring the radius of the fitted track inside the CTD according to $p_t = RQB$, where the transverse momentum p_t of the charged particle is directly related to the radius of curvature, R , the charge of the particle, Q and the magnitude of the \mathbf{B} -field.

The momentum resolution of the CTD depended on the quality of the track, but also on the transverse momentum of the particle since very high energy tracks were effectively straight. For tracks from the vicinity of the nominal interaction point, passing at least three super-layers and carrying a momentum of $P_T > 150$ MeV the uncertainty on the momentum measurement was [58]:

$$\frac{\sigma(p_t)}{p_t} = 0.0058 p_t \oplus 0.0065 \oplus 0.0014/p_t, \quad (3.5)$$



Figure 3.8: The bottom half of the MVD showing the ladders in the barrel, the forward wheels with silicon sensors on the left and the readout cables and services on the right.

where \oplus implies addition in quadrature and the transverse momentum, p_t is measured in GeV. The three terms in the expression take account of the position resolution on the CTD hits, the multiple scattering in the region between the interaction point and the CTD and the scattering inside the CTD itself, respectively. The stated value of the middle term applies to the HERA I phase; the multiple scattering was slightly larger during HERA II due to the presence of the microvertex detector (see below).

The tracks measured by the CTD were used to reconstruct the event vertex. For medium and high multiplicity events this could be achieved with a 2–4 mm resolution along z and < 1 mm in the transverse plane.

3.2.4 The microvertex detector

The microvertex detector (MVD) [59, 60] was installed between the CTD and the beampipe in the ZEUS upgrade in 2000 and had a polar coverage of $7.6^\circ < \theta < 160^\circ$. It provided tracking information close to the beampipe that could be combined with the CTD hits to improve the impact parameter resolution and therefore, the efficiency of finding secondary vertices.

The MVD was assembled from two half-cylinders split in the horizontal plane; the bottom half is shown in Fig. 3.8. The MVD consisted of silicon strip sensors mounted on 30 ladders in the MVD barrel and on 4 wheels in the forward direction. The wheels consisted of 14 silicon sensors each with 480 readout strips at $120 \mu\text{m}$ distance. The barrel ladders of size $6 \times 60 \text{ cm}^2$ were mounted parallel to the beam on a carbon fibre support structure forming three concentric cylinders (see Fig. 3.9) at average radii of 40 mm, 86 mm and 123 mm that carried 4, 10 and 16 ladders, respectively.

Each ladder consisted of 20 sensors of dimensions $6 \times 6 \text{ cm}^2$, which were made of single sided n-type silicon of $300 \mu\text{m}$ thickness with 512 p-type readout strips at $120 \mu\text{m}$ distance separated by 5 p-type strips of $20 \mu\text{m}$ pitch. Capacitive charge division [61] between the strips allowed an intrinsic hit resolution far below the readout distance and measured $20 \mu\text{m}$ for a track at normal incidence. Two adjacent sensors with strips aligned at 90° formed so called $r-\phi$ and $r-z$ sensors that measured the eponymous coordinates of a particle hit within the ZEUS frame of reference. They were connected in pairs via special cables and formed a half module with a single readout, as depicted in Fig. 3.9. Two mirror image half-modules on top of each other were combined to a module, i.e. a double layer with an $r-\phi$ and $r-z$ sensor superposed at each point, and five adjacent modules constituted a ladder.

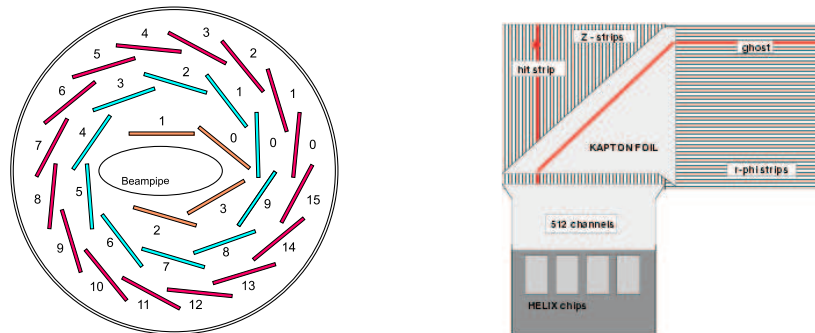


Figure 3.9: Layout of the MVD ladders around the beampipe in the cross sectional view (left) and an MVD half-module showing the r - ϕ and r - z strips (right).

3.2.5 Luminosity monitoring

At HERA the luminosity was determined using the rate of photon production through the Bethe-Heitler interaction $ep \rightarrow e'\gamma p$ [62]. It satisfied the two essential requirements that, on one hand, the cross section of 329 mb was large enough that the statistical uncertainty on the measurement was small and, on the other hand, the theoretical cross section with an uncertainty of less than 1% [63, 64] was known with sufficient precision. The luminosity was determined through $\mathcal{L} = \frac{R}{\sigma A}$, where R is the measured rate of events, σ is the theoretical value of the Bethe-Heitler cross section and A is the acceptance of the luminosity detector. The quantity that was used to normalise cross section measurements was the *integrated luminosity*, i.e. the integral of the instantaneous luminosity over the data taking time.

The quality of the luminosity measurement was essential for obtaining cross sections since a wrong luminosity value leads to an overall systematic normalisation error. At ZEUS, two independent detectors monitored the luminosity: the photon calorimeter (PCAL) and the spectrometer (SPEC). The latter was added during the HERA upgrade because of a concern about the increased synchrotron radiation resulting from the luminosity upgrade. Details on how the PCAL and SPEC values were used in the analysis can be found in Section 6.4.1.

Photon calorimeter

The PCAL [65, 66] was a lead-scintillator sampling calorimeter positioned downstream from the ZEUS detector at $z = -107$ m, see Fig. 3.10. It measured the Bethe-Heitler photons produced in the lepton-proton beam interaction with an acceptance of ≤ 0.5 mrad with respect to the lepton beam direction.

A systematic check of the PCAL's performance could be done based on the fact that electrons involved in the Bethe-Heitler process lost part of their energy to the photon and thus, traveled on a strongly curved path. A detector made of lead-scintillator located downstream from the interaction point at $z = -35$ m could then tag such electrons.

During data taking, the PCAL was directly exposed to synchrotron radiation. This background was reduced by a carbon-lead plate in front of the PCAL with a thickness of four radiation lengths. However, that shield significantly reduced the energy resolution of

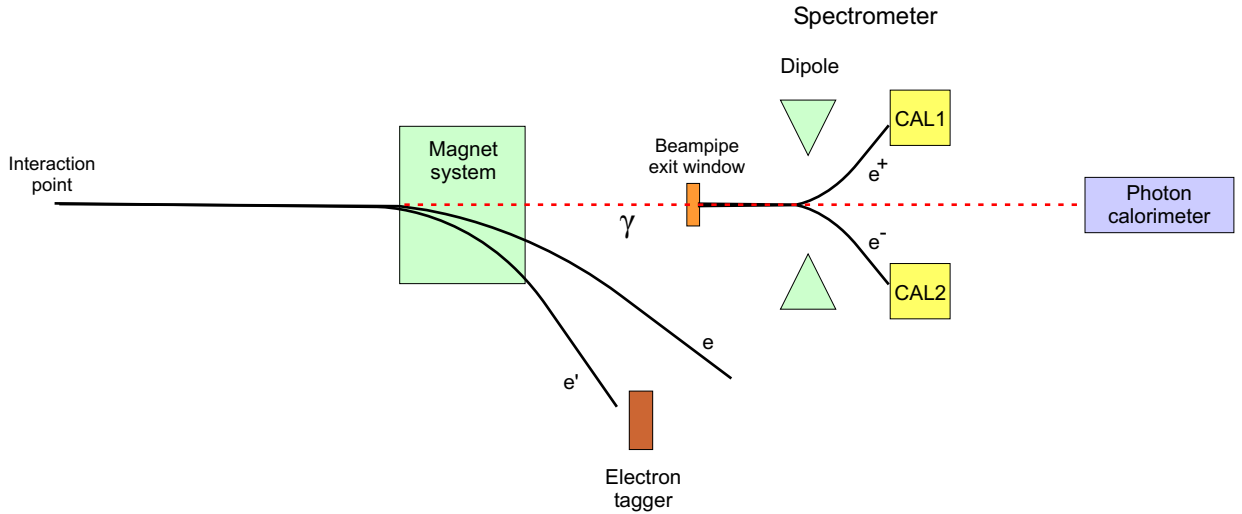


Figure 3.10: Diagram of the luminosity measuring devices: the original photon calorimeter plus ‘electron tagger’ and the spectrometer consisting of the dipole magnet and the two calorimeters, CAL1 and CAL2.

the PCAL from its intrinsic value of $\sigma(E)/E = 18\%/\sqrt{E}$, where E is measured in GeV. To compensate for this deterioration, two Cherenkov detectors made of silica aerogel were mounted around the lead plate during the ZEUS upgrade in 2000 [67]. Their purpose was to measure the electromagnetic shower induced by the Bethe-Heitler photons before and after the shielding and correct the PCAL energy, accordingly.

With a refractive index of 1.03, the silica aerogel was largely inactive to synchrotron radiation whose typical energies of 1–2 MeV rarely produced a Compton electron that was above the Cherenkov threshold of 1.62 MeV. In contrast, Bethe-Heitler photons created e^+e^- pairs with average energies around 20 MeV, which emitted ample Cherenkov radiation. The energy of the Bethe-Heitler photons was determined by summing over the energies measured in the Cherenkov detectors and the PCAL using individual weights obtained from Monte Carlo simulations. The overall uncertainty on the energy was $\sigma(E)/E = 37\%/\sqrt{E}$, where E is measured in GeV [68].

The Bethe-Heitler photon rate in the PCAL was combined with the detector’s acceptance as estimated in a Monte Carlo simulation. The main background was formed by Bremsstrahlung from interactions of the electron beam with residual gas in the beampipe, which could be estimated from pilot bunches. The systematic uncertainty on the PCAL luminosity measurement was around 2.5%.

Spectrometer

The spectrometer (SPEC) [69, 70], installed in the ZEUS upgrade, provided an independent measurement with an uncorrelated systematic uncertainty to that of the PCAL. The SPEC calorimeter was made of tungsten-scintillator, a different material from the PCAL, and used an alternative technique to measure the Bethe-Heitler photons. The SPEC was located

at $z = -92$ m, see Fig. 3.10, where the beam-electrons were sufficiently separated by the bending magnets from the photons. It employed a 3 mm thick window in the beampipe with radius 5 cm, made of 90% copper and 10% beryllium, to convert about one tenths of the photons passing through into e^+e^- pairs. These leptons were subsequently separated out of the photon beam by a dipole magnet and the electrons and positrons were diverted vertically in opposite directions. Two tungsten-scintillator calorimeters at $z = -100$ m [71] detected the leptons individually and measured their coincidence rate.

The advantage of the SPEC over the PCAL was that only a small fraction of the photon beam was converted and detected by the calorimeters, which reduced the rate of multiple-events (pile-up) by two orders of magnitude. Furthermore, the SPEC was insensitive to synchrotron radiation because the field of the dipole magnet diverted all low-energy electrons from synchrotron photon conversions into regions outside of the narrow calorimeter acceptance.

The systematic uncertainty associated with the SPEC value of the luminosity was 3.5% [72].

3.2.6 Background veto system

Two detectors outside of ZEUS were dedicated to rejecting non- ep events. The Veto wall [32], located at $z = -7.50$ m, consisted of an iron wall with scintillator panels either side. It detected particles from the proton beam-halo and protected the ZEUS detector by absorbing them inside the iron bulk. The scintillator information was used by ZEUS to reject beam-halo events that deposited energy in the Veto wall but also leaked into the main ZEUS detector.

The C5 scintillation counter [32] at $z = -3.15$ m provided information on the proton and electron bunch timing. This information was utilised to reject events that could not be associated with a bunch crossing and were therefore not due to an interaction between the electron and proton beams.

3.2.7 Trigger

The electron-proton bunch crossing inside the ZEUS detector occurred at 96 ns intervals, equivalent to an ep interaction rate of 10^7 Hz. That event rate would have resulted in a data volume far above what could be stored and the vast majority of these events did not stem from interesting physics interactions but were formed by beam-gas collisions, halo muons and cosmic contamination (see Section 5.5). Therefore, ZEUS relied on a three-level trigger [73] to clean the data sample and reduce it to 5 Hz before it was written to tape. It was crucial that the trigger system rejected the vastly dominant background, but nonetheless recognised physics events efficiently whilst making fast decisions to keep the dead-time minimal. This was achieved by using a three-level trigger, where very rough selection criteria were applied at the first level and increasingly more detailed and therefore more time consuming requirements were computed by the higher levels, but only for the more interesting events that passed the pre-selection of the first level. The following sections outline the general scheme of each trigger level.

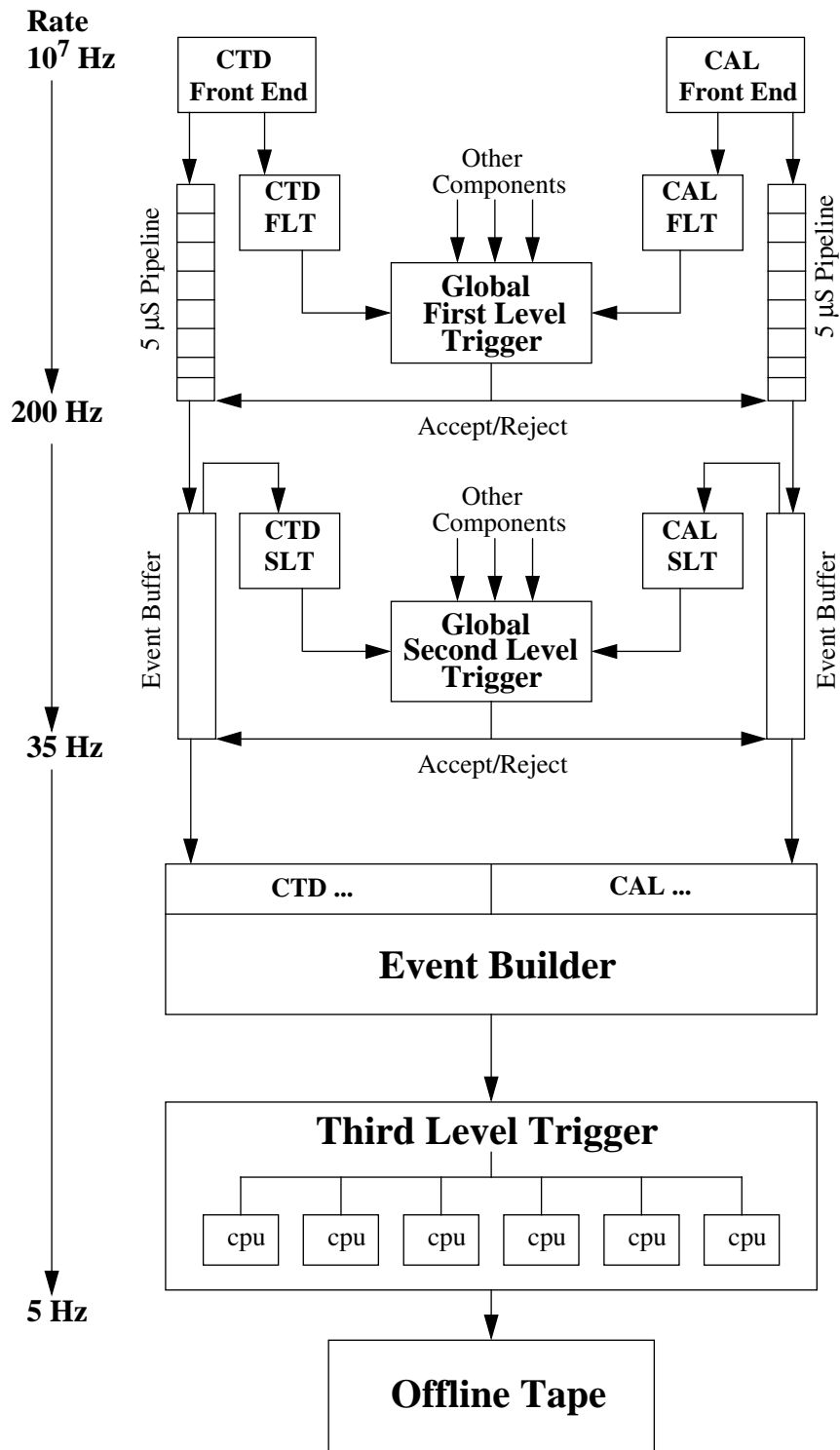


Figure 3.11: The ZEUS three-level trigger system [74] and the in- and output rates at every level. Only the two main components of the ZEUS detector, CTD and CAL, are shown in detail, but other components that feed into the global trigger levels are similar. The CTD SLT was replaced by the Global Tracking Trigger (GTT) in 2006 [75].

First level trigger

The first level trigger (FLT) [76, 77] required the fastest possible decision process and was therefore based entirely on hardware logic running in step with the beam crossing interval. It utilised digital and analogue pipelines to store data for $5 \mu\text{s}$, during which time the decision was made to keep or to reject the event. These pipelines allowed the detector to operate at zero dead-time.

The FLT removed mainly beam-gas events (see Section 5.5), which were recognised, for example, by the high total number of tracks in the event and the low fraction of tracks that originated from the event vertex. An important input to the decision hence came from the CTD FLT [77] that identified events compatible with charged particles emerging from a region around the nominal interaction point. This was done by measuring the hit distribution in the r - ϕ plane with the z -by-timing system and comparing it to template patterns of hits. The advantage of this method was that the processing rate was independent of the track multiplicity and the processing time was minimised by the fact that the z -by-timing was only implemented for CTD super-layers 1, 3 and 5. The tracking information was then passed to the global first level trigger (GFLT), at which point it was checked against 64 slots that encoded basic event requirements from a range of detectors with fast signals. Based on these the event was either rejected or passed to the next trigger level.

The other key input to the GFLT came from the CAL FLT (CFLT) [76] that collected the total energy from CAL towers above a threshold of 500 MeV and calculated global event variables, e.g. missing transverse momentum or the presence of isolated leptons based on the distribution of deposits in the EMC and HAC towers. To save processing time, the event vertex was assumed to be at the origin of the ZEUS coordinate system. Before passing to the GFLT, the CAL information was further pruned by the Fast Clear [78] that used CFLT information to reject events based on the clustering of energy in the CAL.

The total time taken by the GFLT to obtain a decision is $4.4 \mu\text{s}$, after which the event rate that is passed to the second level is 200–1000 Hz.

Second level trigger

The second level trigger (SLT) [79] consisted of component-based parallel processing computers that ran asynchronously with the bunch crossing interval. The SLT could utilise more time than the FLT to make a decision, nonetheless, detailed event properties were still stored and handled locally by all components and then passed to the global second level trigger (GSLT) comprising 60 slots. At this stage, the calorimeter could employ the full information at cell level and the CTD had sufficient time to execute a simple pattern recognition and reconstruct track momenta as well as the primary vertex. However, in contrast to the FLT, the processing rate of the CTD SLT was sensitive to the hit multiplicity. In total, the GSLT required 7 ms to make a decision and the output rate passed to the third level, containing almost purely physics events, was 50–100 Hz.

Third level trigger

After the SLT the entire event information was recorded in a database format by the so called Event Builder. That format was then used by the third level trigger (TLT) to perform the last stage of the background rejection. A fast version of the full event reconstruction software was run on a computer farm and could select events based on the output of jet reconstruction algorithms, electron finders and full tracking information. The final rate with which events were written to tape was about 5 Hz. The most activity was in the slots dedicated to charge current events as these relied on missing transverse moment, a common feature of background events.

3.2.8 Offline event reconstruction

The events stored on tape were processed offline to reconstruct event details that were too time-consuming to obtain at the trigger level. The ZEUS PHYSics Reconstruction (ZEPHYR) package obtained in three stages the detector information required to reconstruct the full event kinematics and implemented the complete calibration constants for the detector.

In the first stage, information from the tracking detectors, the calorimeter and the luminosity detectors was obtained. The second stage reconstructed particle tracks using the package VCTRAK [80, 81] by identifying track segments, which were then matched to form tracks. In the same stage, energy deposits in the calorimeter were combined to clusters and subsequently matched to the reconstructed tracks [82]. The final stage ran particle identification algorithms.

To obtain the event information for an analysis the standard ZEUS analysis package, EAZE, had to be run. It returned the event information in the format of ntuples. Over the lifetime of ZEUS, a lot of specialised algorithms had been developed to e.g. implement correction routines, identify particles and reconstruct event kinematics. Eventually, these were standardised and combined in an additional software package, called ORANGE (Overlying Routine for Analysis Ntuple GEneration) [83], which was run in conjunction with EAZE, and used the best standard methods for reconstructing the event details.

Chapter 4

Monte Carlo simulation

Particle physics detectors are far too complex to predict their response based on analytical calculations. Therefore, statistical methods have to be used to predict particle signatures and detector effects, e.g. showering in the inactive material. The underlying electron-proton interactions have to be modelled in the same manner since they involve many partons, higher order interactions and non-perturbative processes that cannot be calculated exactly. Consequentially, particle physics measurements rely on accurate simulations of the detector response and the known Standard Model processes; reflecting their statistical nature these are called Monte Carlo (MC) simulations.

In ZEUS, MCs were utilised for many different purposes, e.g. calibrating various detector components. However, a full discussion of their use lies outside the scope of this thesis and the following description is limited to the MCs that were used explicitly in this analysis.

4.1 Simulation procedure

The complex task of simulating a high energy experiment was split between several specialised programs. Event generators were used to produce samples of specific physics processes. They took into account the hard process and sub-programs, incorporated into the generators, dealt with hadronisation, which is the confinement of partons into bound and colourless final states. The individual treatment of these two aspects of the electron-proton interaction is based on QCD factorisation theorems [23], according to which the calculable hard interaction that occurs fast and on very short length-scales can be separated (factorised) from the non-perturbative hadronisation that is slower and acts over larger distances.

The generator output consisted of lists of four-momenta for the initial and daughter particles produced in the simulated ep interaction. With the aid of the AMADEUS interface, that output was converted into a file format that could be used as input to the programs in charge of simulating the detector response (MOZART) and the trigger chain (CZAR, ZGANA, TLT-ZGANA). The aim was to process the MC samples with a similar data recording chain to the one used for real ep data, see Fig. 4.1 for a comparison. MOZART was based on the GEANT 3.13 package [84], which allowed the detailed detector geometry to be implemented (e.g. how electronic channels recorded a particle deposit) and modelled the passage of particles through

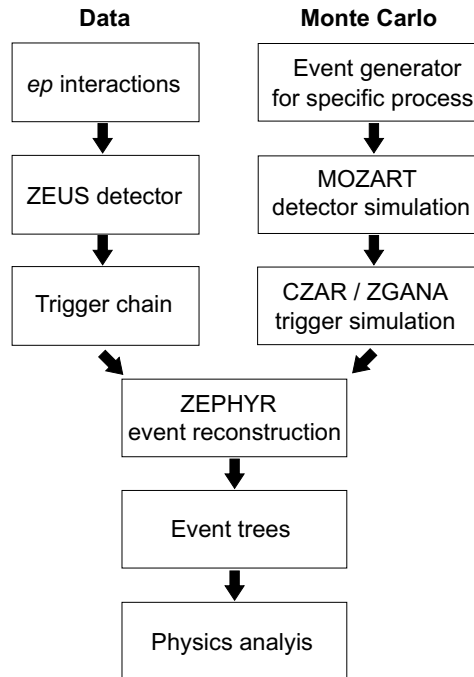


Figure 4.1: The Monte Carlo event simulation and the data taking chains.

the detector. Based on the virtual detector response the trigger simulation then applied the same algorithms as used for data to reach a trigger decision.

After this stage, both MC and ep data were processed by the same reconstruction program, called ZEPHYR (see Section 3.2.8), which collected the information from all the detector sub-components to reconstruct physics observables. The final output had the form of event trees (ntuples) that held all information pertaining to an event (CAL deposits, track variables etc.) in branches and linked it to the run and event number. These data and MC ntuple were used as the basis of every physics analysis. To keep statistical uncertainties on the MC negligible, the generated samples contained up to an order of magnitude more events than could be produced from the real physics processes at ZEUS.

The large size of the MC samples and the need for detector and trigger simulation made the reconstruction of MC events computationally a much more intensive task than the reconstruction of data. In the past, the MC reconstruction had to be distributed by a facility called FUNNEL over several hundred computers across the globe. However, for the upcoming start of larger experiments at the LHC a new computational network, termed the Grid, was developed to cope with the anticipated demand on CPU time. With the opening of this new facility, ZEUS began to migrate the MC reconstruction from FUNNEL to the Grid [85]. This was particularly beneficial for the post-upgrade HERA II data sets since these put additional demands on computation time. The reason for that was the increase in data luminosity and the insertion of the MVD, which led to an increase in detector simulation and reconstruction times. The measurement of single W production presented in this thesis was the first published ZEUS physics analysis to use MC that was simulated and reconstructed entirely on the Grid, thus, highlighting the viability of the new Grid facility.

For this analysis, several MC samples were combined to simulate the main physics process

to be measured, as well as all relevant background processes that could contaminate the event selection. In order to get the correct admixture of each process comparable to real data the samples were individually renormalised with a weight factor, w , given by:

$$w = \mathcal{L}_{\text{data}}/\mathcal{L}_{\text{MC}}, \quad \mathcal{L}_{\text{MC}} = N_{\text{gen}}/\sigma_{\text{theory}} \quad (4.1)$$

where \mathcal{L} denotes luminosity (for data and MC as indicated), N_{gen} is the number of generated events and σ_{theory} is the theoretical value of the cross section for that specific process. Specific samples were used for each run-period, reflecting the centre-of-mass energy, lepton beam type and trigger setup. The generators employed for this thesis are described in more detail in the following sections including tables detailing the number of generated events, the theoretical cross section of the process and the effective luminosity of the MC.

4.2 QED radiation

The MC samples for Neutral and Charged Current included electroweak radiative corrections to first order in α_{QED} . Feynman diagrams of such higher order contributions are shown in Fig. 4.2. Diagrams (a) and (b) are classified depending on the mass of the virtual particles as Bremsstrahlung/Bethe-Heitler (small mass of photon and lepton), QED Compton (small photon mass, large lepton mass) or radiative DIS (large photon mass, small lepton mass). The latter also distinguishes between diagrams (a) and (b) as Initial State Radiation (ISR) and Final State Radiation (FSR), respectively. The remaining diagrams (c) and (d) are in fact of order α_{QED}^2 , nonetheless, they contributed at lower order by interference and were therefore included.

Quarks could also radiate photons, however, the contribution of those diagrams could be neglected due to the fractional electromagnetic charge of the quarks that reduced the coupling to the photon compared to the electron, and due to the slightly larger quark mass. The latter can be understood by recalling that the synchrotron radiation loss, as mentioned in Section 3.1, depends on the mass of the accelerated particle as m^{-4} [30]. A similar relation applies to energy loss through Bremsstrahlung with the modification that the mass dependence increases to m^{-6} [86]. The result is that even small increases in the mass of the charged particle result in the strong suppression of photon radiation.

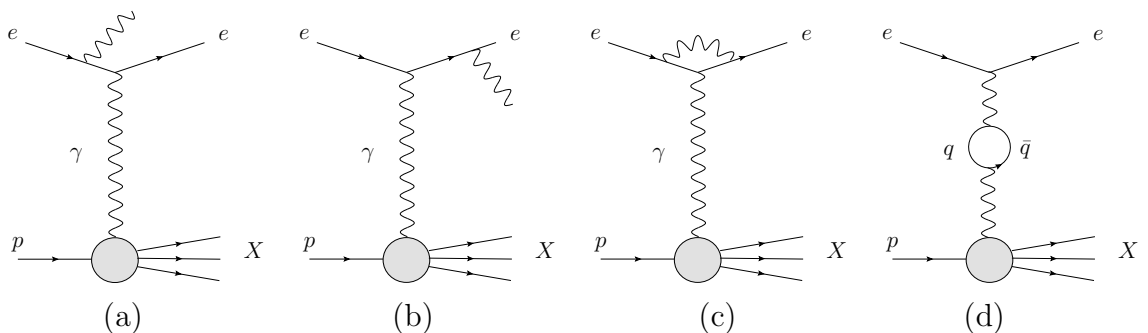


Figure 4.2: Feynman diagrams that contribute to the electroweak corrections: (a) Initial state radiation, (b) final state radiation, (c) vertex correction, (d) propagator correction.

4.3 QCD radiation and hadronisation

The MC simulations were conducted at leading-order (LO). Nonetheless, higher order QCD effects had to be taken into account to model some phenomena observed at ZEUS that occur beyond LO, namely two- and three-jet production shown in Fig. 4.3. Two different schemes based on perturbation theory could be employed for that: In the Colour Dipole Model (CDM) [87], on the one hand, QCD cascades were simulated with radiating colour dipoles formed by pairs of coloured objects that emitted gluons. A QCD shower could be created starting with a colour dipole connecting the struck quark and the proton remnant. After emitting a gluon, two new colour dipoles - connecting the struck quark with the gluon and the gluon with the proton remnant - could in turn emit gluons etc.

The Matrix Element and Parton Shower Model (MEPS), on the other hand, combined first order α_s matrix elements (ME) with parton showers (PS) that relied on the DGLAP [88] leading log approximation (named after Dokshitzer, Gribov, Lipatov, Altarelli and Parisi) to sum all orders in perturbation theory. The Altarelli-Parisi splitting-functions [88] determined the energy distribution between the branches of the QCD cascade and angular-ordering [89] was used for the final state.

In contrast to the underlying hard process and QCD radiation, the formation of the final state particles was a non-perturbative process and therefore could not be calculated from first principles. However, two different phenomenological models of hadronisation could be used: the Lund String Model [87] and Cluster Hadronisation [90]. The former considers strings of self-interacting gluons between colour-connected $q\bar{q}$ pairs. According to this model, the struck quark is connected by a string to its quark partner in the proton remnant. The string stretches as the quarks fly apart, but the energy density in the string is kept constant at around 1 GeV/fm. This results in a linear increase in energy with string length that allows the string to fragment into new $q\bar{q}$ pairs connected in turn by strings. The process is repeated until all the energy of the initial pair is converted into quarks and anti-quarks that are then grouped into hadrons. Decays of the hadrons are permitted until the final state particles are on mass-shell.

The alternative approach of the Cluster Model is based on the grouping ('pre-confinement') of partons into colourless states already at the perturbative stage. These clusters form seeds from which hadrons are generated by combining the clusters with pair-production of $q\bar{q}$ -pairs from gluons in a non-perturbative process. Clusters are constructed up to a few GeV and subsequently decay into known particles.

The parton distribution function (PDF) of the proton have to be incorporated into the MCs to accurately simulate the probability, with which the lepton probe interacted with partons of different flavour and momentum. This is done using the library PDFlib [91]. Newer sets of PDFs are available, however, the sensitivity to differences between these and PDFlib are negligible for the processes relevant to this analysis.

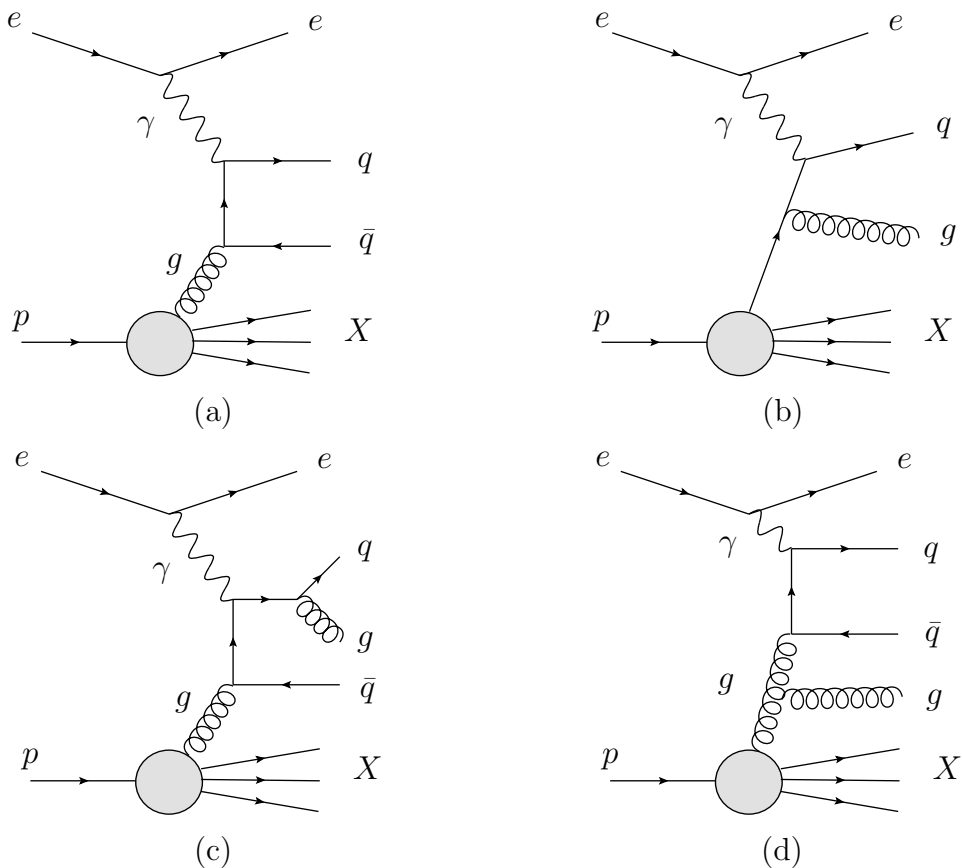


Figure 4.3: Feynman diagrams of higher order QCD processes: (a) 2-jet production via boson-gluon fusion and (b) via gluon radiation, (c) 3-jet production through final and (d) through initial state radiation.

4.4 Single W production

The production of single W bosons at HERA was simulated using the generator EPVEC 1.0 [92]. This leading-order program does not incorporate QCD radiation, but single W bosons can be produced via both the NC and the CC process. Examples of Feynman diagrams that contribute through these mechanisms are shown in Fig. 2.9.

The generator divides the NC production mechanism into two modes by separating the cross section into different regions of phase space according to:

$$\sigma = \sigma(|u| > u_{\text{cut}}) + \int^{u_{\text{cut}}} \frac{d\sigma}{d|u|} d|u|. \quad (4.2)$$

The terms correspond to the modes called *DIS* and *resolved*, respectively, which are distinguished using the four-momentum transfer, $u = (p_q - p_W)^2$, between the incoming quark and the final state W boson. The boundary value between the two modes was chosen to be $u_{\text{cut}} = 25 \text{ GeV}^2$, but the total cross section is sufficiently insensitive to the value of u_{cut} , as shown in Fig 4.4b. Similarly, the dependence of σ on the lepton beam polarisation, see Fig. 4.4a, could also be neglected even though it is itself large, since the mean polarisation in the e^-p and e^+p data sets of the HERA II running phases was less than 4% (see Table 3.1).

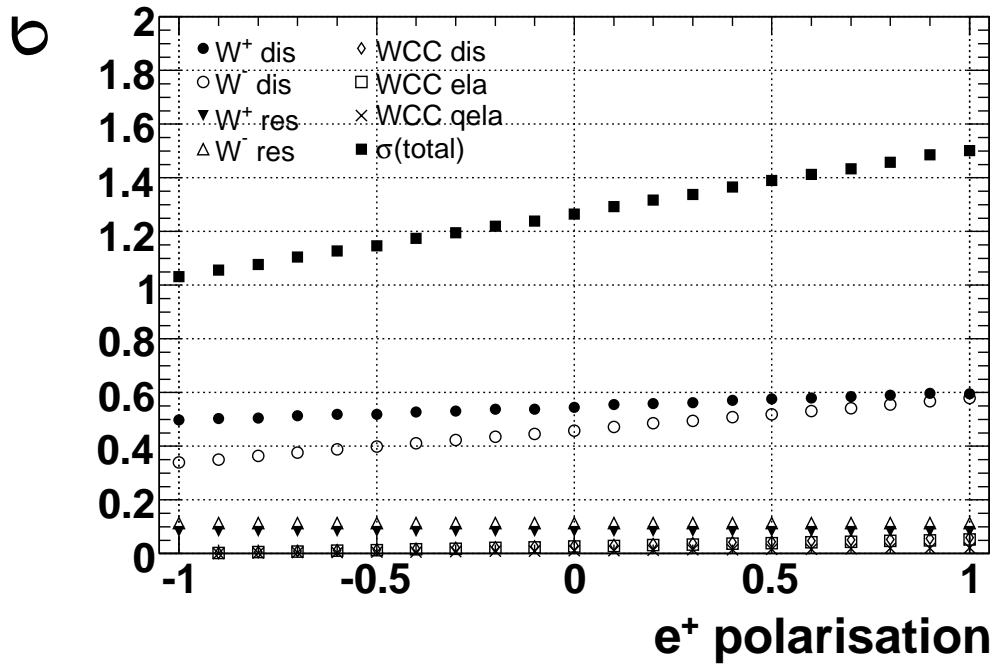
Single W production (EPVEC)				
Beams	Sample	$N_{\text{gen}} \times 10^{-3}$	σ (pb)	\mathcal{L} (fb $^{-1}$)
e^+p	W^+ (DIS)	46 (20)	0.513 (0.391)	89.7 (50.2)
	W^- (DIS)	10 (20)	0.428 (0.324)	23.4 (61.7)
	W^+ (res)	60 (10)	0.082 (0.126)	731.9 (78.6)
	W^- (res)	10 (10)	0.114 (0.100)	87.7 (99.6)
	W (CC DIS)	1	0.037 (0.029)	27.1 (34.1)
	W (CC ela)	1	0.040 (0.033)	25.3 (30.0)
	W (CC qela)	1	0.015 (0.012)	65.9 (80.0)
e^-p	W^+ (DIS)	50	0.458	109.3
	W^- (DIS)	50	0.434	115.3
	W^+ (res)	50	0.082	610.0
	W^- (res)	50	0.114	437.6
	W (CC DIS)	1	0.033	30.1
	W (CC ela)	1	0.039	25.5
	W (CC qela)	1	0.015	65.8

Table 4.1: Details of the samples used to simulate single W production via NC in the DIS and resolved (res) modes, as well as via CC in the DIS, elastic (ela) and quasi-elastic (qela) modes. The columns indicate the beam type, the total number of generated events (N_{gen}), the cross section (σ) used before the NLO reweighting and the effective luminosity (\mathcal{L}). The numbers in brackets apply to the lower proton beam energy of 820 GeV. The value of N_{gen} is in some cases a nominal number that agrees with the actual value within 5%.

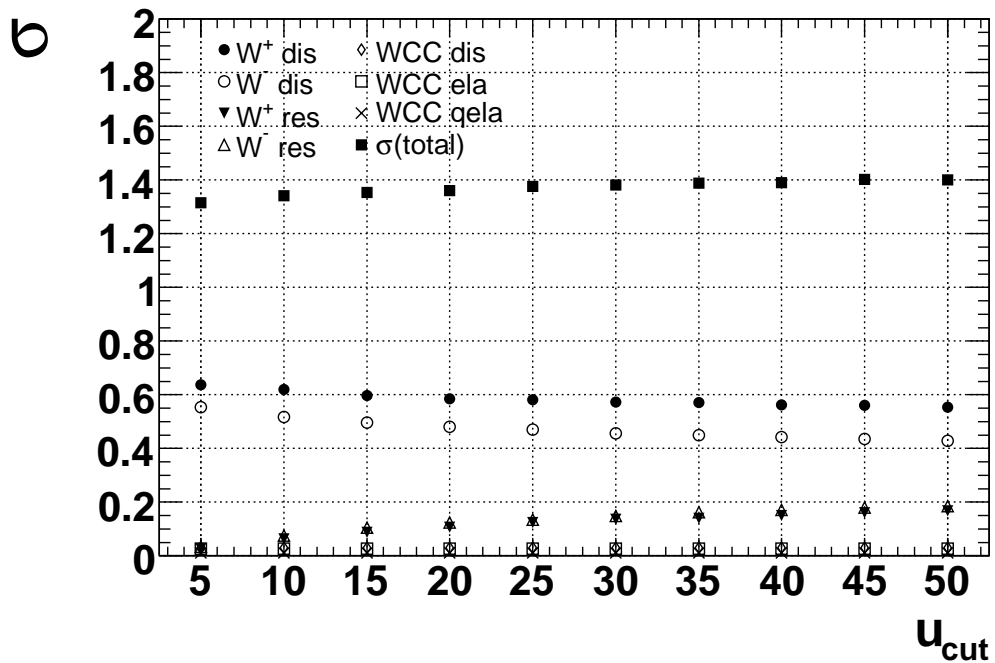
In the DIS mode, the production cross section was determined using helicity amplitudes for the process $q \rightarrow Wq'$, $W \rightarrow l\nu$. The resolved mode covers the region where $u < u_{\text{cut}}$ and EPVEC obtained the cross section by folding the main process $qq' \rightarrow W \rightarrow l\nu$ with the parton densities of the proton and effective parton densities of the resolved photon.

The cross section for CC mediated single W production is about an order of magnitude smaller than that of the corresponding NC mechanism, since a photon exchange contributes to the latter. However, the small admixture of the CC process was taken into account using EPVEC CC samples split into three modes termed *elastic*, *quasi-elastic* and *DIS*. In this case, the phase space was separated using the four-momentum transfer, Q^2 , to the hadronic system and the invariant mass, W_{had} , of the final hadronic state. The elastic mode specified the region where $W_{\text{had}} = m_p$ and the DIS region was defined by $|Q^2| > Q_0^2$, where Q_0 is the minimum momentum transfer at which the quark parton model can be applied [92]. The remaining phase space made up the quasi-elastic mode.

Table 4.1 details the number of events generated, the cross sections used and the effective luminosities for the different samples. The next to leading-order (NLO) parton density functions for the proton that were used by EPVEC were obtained from the set CTEQ4D [93] for the MC samples corresponding to the 96–97 e^+p data set and from CTEQ5D [94] for all other samples. The set GRV-G(LO) [95, 96] provided the photon structure function at LO and hadronisation was simulated according to the Lund String Model using PYTHIA 5.7 and JETSET 7.4 [97, 98]. However, it should be noted that, because of the reweighting to the NLO cross section (see next section), the relevant PDF sets were the ones stated below.



(a)



(b)

Figure 4.4: (a) The dependence of the total cross section for single W boson production and of the cross sections for individual production channels on the lepton beam polarisation at $s = 318$ GeV. (b) The dependence of these cross sections on u_{cut} at the same centre-of-mass energy.

4.4.1 NLO reweighting

The samples of single W bosons were generated by EPVEC using the LO cross section. In order to obtain NLO precision, the MC samples were reweighted in bins of rapidity, y_W , and transverse momentum, P_T^W , of the W boson to the known NLO double differential cross sections, $d^2\sigma_{\text{NLO}}/dP_T^W dy_W$, as listed in the appendix of Reference [99]. Every event generated by EPVEC received a weight, w_{NLO} , given by

$$w_{\text{NLO}} = \left(\frac{d^2\sigma_{\text{NLO}}}{dP_T^W dy_W} \right) / \left(\frac{d^2\sigma_{\text{EPVEC}}}{dP_T^W dy_W} \right), \quad (4.3)$$

where $d^2\sigma_{\text{EPVEC}}/dP_T^W dy_W$ is the value of the double differential cross section used by EPVEC. The specific reweighting factors that were used for the present MC samples, as well as the EPVEC double differential cross sections are shown in Figs. 4.5–4.7 separated into W^+ and W^- production, lepton beam types and centre of mass energies.

The double differential cross sections presented in Reference [99] are based on the ACFGP [100, 101] set of photon PDFs and the CTEQ4M [93] the parton densities of the proton.

4.5 Neutral and Charged Current sample

Neutral Current mediated DIS formed a significant background to single W production due to cases, in which the scattered beam electron was identified as the isolated lepton and a mis-measurement of the proton remnant lead to the reconstruction of fake missing transverse momentum. Most of the NC interactions scattered the beam electron into the rear region of the detector and that feature could be exploited to remove most of these events (see Section 6.1). However, at the highest four-momentum transfer, Q^2 , the scattered electron from a NC event was detected in the forward region, where it could be misidentified as the isolated lepton from a single W boson.

In order to simulate the contribution of these events precisely, the statistical uncertainty on the MC simulation at large Q^2 was reduced by using additional NC samples produced with a higher threshold value of Q^2 . A generator level requirement on the minimum four-momentum transfer, Q_{min}^2 , was necessary for every DIS Monte Carlo because the cross section increases rapidly for small Q^2 (see Equation 2.9) and without a restriction the samples would be entirely dominated by low Q^2 events. The details of the MCs are given in Table 4.2. It lists the number of events generated, the cross section used and the effective luminosity. From the latter it can be seen that the statistical uncertainty on the MC sample is negligible compared to the data.

The weight factor, w , as given in Equation 4.1, had to be modified to give the correct normalisation after combining several NC samples. It was calculated individually for every event based on its true (generator level) value of Q^2 and summed over all MC samples that contributed at that Q^2 , according to:

$$w(Q^2) = \mathcal{L}_{\text{data}} * \left(\sum_i \mathcal{L}_{\text{MC},i}(Q^2 > Q_{\text{min},i}^2) \right)^{-1}, \quad (4.4)$$

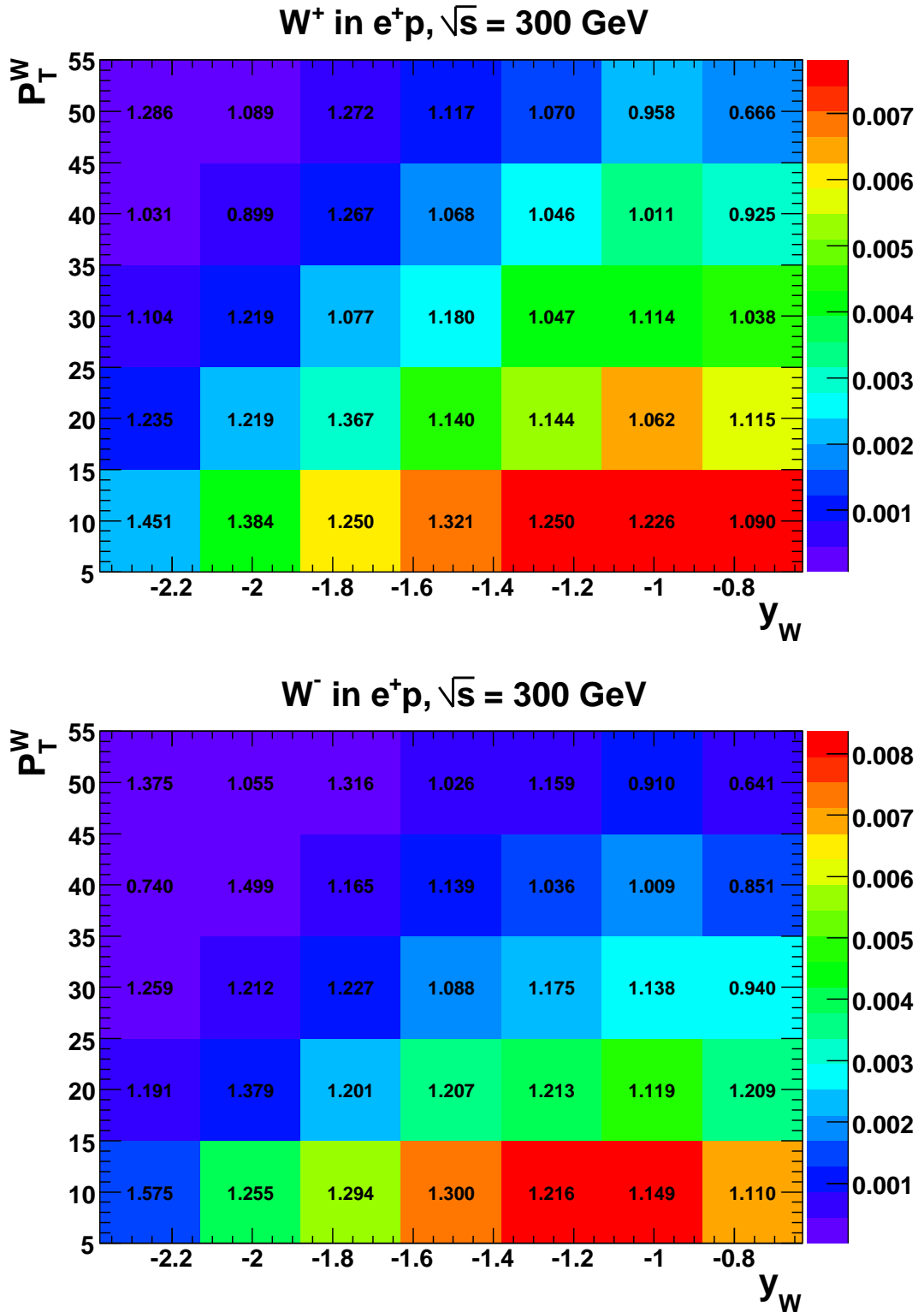


Figure 4.5: The double differential cross section $d^2\sigma_{\text{EPVEC}}/dP_T^W dy_W$ (in units of pb/GeV) used by EPVEC (colours) and the NLO reweighting factors (numbers) for single W^\pm production in e^+p collisions at a centre of mass energy of 300 GeV. The quantities P_T^W and y_W are the transverse momentum and the rapidity of the W boson, respectively. Entries in bins are zero where not specified.

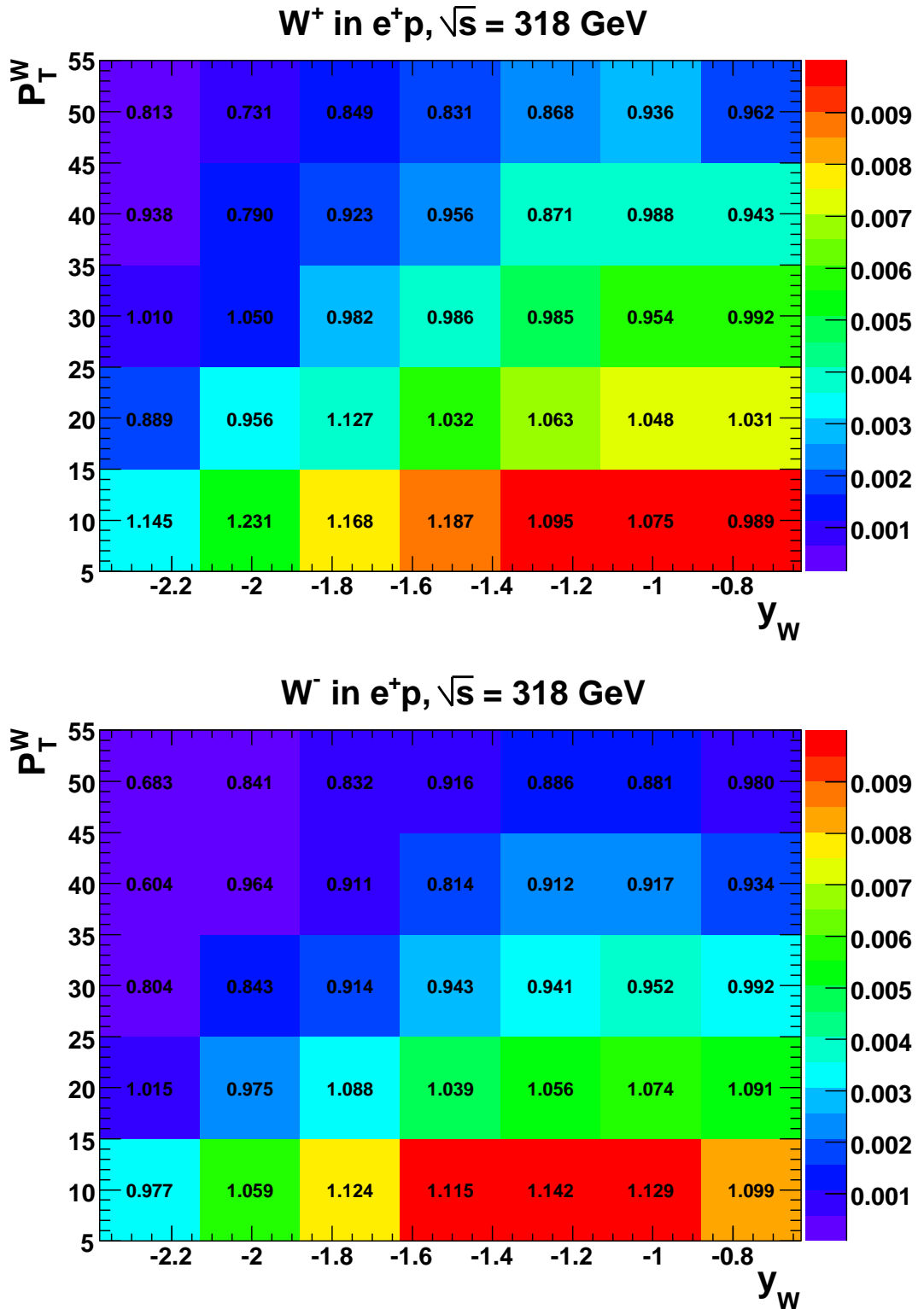


Figure 4.6: The double differential cross section $d^2\sigma_{\text{EPVEC}}/dP_T^W dy_W$ (in units of pb/GeV) used by EPVEC (colours) and the NLO reweighting factors (numbers) for single W^\pm production in e^+p collisions at a centre of mass energy of 318 GeV. All other details as in Fig. 4.5.

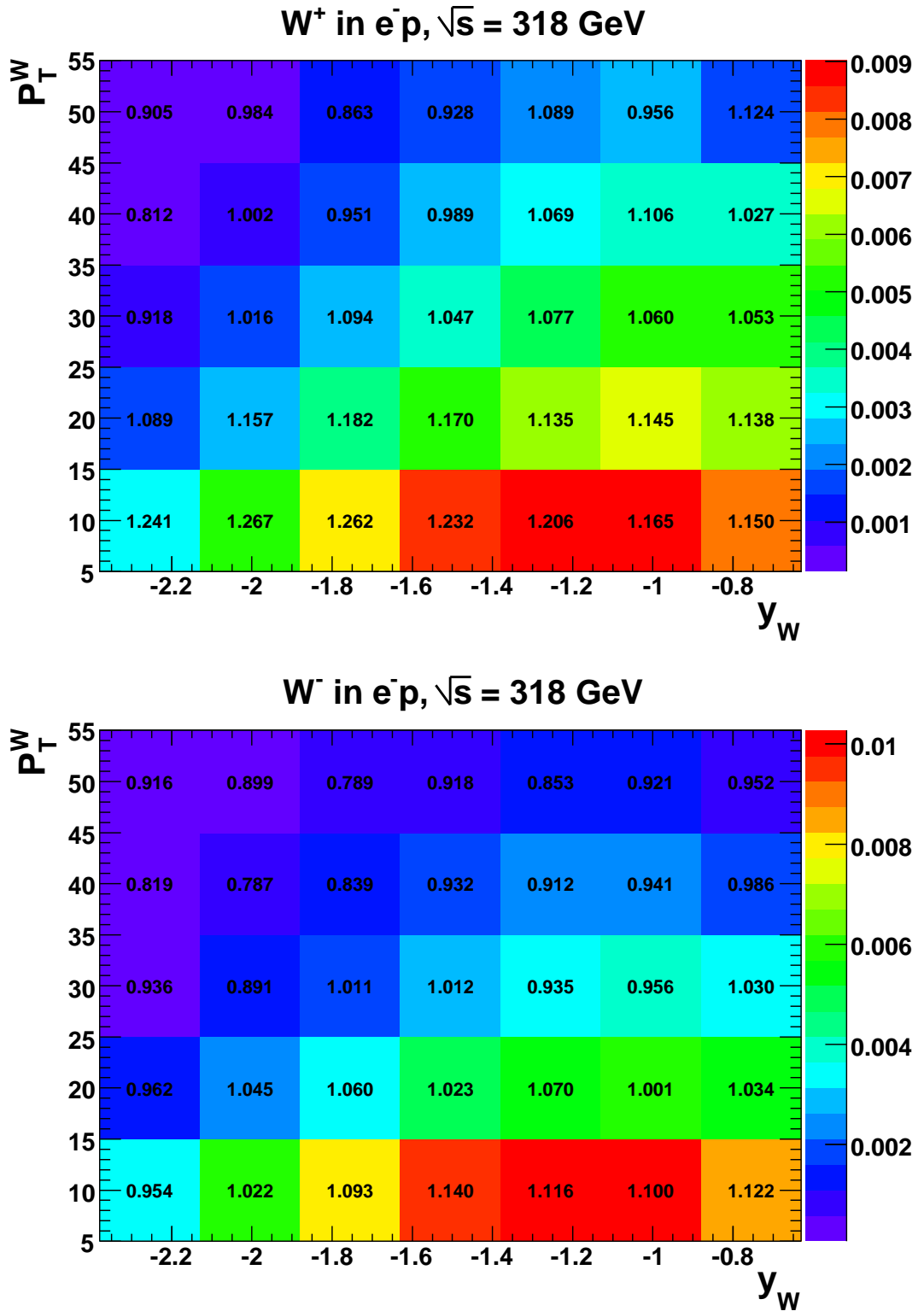


Figure 4.7: The double differential cross section $d^2\sigma_{\text{EPVEC}}/dP_T^W dy_W$ (in units of pb/GeV) used by EPVEC (colours) and the NLO reweighting factors (numbers) for single W^\pm production in e^-p collisions at a centre of mass energy of 318 GeV. All other details as in Fig. 4.5.

Charged and Neutral Current (ARIADNE)						
Beams	Sample	Q^2 (GeV ²)	Years	$N_{\text{gen}} \times 10^{-3}$	σ (pb)	\mathcal{L} (fb ⁻¹)
e^+p	CC	> 10	96–97	50	41.425	1.2
			99–07	250	44.885	5.6
	NC	> 400	96–97	619	1097.1	0.6
			99–00	120	1167.7	0.1
			03–07	1 973		1.7
	NC	> 1250	99–00	50	197.42	0.3
			03–04	993		5.0
	NC	> 2500	99–00	24	58.915	0.4
			03–07	493		8.4
NC	> 5000	99–00	24	14.844	1.6	
		03–07	477		32.2	
e^-p	CC	> 10	98–06	250	79.414	3.1
	NC	> 400	98–99	120	1196.7	0.1
			04–06	2 558		2.1
	NC	> 1250	98–99	50	217.08	0.2
			04–06	1 418		6.5
NC	> 2500	98–99	24	71.866	0.3	
		04–06	600		8.3	
NC	> 5000	98–99	24	21.733	1.1	
		04–06	605		27.8	

Table 4.2: Details of the samples used to simulate CC and NC events. For the 96-97 data the NC Monte Carlo consisted only of the sample with $Q^2 > 400$ GeV². All other details as in Table 4.1.

In contrast, the background from CC events only contributed to single W production if a particle of the hadronic system was misidentified as the isolated lepton. This was independent of the Q^2 of the hard process and, therefore, only a single MC sample of CC events with $Q^2 > 10$ GeV² was used.

Neutral and Charged Current DIS events were both simulated using the event generator DJANGO 1.3 [102]. It interfaces the programs LEPTO [103] and HERACLES [102], which implement leading-order electroweak ep interactions and electroweak radiative corrections, respectively. LEPTO also allows for lepton polarisation, however, samples were generated unpolarised. Instead the Charged Current MC was weighted to the longitudinal lepton polarisation, P_e , of the data (listed in Table 3.1) using the weight factor $1 \pm P_e$, see Equation 2.19:

$$w = \frac{\mathcal{L}_{\text{data}}}{N_{\text{gen}}} \sigma(P_e) = \frac{\mathcal{L}_{\text{data}}}{N_{\text{gen}}} \sigma(P_e = 0) (1 \pm P_e) \quad (4.5)$$

QCD cascades were simulated using the program ARIADNE [104], which employs the colour dipole model (CDM) described in Section 4.3. The systematic uncertainty of this QCD model is estimated in Section 6.4 by simulating parton showers with LEPTO, which provides an alternative description of QCD radiation and boson-gluon fusion based on the MEPS model.

Lepton pair production in e^+p (GRAPE)				
Sample		$N_{\text{gen}} \times 10^{-3}$	σ (pb)	\mathcal{L} (fb $^{-1}$)
e^+e^-	(ela)	30 (30)	13.391 (12.649)	2.2 (2.4)
	(qela 1)	30 (10)	5.750 (5.547)	5.2 (1.8)
	(qela 2)	30 (3)	0.220 (0.195)	136.4 (15.4)
	(DIS 1)	30 (40)	32.635 (31.96)	0.9 (1.3)
	(DIS 2)	30 (12)	8.258 (7.915)	3.6 (1.5)
	(DIS 3)	30 (10)	6.476 (6.185)	4.63 (1.6)
	(DIS 4)	30 (4)	3.660 (3.563)	8.2 (1.3)
$\mu^+\mu^-$	(ela)	30 (30)	10.206 (9.654)	2.9 (3.1)
	(qela 1)	30 (10)	4.969 (4.761)	6.0 (2.1)
	(qela 2)	30 (3)	0.167 (0.146)	179.6 (20.5)
	(DIS 1)	30 (20)	13.002 (12.172)	2.3 (1.6)
	(DIS 2)	30 (5)	2.681 (2.381)	11.2 (2.1)
	(DIS 3)	30 (5)	2.375 (2.161)	12.6 (2.3)
	(DIS 4)	30 (3)	1.216 (1.123)	24.7 (2.7)
$\tau^+\tau^-$	(ela)	30 (10)	6.350 (5.994)	4.7 (1.7)
	(qela 1)	30 (3)	3.563 (3.407)	8.4 (0.9)
	(qela2)	30 (5)	0.144 (0.091)	208.3 (55.1)
	(DIS1)	30 (10)	5.233 (4.678)	5.7 (2.1)
	(DIS2)	30 (3)	1.047 (0.856)	28.7 (3.5)
	(DIS3)	30 (3)	0.954 (0.818)	31.4 (3.7)
	(DIS4)	30 (3)	0.479 (0.412)	62.6 (7.3)

Table 4.3: Details of the samples used to simulate lepton pair production via the DIS, elastic (ela) and quasi-elastic (qela) modes. The numbers in brackets indicate the numbers used for the HERA I data set. All other details as in Table 4.1.

To obtain the hadronic final state, DJANGO called the package JETSET [97] that computes hadronisation within the framework of the Lund String Model. The parton density functions of the proton at NLO were provided by the set CTEQ5D [94].

4.6 Lepton pair production

The event generator GRAPE-Dilepton 1.1 [105] described lepton pair production in ep collisions. It used cross sections calculated at tree level by GRACE [106]. The proton PDFs used in this MC were obtained from CTEQ5L [94] and the hadronisation was done by interfacing GRAPE to PYTHIA.

The simulation of lepton pair production was split into the regimes of elastic, quasi-elastic and DIS scattering using the kinematic variables

$$Q_p^2 = [k - (k' + p_{l+} + p_{l-})]^2 \quad (4.6)$$

$$M_{\text{had}}^2 = [k + p - (k' + p_{l+} + p_{l-})]^2, \quad (4.7)$$

where M_{had} represents the mass of the hadronic system, Q_p^2 is the four-momentum transfer

Lepton pair production in e^-p (GRAPE)				
Sample		$N_{\text{gen}} \times 10^{-3}$	σ (pb)	\mathcal{L} (pb $^{-1}$)
e^+e^-	ela	30	13.391	2.2
	qela 1		5.756	5.2
	qela 2		0.220	13.6
	DIS 1		33.347	0.9
	DIS 2		7.992	3.75
	DIS 3		6.450	4.65
	DIS 4		3.689	8.1
$\mu^+\mu^-$	ela	30	10.205	2.9
	qela 1		4.969	6.0
	qela 2		0.167	179.6
	DIS 1		13.050	2.3
	DIS 2		2.657	11.3
	DIS 3		2.368	12.7
	DIS 4		1.220	24.6
$\tau^+\tau^-$	ela	30	6.350	4.7
	qela 1		3.563	8.4
	qela 2		0.104	288.5
	DIS 1		5.248	5.7
	DIS 2		1.043	28.8
	DIS 3		0.951	31.5
	DIS 4		0.480	62.5

Table 4.4: (continued) Details of the samples used to simulate the DIS, elastic (ela) and quasi-elastic (qela) modes. All other details as in Table 4.1.

at the proton vertex and $k, k', p, p_{l\pm}$ are the four-momenta of the incoming and outgoing electron, the proton and the lepton pair, respectively.

The region was called elastic if $M_{\text{had}} = M_p$, whereas, quasi-elastic and DIS modes were further subdivided into:

- quasi-elastic 1 (qela1) for $1.08 < M_{\text{had}} < 5$ GeV
- quasi-elastic 2 (qela2) for $M_{\text{had}} > 5$ GeV
- DIS 1 for scattering off the u -quark
- DIS 2 for scattering off the \bar{u} -quark
- DIS 3 for scattering off the d or s -quark
- DIS 4 for scattering off the \bar{d} or \bar{s} -quark

The generator level requirement on the sample was that at least one lepton carried transverse momentum $P_T^l > 5$ GeV and had a polar angle of $5^\circ < \theta_l < 175^\circ$. Further details of the MC samples used are given in Tables 4.3–4.4.

4.7 Photoproduction

The package that generated direct and resolved photoproduction events was HERWIG [107] using the NLO proton PDF set CTEQ4D [93] and set GRV-G(LO) [95,96] for the photon. It was fundamentally different in its approach to fragmentation as, unlike the other MC packages described above, it was based on a Cluster Model (see Section 4.3).

The sample was generated with the requirement that either the transverse momentum of the event satisfy $P_T^{\text{had}} > 6$ GeV or that the total hadronic transverse energy fall in the region of $E_T > 30$ GeV. Photoproduction could, in principle, contribute to the selection of isolated leptons if, for example, a mis-measurement caused sufficiently high missing transverse momentum to appear in the event. However, the criterion on large missing transverse momentum above 12 GeV (see Section 6.1) turned out to remove all photoproduction events in the MC. Hence, this type of MC sample was only used to confirm that the selection requirements used in the analysis reject it successfully.

4.8 Monte Carlo corrections

The comparison between the HERA II data and the MC samples showed a discrepancy in the description of the calorimeter energy that was not present between the HERA I data and its corresponding MC sets. This discrepancy was attributed to the increase in dead-material in the detector during the upgrade but was not rectified using the standard corrections applied to the electromagnetic and the hadronic energy (see Sections 5.3.2–5.4). Therefore, a set of additional corrections for the EMC and the HAC energies had to be applied to the MC samples at the analysis stage in order to bring the description of the MC in line with the HERA II data.

In the HERA II MC samples the electron energy had to be adjusted by scaling down in the FCAL and BCAL by 5% and 2%, respectively. Additionally, in the BCAL the electron energy was also ‘smeared’ with a Gaussian spread of 3%. The hadronic energy in the HERA II MC was also scaled down by 1% everywhere except for events in the FCAL, defined such that the unscaled hadronic angle satisfied $\gamma_{\text{had}} < 35^\circ$, for which it was scaled down by 2.5%.

Chapter 5

Data sets, event reconstruction and backgrounds

This chapter lists the data sets that have been used for this thesis. It also outlines how the relevant particles were identified and details the event variables that were reconstructed. The last section describes the various backgrounds not associated with the interaction of the electron and proton beams that affected the measurements and explains how the event variables were used to eliminate or reduce these.

5.1 Data sets

Events containing isolated leptons and large missing transverse momentum were very rare events at HERA. Therefore, all available ZEUS data from the years 1994 – 2007 (see Section 3.1.3), comprising both electron and positron beam data, were used for the analysis. Very early electron data from 1992 – 1993 were ignored as no adequate MC simulations were available and the luminosity contribution of that period was negligible compared to the subsequent years.

The HERA II data set was obtained with polarised lepton beams. The polarisation averaged over a whole data taking period was small, as shown in Table 3.1. However, each of these periods consisted of separate run phases, comprising roughly equal amounts of data, with left-handed (LH) or right-handed (RH) longitudinal polarisation of about 30%.

5.2 Event reconstruction

After recording the data with the ZEUS trigger and readout system, events were selected and studied by dedicated physics analyses that used the information obtained by the various detector components to reconstruct more sophisticated event variables. Several quantities were defined to aid the reconstruction and selection of events. The definitions were guided by the characteristics of the event class for which these variables were used, so the search for

isolated leptons distinguished between electrons and muons. The variables described here were used for both unless stated otherwise. Furthermore, a massless approximation was used in some cases, e.g. in converting momentum from the CTD into an energy measurement. This is a good approximation at DIS energies, for which the analysis was conducted.

5.2.1 Electron identification

Electrons were identified using the electron finder EM [108,109]. It combined electromagnetic clusters in the CAL with tracking information and computed the likelihood that the electron candidate was a true electron. The probability estimate was based on a comparison of several measured quantities of the candidate shower, namely,

- depth of the shower, i.e. fraction of energy deposited in the HAC
- width of the shower in azimuthal angle, ϕ , in the BCAL or x in the FCAL and RCAL
- width of the shower in z in the BCAL or y in the FCAL and RCAL
- energy not attributed to the electron within a radius of 0.8 in η - ϕ around the electron candidate (where η is given by Equation 5.20)
- difference in polar angle, θ , between the matching track and the CAL deposit
- difference in ϕ between the matching track and the CAL deposit
- deviation between track momentum and CAL energy as measured by $1/E_e - 1/P_{\text{trk}}$

to the expectation for true electrons. Each measured variable was thus attributed a corresponding sub-probability, P_i^{EM} , to be the signature of a true electron and EM obtained a grand probability P_e^{EM} from the product of these sub-probabilities:

$$P_e^{\text{EM}} = \prod_i P_i^{\text{EM}} \quad (5.1)$$

The requirement on the electron probability of $P_e^{\text{EM}} > 0.001$ ensured that the candidate was very likely to be an electron. The efficiency of this requirement has been studied previously [110] and found to be 98%. This efficiency is also implemented in the MC.

EM was optimised for NC DIS events to achieve maximum electron-finding efficiency and electron-hadron separation. Using the pulse height information from the photo-multipliers in the CAL it could determine the impact point of electrons on the CAL with a resolution of 1 cm. This was used to reduce fake electrons by constraining the distance of closest approach (DCA) of the track to the electromagnetic cluster of the electron to typically $\text{DCA} < 10$ cm.

EM corrected the electron energy taking into account inactive material, non-uniformity of the CAL and mis-measurement of the energy from known broken PMTs, see Section 5.3.

5.2.2 Muon identification

The identification of muons relied on the muon finder MV [111, 112], which searched for deposits in the CAL that were consistent with a minimum ionising particle (MIP). The program also contained an algorithm for matching these deposits to CTD tracks. To be classified as a MIP, CAL deposits had to satisfy requirements on the cluster shape and energy distribution, based on which the neural-net-like algorithm of MV compiled a probability, P_{μ}^{MV} , for a MIP to originate from a muon. Muon candidates with a purely CAL-based probability of $P_{\mu}^{\text{MV}} > 0.6$ were reasonably likely to be a true muon, as can be seen in Fig. 5.1.

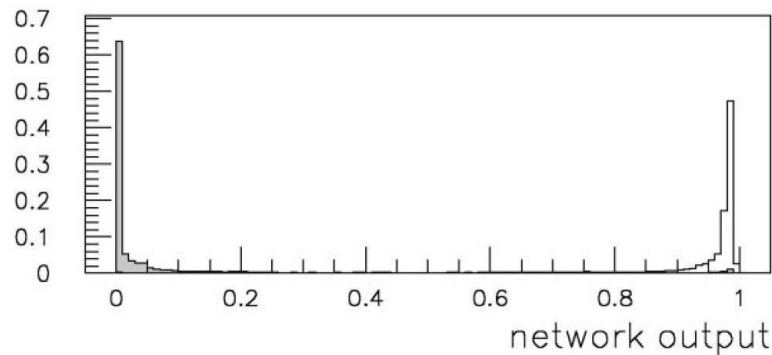


Figure 5.1: The muon finder output, P_{μ}^{MV} , for MC samples of 4×10^5 hadrons (filled histogram) and muons, respectively, with initial energy uniformly distributed in the region of 1–40 GeV [111]. The scale on the vertical axis is arbitrary.

This could be enhanced with an explicit requirement of a matching track, which implied a primary vertex track that, extrapolated to the CAL, matched the MIP within 20 cm. Good muon candidates were MIPs with a probability above 0.6 and with a matching track.

5.2.3 Vertex reconstruction

The event vertex was the point in space from which particles measured in the detector appeared to emanate. More than one vertex could be found in an event for a number of reasons: For example, secondary vertices appeared when long-lived particles were produced and decayed inside the beam-pipe or when particles interacted in the inactive material, e.g. the walls of the tracking devices.

Vertices played an important role in selecting events as they could distinguish between electron-proton interactions that happened close to the expected intersection region of the colliding beams and background processes or badly reconstructed events, in which the vertex was far away from the nominal interaction point. The vertex position was also important in calculating other quantities, for example, the polar angles of the particles, which fed directly into the calculation of the kinematic variables.

The vertex could be fitted by extrapolating tracks measured in the tracking devices back into the beam-pipe and allowing for several vertices. The selection criteria on the event

vertex had to take into account the dimensions of the beam bunches, fluctuations in the position of the beam intersections, background conditions and the different resolutions of the trackers for the x , y and z components of tracks.

The measurement of single W production used the vertex as reconstructed from the CTD tracks [80, 81]. This method could find the z position event-by-event with a resolution of 4 mm, which constrained the vertex well given that along the z direction the spread of the beam was largest and could lie anywhere within a 1 m range. In contrast, the x and y positions of the vertex used mean values averaged over an entire run as the event-by-event resolution of 1 mm in x and y was much larger than the width and height of the beam, which were typically less than 200 μm (see Section 3.1.1).

5.2.4 Event variables

The calorimeter was used to determine most of the kinematic variables. The quantities based on CAL measurements were:

$$E_{\text{tot}} = \sum_i E_i, \quad (5.2)$$

$$p_x^{\text{CAL}} = \sum_i p_{x,i}^{\text{CAL}} = \sum_i E_i \sin \theta_i \cos \phi_i, \quad (5.3)$$

$$p_y^{\text{CAL}} = \sum_i p_{y,i}^{\text{CAL}} = \sum_i E_i \sin \theta_i \sin \phi_i, \quad (5.4)$$

$$p_z^{\text{CAL}} = \sum_i p_{z,i}^{\text{CAL}} = \sum_i E_i \cos \theta_i, \quad (5.5)$$

$$P_T^{\text{CAL}} = \sqrt{(p_x^{\text{CAL}})^2 + (p_y^{\text{CAL}})^2}, \quad (5.6)$$

$$E_T = \sum_i \sqrt{(p_{x,i}^{\text{CAL}})^2 + (p_{y,i}^{\text{CAL}})^2} \quad (5.7)$$

where E_{tot} was the total energy, P_T^{CAL} was the total transverse momentum in the CAL and E_i were individual energy deposits in clusters of CAL cells. The E_i incorporated a correction for energy loss in inactive material and non-uniformity corrections (see Section 5.3). They were combined with the polar angle, θ_i , and azimuthal angle, ϕ_i , which were measured from the event vertex and the geometric centres of the cells.

In the electron decay channel of the W boson, P_T^{CAL} was a measure of the transverse momentum carried away undetected by the neutrino. This was the so called ‘missing’ transverse momentum, P_T^{miss} , i.e.

$$P_T^{\text{CAL}}(ep \rightarrow e' W X, W \rightarrow e\nu) = P_T^{\text{miss}}. \quad (5.8)$$

However, in the muon decay channel of the W a better estimate of P_T^{miss} was obtained by using the muon momentum as measured by the CTD. This was the case because muons are minimum ionising particles (MIPs) and deposited very little energy in the CAL. As a consequence, the CAL measurement of the muon energy carried large uncertainties, which

could lead to a mis-measurement of the neutrino's transverse momentum. To avoid this problem, the muon channel used the variable:

$$P_T^{\text{miss}} = \sqrt{\left(\sum_{i \neq \mu} p_{x,i}^{\text{CAL}} + p_x^{\mu,\text{track}}\right)^2 + \left(\sum_{i \neq \mu} p_{y,i}^{\text{CAL}} + p_y^{\mu,\text{track}}\right)^2}, \quad (5.9)$$

where the sum is over all CAL cells excluding the MIP deposit.

For the same reason, the transverse momentum of the isolated leptons, P_T^l , was measured from the associated calorimeter cluster for electrons but had to be obtained from the CTD measurement for muons.

The hadronic transverse momentum, P_T^X , was obtained from the sum of all calorimeter cells not assigned to an isolated lepton candidate:

$$P_T^X = \sqrt{\left(\sum_{i \neq e, \mu} p_{x,i}^{\text{CAL}}\right)^2 + \left(\sum_{i \neq e, \mu} p_{y,i}^{\text{CAL}}\right)^2} \quad (5.10)$$

Further CAL quantities that were used to reduce the background were:

$$P_T^{\text{ex1IR}} = \sqrt{\left(\sum_{i \neq \text{1IR}} p_{x,i}^{\text{CAL}}\right)^2 + \left(\sum_{i \neq \text{1IR}} p_{y,i}^{\text{CAL}}\right)^2}, \quad (5.11)$$

which was the transverse momentum measured by the CAL excluding the first innermost ring (1IR) in the FCAL and

$$\delta = \sum_i E_i - p_{z,i} = \sum_i E_i (1 - \cos \theta_i), \quad (5.12)$$

where the sum in the expression for δ is over all CAL cells.

The quantity δ is based on longitudinal momentum conservation and peaks at twice the electron-beam energy for well reconstructed NC events. It was used to clean the event selection since particles detected in the FCAL, e.g. from the proton remnant, did not add to δ because of the cancellation of their energy, E_i , with their longitudinal momentum, $p_{z,i}$. Similarly, particles that escaped through the forward beam-hole did not affect this quantity, a fact that was particularly important as the asymmetric beams at HERA deposited most of the energy in the forward region.

The quantity δ depends linearly on individual energy deposits, it therefore allowed to separate out individual components from different parts of the event, for example by rewriting it as

$$\delta = \delta_e + \delta_h = E_e (1 - \cos \theta_e) + \sum_h E_h (1 - \cos \theta_h), \quad (5.13)$$

contributions could be split into those pertaining to the electron and a sum over the energy deposits associated with the hadronic system.

Another useful quantity, which can be calculated from the above quantities, is the polar angle of the hadronic system, γ_h . In the massless approximation γ_h is equivalent to the polar angle of the struck quark. It can be expressed as:

$$\cos \gamma_h = \frac{(P_T^X)^2 - \delta_h^2}{(P_T^X)^2 + \delta_h^2} \quad (5.14)$$

The quantity $V_{\text{ap}}/V_{\text{p}}$ is defined relative to the direction of the total transverse momentum measured in the CAL and represents the ratio of the anti-parallel to parallel CAL contributions along that direction. The numerator and denominator can be expressed as

$$V_{\text{ap}} = - \sum_i \vec{P}_{T,i}^{\text{CAL}} \cdot \vec{\epsilon} \quad \text{for } \vec{P}_{T,i}^{\text{CAL}} \cdot \vec{\epsilon} < 0 \quad (5.15)$$

$$V_{\text{p}} = \sum_i \vec{P}_{T,i}^{\text{CAL}} \cdot \vec{\epsilon} \quad \text{for } \vec{P}_{T,i}^{\text{CAL}} \cdot \vec{\epsilon} > 0 \quad (5.16)$$

where the sum runs over all CAL cells and $\vec{\epsilon}$ is a unit vector along the direction of the total transverse momentum, i.e. $\vec{\epsilon} = \vec{P}_T^{\text{CAL}}/|\vec{P}_T^{\text{CAL}}|$. Events with escaping particles had low values of $V_{\text{ap}}/V_{\text{p}}$, in contrast to well measured NC DIS events, which had values close to unity.

The quantity ξ defined as

$$\xi^2 = 2E'_e E_e (1 + \cos \theta_e), \quad (5.17)$$

was used to distinguish between NC DIS events and single W decay proceeding via the electron channel. In an event of the former type, the scattered lepton could be mis-identified as the isolated lepton and in that case $\xi^2 = Q^2$, where Q^2 is the virtuality of the exchanged boson (see Equation 5.25). Neutral Current events have the highest cross section at low values of Q^2 and hence tended to have small values of ξ^2 , by virtue of which they could be distinguished from single W events with large ξ^2 .

The transverse mass, M_T , was defined as:

$$M_T = \sqrt{2P_T^l P_T^\nu (1 - \cos \phi_{l\nu})}, \quad (5.18)$$

where $\phi_{l\nu}$ was the azimuthal separation of the lepton and neutrino transverse momentum vectors. This quantity was reconstructed to measure the mass of the single W boson decaying via $W \rightarrow l\nu$, but it was expected to produce a value below the true mass because the longitudinal momentum component of the escaping neutrino could not be measured.

The isolated lepton search employed the quantity ϕ_{acop} to distinguish signal events from NC DIS. This angle, shown in Fig. 5.2, was measured in the transverse plane and represented the azimuthal angle between the momentum of the isolated lepton and the vector that balanced P_T^X . It was a powerful tool since inaccurately measured NC DIS events $\phi_{\text{acop}} = 0$, whereas, single W decays produced a neutrino that carried away transverse momentum such that P_T^l and P_T^X did not balance and therefore, produced larger values of ϕ_{acop} .

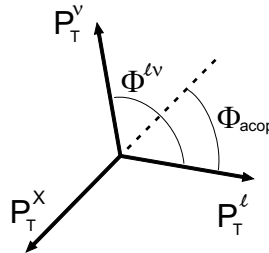


Figure 5.2: The acoplanarity angle in the transverse plane.

A Lorentz invariant measure of the polar angle of a particle was provided by the *rapidity*, y , defined as:

$$y = \frac{1}{2} \ln \frac{E + p_z}{E - p_z} \quad (5.19)$$

where E and p_z are the energy and the longitudinal momentum of the particle. For DIS energies this simplifies to the pseudo-rapidity η

$$y \approx \eta = -\ln\left(\tan \frac{\theta}{2}\right). \quad (5.20)$$

With the aid of this quantity, the distribution of particles in the detector could be expressed in terms of the η - ϕ plane in a Lorentz invariant manner.

5.2.5 Jet finding

Jets were found with the k_T cluster algorithm [113] operating in the inclusive mode [114]. It satisfied the standard condition for a jet finding algorithm to be infra-red safe, i.e. insensitive to soft or collinear gluon emission. This was achieved by using the distance measure d_{ij} between CAL deposits, where

$$d_{ij} = \min(E_i^2, E_j^2) \frac{R_{ij}^2}{R^2} \quad (5.21)$$

and R_{ij} denotes the distance between the deposits in the η - ϕ plane, given by $R_{ij}^2 = (\Delta\eta_{ij})^2 + (\Delta\phi_{ij})^2$ and R is unity. Comparing this distance to the one for a single CAL deposit, $d_i = E_{T,i}^2$, these objects were merged if $d_{ij} < d_i$. Otherwise, they were listed as an identified jet and no further deposits were clustered with it. The algorithm ran until all clusters satisfied $d_i < d_{ij}$, i.e. all jets were identified and there were no remaining deposits to be merged.

The jet properties were calculated according to the Snowmass convention [115]:

$$E_T^{\text{jet}} = \sum_i E_T^i \quad (5.22)$$

$$\eta_{\text{jet}} = \frac{\sum_i \eta_i E_T^i}{E_T^{\text{jet}}} \quad (5.23)$$

$$\phi_{\text{jet}} = \frac{\sum_i \phi_i E_T^i}{E_T^{\text{jet}}} \quad (5.24)$$

with the sum running over CAL deposits associated with the jet and the resultant jet being effectively massless. The jet properties could be related to the underlying partons involved in the hard process of the interaction through a local hadron-parton duality [116].

5.2.6 Reconstruction methods for DIS processes

The ZEUS detector measured four independent quantities that could be used to reconstruct the kinematic variables of a DIS event: the polar angles of the scattered lepton, θ_e , and the hadronic system γ_h , as well as the energies of the scattered lepton, E'_e , and the hadronic

system, E_h . This set of variables¹ offered a redundancy of information for measuring the kinematic variables x , y , Q^2 and s since obtaining two of these four variables allowed to determine the other two using Equations 2.1–2.4.

As a result, there were several different ways in which the kinematic variables could be determined, e.g. using only the electron information (electron method), relying on the measurement of the hadronic system (Jacquet-Blondel method) or employing the polar angles of the electron and the hadronic system (Double Angle method). The following sections outline these different reconstruction methods with their advantages and limitations.

It should be noted that these methods were developed for analysing the kinematics of Neutral and Charged Current events and were therefore not of direct relevance to events of the type of single W boson production. However, some of the variables were used in the event selection (see Section 6.1) in order to reject the background from these DIS events.

Electron method

The electron method [117] reconstructed the kinematic variables of the event by relying on the measurement of the scattered electron:

$$Q_{\text{el}}^2 = 2E_e E'_e (1 + \cos \theta_e) = 4E_e E'_e \cos^2 \frac{\theta_e}{2} \quad (5.25)$$

$$y_{\text{el}} = 1 - \frac{E'_e}{2E_e} (1 - \cos \theta_e) = 1 - \frac{E'_e}{E_e} \sin^2 \frac{\theta_e}{2} \quad (5.26)$$

$$x_{\text{el}} = \frac{Q^2}{s y_{\text{el}}} = \frac{E'_e}{E_p} \cos^2 \frac{\theta_e}{2} \left(1 - \frac{E'_e}{E_e} \sin^2 \frac{\theta_e}{2}\right)^{-1} \quad (5.27)$$

The advantage of this method was that the scattered electron was generally well reconstructed and its energy and polar angle were known with good precision. The shortcomings, on the other hand, are best explained by looking at the behaviour of the measured variables, E'_e and θ_e , across the kinematic plane defined by x and Q^2 . This can be done by using Equations 5.25–5.27 to find an expression for Q^2 as a function of x and one of the measured quantities. The result is:

$$Q^2 = E_e s x \frac{E'_e - E_e}{0.25 s x - E_e^2} \quad (5.28)$$

for E'_e and

$$Q^2 = s x \left(1 + \frac{s x}{4E_e^2} \frac{1 - \cos \theta_e}{1 + \cos \theta_e}\right)^{-1} \quad (5.29)$$

for θ_e . These functions are drawn in Figs. 5.3a and b as isolines (i.e. lines of equal value) of E'_e and θ_e , respectively, in the Q^2 - x kinematic plane. It can be seen that in the kinematic-peak region around $E'_e = E_e$ the electron method didn't perform very well. At the isoline $E'_e = 27.5$ GeV the measurement became independent of Q^2 for any x and around that region isolines were spread far apart, so that a small experimental uncertainty on E'_e translated into a large uncertainty on the kinematic variables. Similarly, the resolution in x was poor for energies above the beam energy, where both E'_e and θ_e were independent of this variable.

¹Any other combination of independent variables, e.g. P_T^X and δ_h as defined in Equations 5.10 and 5.13, could also be used.

The best performance of the electron method was achieved in the region of high y and medium to low Q^2 , where the isolines of the scattered electron energy lay close together and were therefore very sensitive to the measurement. The polar angle of the electron gave also a good handle on the Q^2 across most of the phase space.

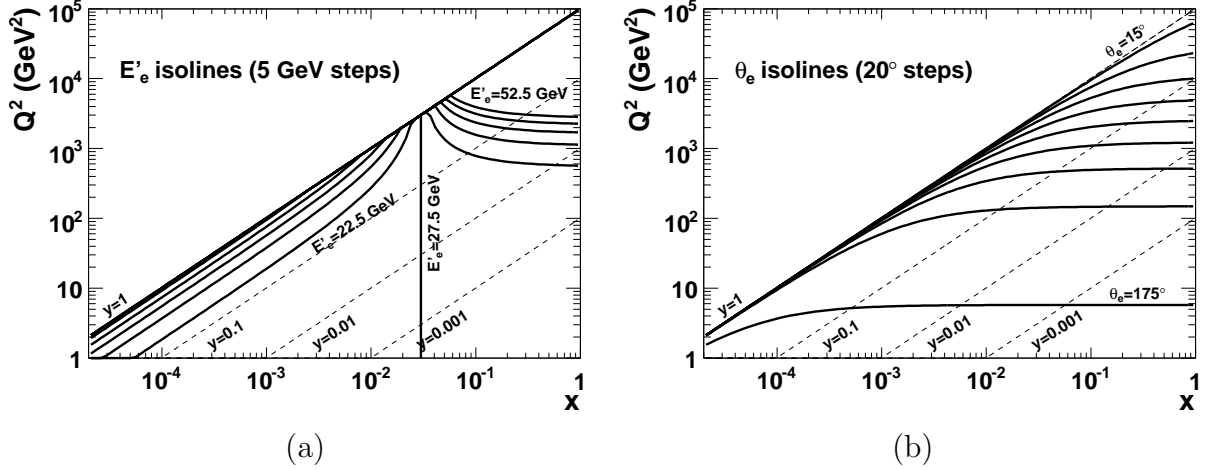


Figure 5.3: Isolines of the scattered electron's energy, E'_e , and polar angle, θ_e in the x - Q^2 kinematic plane [118]. The dashed lines in the background indicate isolines for the kinematic variable y .

Jacquet-Blondel method

The Jacquet-Blondel (JB) method [119] used only the information on the hadronic system to reconstruct the kinematic variables:

$$Q_{\text{JB}}^2 = \frac{(P_T^X)^2}{1 - y_{\text{JB}}}, \quad (5.30)$$

$$y_{\text{JB}} = \frac{\delta_h}{2E_e}, \quad (5.31)$$

$$x_{\text{JB}} = \frac{Q_{\text{JB}}^2}{s y_{\text{JB}}}, \quad (5.32)$$

It was, therefore, particularly well suited for reconstructing Charged Current events, in which the scattered lepton was the neutrino and escaped undetected. For NC events, however, the JB method was not the best choice since the hadronic system was usually not as well measured as the scattered electron.

The behaviour of the two measured variables P_T^X and δ_h across the kinematic plane can be derived using Equations 5.30–5.32 and is given by

$$x = \frac{Q^4}{s(Q^2 - (P_T^X)^2)} \quad (5.33)$$

and

$$Q^2 = 2E_p \delta_h x, \quad (5.34)$$

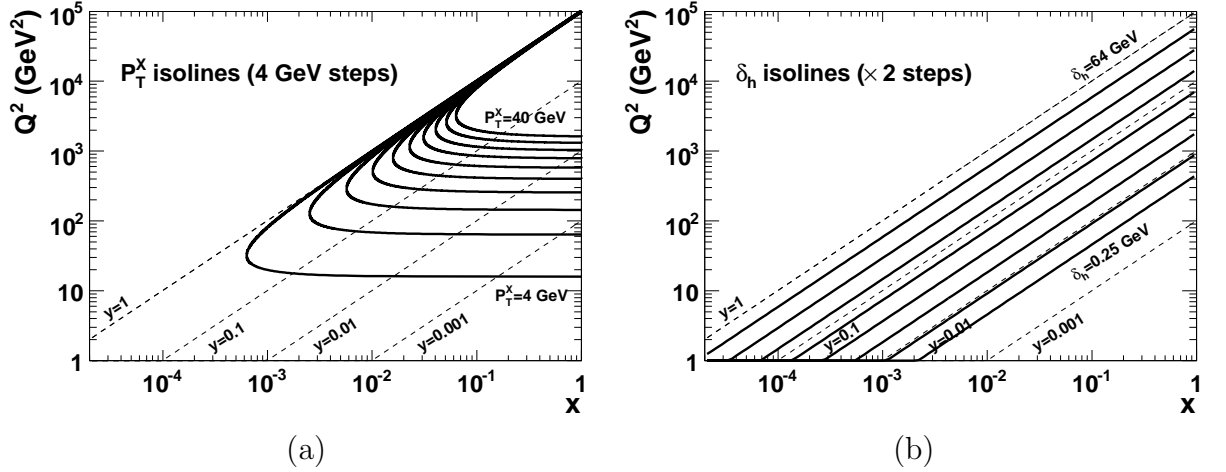


Figure 5.4: Isolines of the hadronic system's transverse momentum, P_T^X , and energy and longitudinal momentum balance, δ_h in the x - Q^2 kinematic plane [118]. The dashed lines in the background indicate isolines for the kinematic variable y .

respectively. Isolines for these quantities are shown in Figs. 5.4a for P_T^X and 5.4b for δ_h . At medium and high Q^2 , the hadronic transverse momentum had good sensitivity to Q^2 but was independent of x . The quantity δ_h , on the other hand, gave a good coverage of the kinematic plane and a direct measurement of y .

Double Angle method

The Double Angle method (DA) [117] reconstructed the kinematic variables solely with the aid of the polar angles of the scattered lepton and the hadronic system:

$$Q_{DA}^2 = 4E_e^2 \frac{\sin \gamma_h (1 + \cos \theta_e)}{\sin \gamma_h + \sin \theta_e - \sin(\theta_e + \gamma_h)}, \quad (5.35)$$

$$y_{DA} = \frac{\sin \theta_e (1 - \cos \gamma_h)}{\sin \gamma_h + \sin \theta_e - \sin(\theta_e + \gamma_h)}, \quad (5.36)$$

$$x_{DA} = \frac{E_e \sin \gamma_h + \sin \theta_e + \sin(\theta_e + \gamma_h)}{E_p \sin \gamma_h + \sin \theta_e - \sin(\theta_e + \gamma_h)}, \quad (5.37)$$

$$(5.38)$$

This guaranteed that the DA method was insensitive to the uncertainties on the CAL energy scale and could consequently be used for calibration. This was particularly useful given that angles could generally be measured with higher precision than energies and by taking ratios of the angles the uncertainty on the less well constrained γ_h cancelled. Using the relationship between Q^2 and E'_e , given in Equation 5.25, and comparing it to Equation 5.35, one arrives at an expression for the scattered electron energy as determined by the DA method:

$$E_{DA} = \frac{Q_{DA}^2}{E_e(1 + \cos \theta_e)}. \quad (5.39)$$

The ratio of this quantity to the electron energy measured in the CAL could be used to derive correction factors for the electron energy in different regions of the calorimeter [120] (see Section 5.3).

Further advantages of the DA method can be seen in Fig. 5.5b, which shows isolines of γ_h given by:

$$Q^2 = s^2 x^2 \left(4E_e^2 \frac{1 + \cos \gamma_h}{1 - \cos \gamma_h} + s x \right)^{-1} \quad (5.40)$$

obtained from Equations 5.35–5.37. It shows that the quantity γ_h had a good coverage everywhere apart from the high- x region. The DA method did not give the best resolution in either Q^2 or x , but combined with θ_e (see Fig. 5.3b) it gave the best resolution on both across most of the kinematic plane. The exceptions to this were the region of low Q^2 and DIS events at the very highest y , where isolines of the angles ran indistinguishably close together and small experimental errors translated into large errors on the kinematic variables.

For completeness, Fig. 5.5a shows the behaviour across the kinematic plane of another measurable variable, E_h , given by:

$$Q^2 = s x \frac{E_h - E_p x}{E_e - E_p x} \quad (5.41)$$

As can be seen in the plot, this variable is not as useful as the others in determining the kinematics. At and above the electron beam energy it is insensitive to Q^2 but measures x very well. However, below this threshold it carries too much ambiguity with regards to these variables.

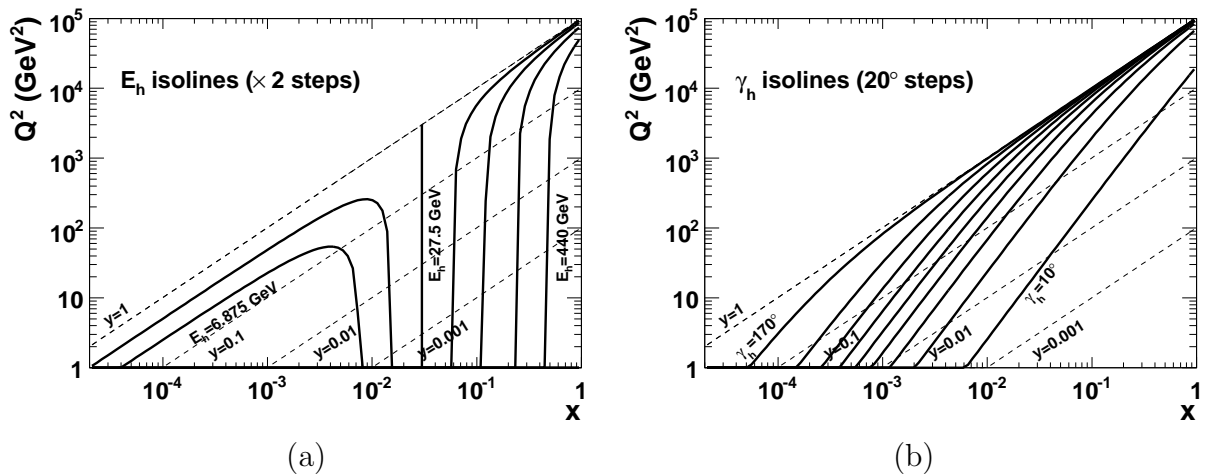


Figure 5.5: Isolines of the hadronic system's energy, E'_h , and polar angle, γ_h in the x - Q^2 kinematic plane [118]. The dashed lines in the background indicate isolines for the kinematic variable y .

5.3 Corrections

Several corrections were applied to the raw energy measurements delivered by ZEUS to correct for known effects in the detector. The following sections explain these corrections.

5.3.1 Calorimeter noise

The calorimeter measurements had to be corrected for the natural radioactivity of the uranium it contained. This background was eliminated by removing EMC cells with less than 60 MeV and HAC cells below a threshold of 110 MeV [121–123].

Additionally, small electrical discharges in individual PMTs, termed calorimeter sparks, could be masked with the aid of the energy imbalance between the two PMTs that read out a cell. Isolated cells were removed from the energy measurement on an event-by-event basis if $E_{\text{cell}} < 1$ GeV and the energy imbalance satisfied $|E_{\text{PMT1}} - E_{\text{PMT2}}| > 0.49E_{\text{cell}} + 0.03$ GeV, where $E_{\text{cell}} = |E_{\text{PMT1}} + E_{\text{PMT2}}|$. Furthermore, isolated cells reading out less than 0.08 (0.14) GeV in the EMC (HAC) were also ignored [121–123].

Noise in the readout electronics and faulty PMTs gave rise to so called *hot cells* that provided consistently bad measurements. These could be identified on a run-by-run basis by comparing events collected from unpaired electron or proton pilot bunches (see Section 3.1.1) with a random FLT pass-through trigger. Cells that fired in such a selection with a probability five standard deviations above the mean of all cells from the same CAL section (i.e. FCAL, BCAL or RCAL) were rejected. For the BCAL the procedure was repeated by recalculating the mean after the first set of hot cells had been removed. Cells that had a low frequency of firing but fluctuated to large energies were removed by a similar statistical requirement in energy, which rejected cells whose mean energy calculated over a pass-through sample was over five standard deviations above the mean of all cells [123].

The removal of hot cells was not undertaken for the first inner ring of the FCAL and RCAL as it would have deteriorated the efficiency of the beam-gas rejection algorithm (see Section 5.5.2) [124].

5.3.2 Electron corrections

It was particularly important to measure electrons as well as possible since the event selection (Section 6.1) put several constraints on their properties and without appropriate corrections the pass rate would have been different in data (affected by detector effects) than in MC (unaffected by unmodelled detector effects).

Therefore, three corrections were dedicated to the electron energy measurement in the CAL, namely, dead-material, non-uniformity and presampler corrections.

Dead-material corrections

For the measurement of particle energies it was important that the inactive material (termed ‘dead’ material) between the interaction point and the CAL was taken into account since particles could lose energy or be absorbed before they reached the calorimeter. Therefore, a precise map of the inactive regions within ZEUS and the material that they contained was implemented in the MC and was also used to correct the data. For electrons, the corrections were dependent on the angles θ_e , ϕ_e and the energy of the electron, as well as the z -position of the vertex [125].

Non-uniformity corrections

The division of the CAL into towers and modules lead to a non-uniformity in its response. Particles could deposit part or all of their energy in the gaps between the CAL cells along z or in the wavelength shifters between the modules along ϕ . In the former case, the energy was underestimated since some energy disappeared undetected in the material filling the gaps. In contrast, electrons showering in the wavelength shifters amplified the signal and caused the CAL to overestimate their energy.

Dead material, described above, caused electrons to shower before they reached the calorimeter and could smear out the effect of CAL non-uniformities, therefore, the corrections that took account of non-uniformities were applied after correcting for dead material.

The non-uniform response of the CAL was measured by comparing the electron energy calculated independently with the Double Angle method, E_{DA} , to the electron energy obtained from the CAL and corrected for the dead material, E_{cor1} [126]. As an example, the ratio of these two quantities is shown for MC positrons in the BCAL in Fig. 5.6a with respect to the distance to the module edge (DME) and in Fig. 5.6b with respect to the distance to the cell edge (DCE).

As expected, the ratio dips in the region close to the module edge, reflecting the fact that the electron deposited energy in the light-guides, which lead to an over-estimation of the energy. (The double-peak is a geometrical effect due to the fact that the CAL modules were rotated in azimuth by 2.5° - see Section 3.2.1 - and included not only light-guides but also some dead material.) Similarly, the ratio increases towards DCE=0 as larger fractions of the electron energy were absorbed in the dead material between cells. Correction functions, based on fits to distributions like these, adjusted the electron energy for non-uniformity effects in data and MC.

Presampler corrections

Corrections using the presampler (see Section 3.2.2) were a more refined attempt to adjust the electron energy for showering in inactive material than the dead material corrections, described above. They were based on the fact that minimum ionising particles (MIPs) were produced when electrons interacted with the dead material. The energy of the resultant shower was proportional to the number of MIPs, so by recording the number of these MIPs with the presampler the measurement of the electron energy could be adjusted for energy loss outside the CAL [127].

5.4 Hadronic corrections

Several corrections were applied to the measurement of the hadronic final state by a routine called CORANDCUT [128]. The effects that it took into account are described below.

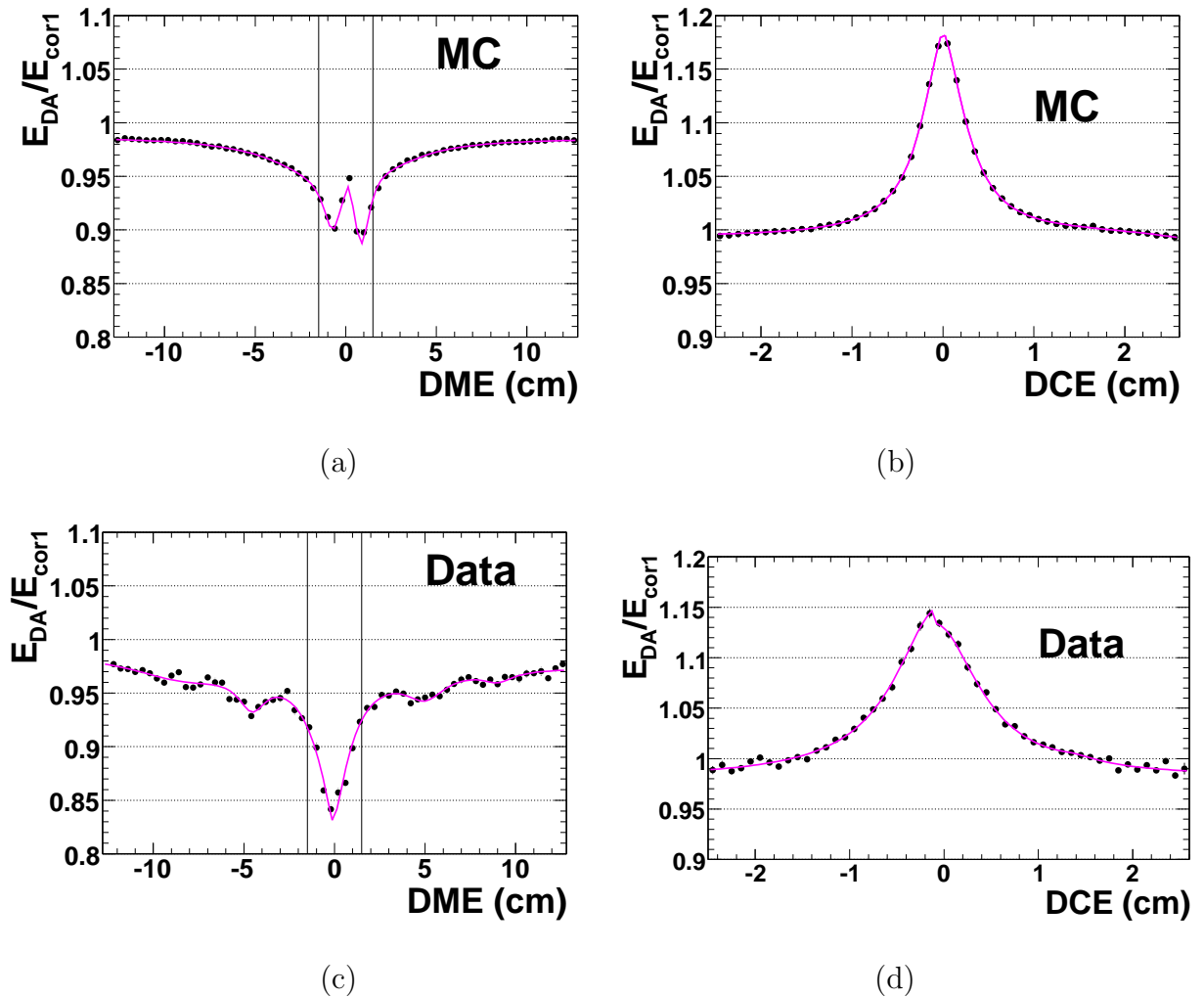


Figure 5.6: The mean of the Gaussian fit to the E_{DA}/E_{cor1} distribution versus (a) DME and (b) DCE for positrons in Monte Carlo and correspondingly for data in (c) and (d) [120]. The error bars on the points represent the error on the Gaussian mean and are smaller than the marker size.

Dead-material corrections

Information on the inactive material in the detector was based on the same dead-material map as used for electrons (see Section 5.3.2). However, for the hadronic final state the corrections were not particle-specific but were obtained from MC simulations and averaged over all particle types [128].

Low-energy corrections

Before the calorimeter was put into ZEUS, data were taken at a test-beam facility. They showed that the energy estimated by the CAL was 60% higher if deposits occurred via ionisation instead of shower development [129]. This effect was modeled with MC simulations and correction factors implemented in CORANDCUT [128].

Calorimeter-gap corrections

There were relatively large gaps between the FCAL and the BCAL that were filled by the support structure and miscellaneous services connecting the interior of the detector to the outside. In the case of the scattered electron, the gap in the detector was straightforward to take into account since the electron's CTD track could be used to reject events, in which the electron disappeared into the gap region.

The hadronic final state, however, contained neutral particles and hence the hadronic energy deposited in the gap had to be estimated by other means. Furthermore, the simulation of neutron production carried large uncertainties. So to avoid biasing the result, the correction method had to be data-driven, i.e. avoid the use of MC 'truth' information, in order that the same procedure could be applied to MC and data.

Neutral current data and MC samples were used to derive the corrections [128]. A subset of events containing very collimated one-jet events was selected, in which all deposits satisfied $|\theta_i - \gamma_h| < 0.25$ rad.

The 'energy of the struck quark', defined by

$$E_q = \frac{P_T^X}{\sin \gamma_h},$$

was estimated and compared to the equivalent quantity from the Double Angle (DA) method, where

$$E_q^{\text{DA}} = \frac{P_{T,DA}^X}{\sin \gamma_h}, \quad P_{T,DA}^X = \sqrt{Q_{\text{DA}}^2 (1 - y_{\text{DA}})}.$$

The ratio of the two estimates of the quark energy plotted versus γ_h showed clear deviations in the region of the calorimeter gap. A fit to the behaviour of this graph in the gap region was then used to correct the hadronic final state depending on the hadronic angle γ_h .

Back-splash corrections

The term *back-splash* was used for particles of the hadronic system that scattered off the material in the detector and entered the CAL far away from the rest of the jet. These deposits could make large contributions to δ_h since the $E - p_z$ value increased towards the rear of the detector.

In order to suppress back-splash, clusters of deposits in the CAL (not associated with the scattered lepton) were removed if they were not associated to a primary-vertex track, their energy was less than 3 GeV and their polar angle satisfied $\theta > \gamma_{\text{max}}$, where γ_{max} was a threshold polar angle tuned to data and MC, given by [128]:

$$\gamma_{\text{max}} = \begin{cases} 0.151 + 1.372 \gamma, & \gamma < 1.95 \text{ rad} \\ 2.826 + 0.259 (\gamma - 1.95), & \gamma > 1.95 \text{ rad} \end{cases}$$

In the above expression γ represents the hadronic angle and was calculated iteratively from all deposits in the first instance and at subsequent stages excluding the back-splash candidates. Up to three such iterations were conducted until the change in γ_{max} between steps dropped below 1%.

5.5 Backgrounds

There were several types of background that did not originate from ep interactions but could fake such events by producing tracks inside the CTD and by depositing energy inside the CAL that could be misidentified as an electron or muon from a DIS event. As these background events didn't emanate from the ep interaction point, *fake* missing transverse momentum was often reconstructed. This allowed them to pass a crucial selection criterion for single W events.

The removal of this contamination was particularly difficult because these processes did not only occur on their own but could also be overlaid on top a genuine ep event, e.g. see Fig. 5.7d. Special selection criteria were devised to eliminate them, but in a few cases only an eye-scan of the selected events could reject the remaining obvious fakes. The major types of background and the measures employed to remove them are detailed below. There was no Monte Carlo simulation available for these processes.

5.5.1 Cosmic muons

Cosmic muons were produced when highly energetic particles from the Sun or other cosmic sources interacted with nuclei of the Earth's atmosphere. Pions and kaons were produced in such interactions, which then predominantly decayed to muons and muon-neutrinos. The muons themselves decayed via the weak interaction with a long proper lifetime, which was significantly Lorentz dilated by the very high energies they could carry. Consequentially, many cosmic muons reached the Earth's surface where they could penetrate large amounts of matter without undergoing significant multiple scattering.

Cosmic muons recorded by ZEUS needed to have high energies to reach the detector 23m below ground. Therefore, their typical signature, shown in Fig.5.7a, was a very straight track inside the CTD. In the CAL the deposits of cosmic muons were small since muons are minimum ionising particles and mostly deposit energy through Bremsstrahlung. However, in the case of cosmic showers the deposits in the CAL could also be significant, see Fig.5.7b.

Cosmic muons shower the Earth continuously with a very high rate. So the first step in dealing with this background was to restrict the timing of events to a small window of several nanoseconds around the beam crossing, as given by the HERA clock (see Section 3.1). A simple requirement to reject cosmic muons within this window was to remove events containing two muons with associated tracks back to back within certain angular limits. Unfortunately, this only removed well reconstructed events of this type.

By restricting the event's primary vertex position in z to a region in the centre of the detector, events far from the nominal interaction point could be filtered out. The vertex constraint had to take into account the beam dimensions and the natural variation in the ep vertex hence it was only applied in z and not tighter than 50 cm (HERA I) or 30 cm (HERA II) around the nominal interaction point.

Most cosmic muons traversed the ZEUS detector from above and close to the vertical direction since at shallower angles the path length through the Earth and hence the probability of absorption increased rapidly. This could be exploited for a rejection criterion since

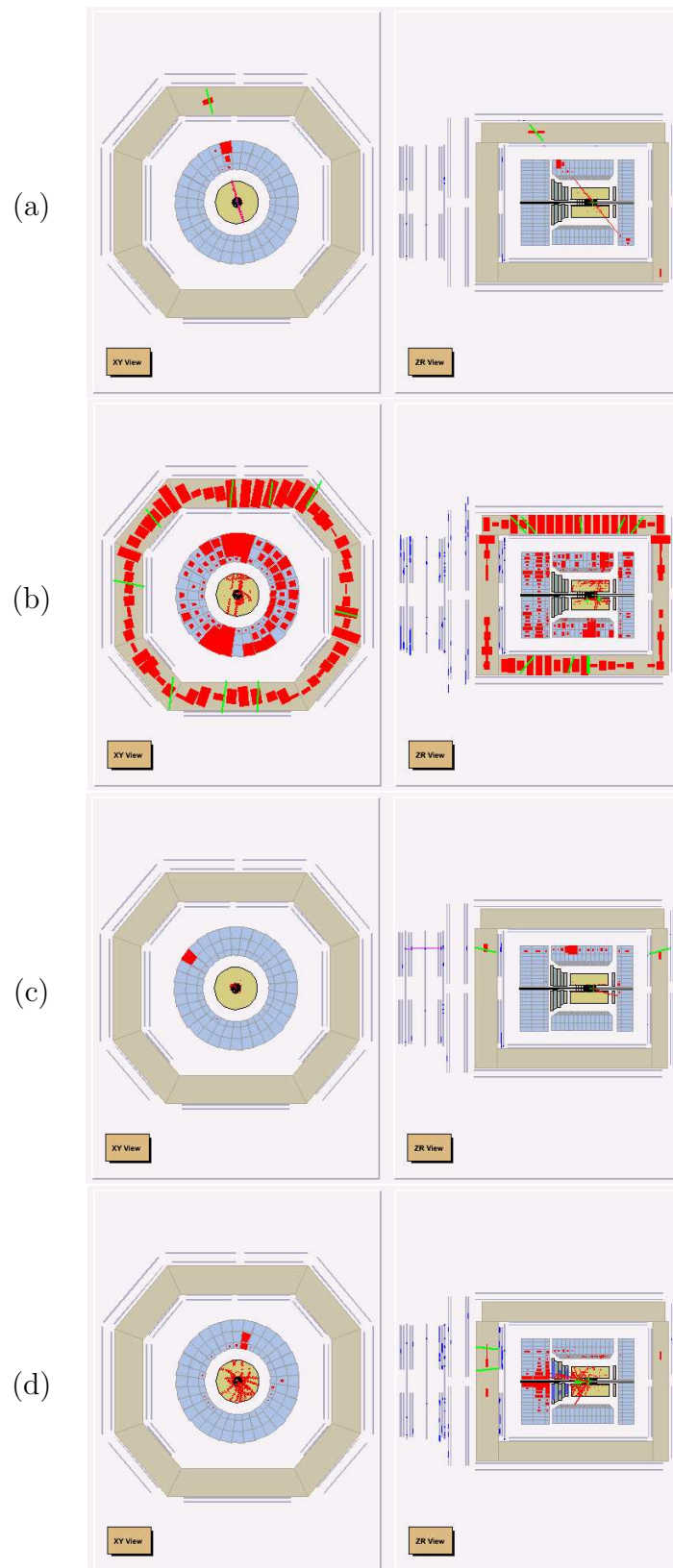


Figure 5.7: Examples of background events: (a) cosmic muon, (b) cosmic shower, (c) halo-muon, (d) halo-muon and ep event.

relativistic muons required 10 ns to travel the roughly 3 m to cross the ZEUS calorimeter, the difference in CAL timing between the lower and upper halves of the BCAL had to be less than 10 ns. Events from the ep interaction passed this requirement since their timing for both sides of the CAL was roughly equal.

5.5.2 Beam-gas interactions

Beam-gas interactions occurred when the electron or proton beams interacted with residual gas molecules inside the evacuated beam-pipe. These interactions could occur because the vacuum in the beam-pipe was evidently not perfect but had a residual pressure of 10^{-9} bar [130].

Most beam-gas events inside the detector were suppressed by a minimum requirement on P_T^{miss} . Furthermore, proton beam-gas events could be rejected by the Veto Wall, provided they occurred upstream from the ZEUS detector. Otherwise, they led to very forward boosted secondary particles that deposited all of their energy in the inner rings of the FCAL. Thus, a constraint on the transverse momentum of the event excluding the first inner ring, P_T^{ex1IR} , could help to reject these events. Additionally, proton beam-gas events lacked a scattered electron so a minimum requirement on the quantity δ , e.g. $\delta > 35$ GeV, could help clean the selection.

Generally, beam-gas interactions created a large number of tracks, many of which were low momentum and far away from the nominal interaction point. Exploiting these characteristics, beam-gas events could be suppressed with a restriction on the z position of the vertex and a condition on the relation between the number of ‘good’ tracks, $N_{\text{trk}}^{\text{good}}$, defined as associated with the primary vertex with a momentum above 0.2 GeV, and the total number of tracks in the event, N_{trk} .

5.5.3 Halo-muons

Halo muons were produced either by proton beam-gas interactions or by stray protons from the proton beam halo hitting the material of the accelerator, for example, the bending magnets about 360 m upstream from ZEUS. Such interactions produced pions and kaons, which subsequently decayed to muons. The muons could reach the ZEUS detector if they traveled parallel to the beam-line.

As a consequence, halo-muons recorded by ZEUS entered from the rear of the detector traveling along the z direction at some distance to the beam-line, see Fig. 5.7c for a typical event. If a halo-muon passed through the CAL the event could be reconstructed to have large fake P_T^{miss} .

A restriction on the global calorimeter timing of events, as used for cosmic muons, was not effective against halo-muons, since most of them passed the detector at the same time as the proton beam and therefore fell within the data taking window. However, requiring the calorimeter timing difference between the FCAL and the RCAL to be less than 10 ns could be used to remove these events.

Chapter 6

Isolated leptons and single W boson production

This chapter describes the search for events containing isolated leptons and large missing transverse momentum. The event selection is explained in Section 6.1 and the number of data events, which match these characteristics, is compared to the MC expectation in Section 6.2. The data samples used for the search and their integrated luminosities are listed in Table 3.1. The Standard Model process of single W boson production has the same characteristics as the events selected by this search. Therefore, the samples were used for obtaining the production cross section of single W bosons, a measurement that is detailed in Section 6.3.

Several other Standard Model processes contributed to the isolated lepton search and to the cross section measurement by imitating the signature of single W events:

- **Neutral Current DIS**, where the scattered beam electron was identified as the isolated lepton and a mis-measurement of the proton remnant lead to the reconstruction of fake P_T^{miss} .
- **Charged Current DIS**, in which genuine P_T^{miss} was due to the escaping neutrino and a fake lepton was detected due to mis-identification of a particle from the hadronic final state.
- **Lepton pair production**, in the case where one of the genuine leptons was identified but fake large P_T^{miss} resulted from mis-measurement of the second lepton or the proton remnant. Tau pair production contributed if one or both of the taus decayed leptonically, which lead to genuine isolated leptons as well as genuine P_T^{miss} .
- **Photoproduction** could contribute if a particle of the hadronic final state mimicked the signature of an isolated lepton and mis-measurement lead to large fake P_T^{miss} .

The background processes not related to the main electron-proton interaction, described in Section 5.5, also contributed to the event selection as they typically contained isolated leptons and often also P_T^{miss} .

Variable	Electron	Muon
δ	$5 < \delta < 50$ GeV	< 70 GeV
P_T^{exlIR}	> 9 GeV	> 9 GeV
P_T^{CAL}	> 12 GeV	> 12 GeV
P_T^{miss}	> 12 GeV	> 12 GeV
P_T^X	—	> 12 GeV
ξ_l^2	> 5000 GeV ² for $P_T < 25$ GeV	—
ϕ_{acop}	$> 20^\circ$	$> 10^\circ$
$V_{\text{ap}}/V_{\text{p}}$	< 0.5 (< 0.15 for $P_T^e < 25$ GeV)	< 0.5 (< 0.15 for $P_T^{\text{CAL}} < 25$ GeV)
P_T^l	> 10 GeV	> 10 GeV
θ_l	$15^\circ < \theta_e < 120^\circ$	$15^\circ < \theta_\mu < 120^\circ$
D_{track}	> 0.5 for $\theta_e > 45^\circ$	> 0.5
D_{jet}	implicit	> 1.0
# isolated μ	0	1

Table 6.1: Event requirements for the isolated electron and muon search.

In the following, the term *signal* refers to events with genuine isolated leptons and genuine large P_T^{miss} , whereas, other physics backgrounds and non-*ep* processes that merely imitated these features are termed *background*.

6.1 Event selection

The following event selection was applied to both the ZEUS data and the MC samples described in Section 4.4–4.7, with the exception of the requirement on the Calorimeter timing (see details below). Events containing isolated electrons were treated separately from those containing isolated muons, but unless specified, the requirements were applied to both. The value of the requirements was chosen such that it maximised the ratio of signal to the background in the selection. A short description of every criterion outlines how it was expected to reduce the number of background events whilst enhancing the signal. The main offline selection criteria are summarised in Tab. 6.1.

- **Trigger**

Candidate events were selected using several trigger slots at the level of the FLT, SLT and TLT. An event was accepted if it fired at least one slot on every trigger level. However, the offline selection requirements, listed below, were more stringent than the online trigger thresholds.

- **Calorimeter timing**

Constraints on the calorimeter timing were used to reject cosmics and beam-gas events in data (see Sec.5.5). Events had to be recorded within a 6 ns window around the bunch crossing, as given by the HERA clock, thereby removing off-time events. Furthermore, the first deposits recorded by opposite sides of the CAL also had to be less than 6 ns apart, thus rejecting cosmics and halo-muon events that typically took about 10 ns to

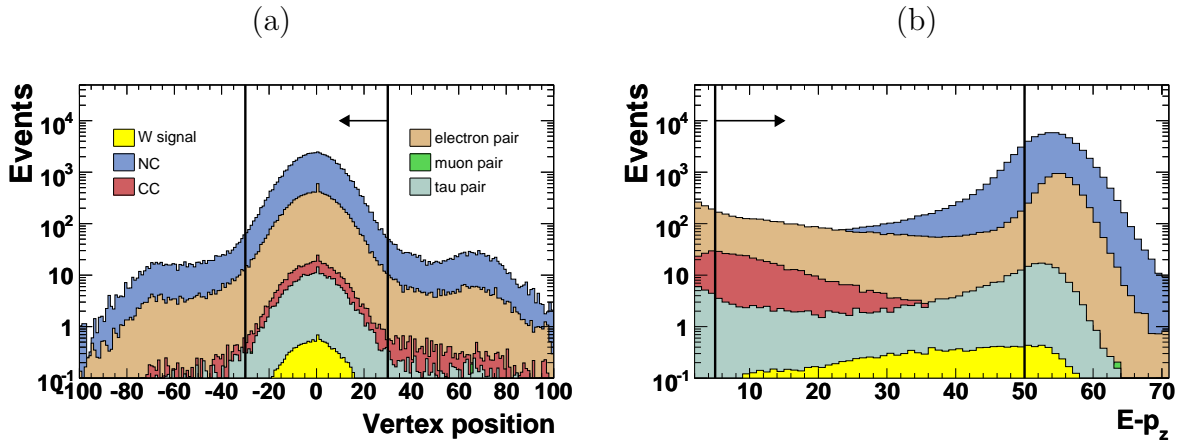


Figure 6.1: Distribution of MC events in the isolated electron search for the quantities Z_{vtx} and $E - p_z$. The the W signal MC only comprises the electron decay channel of the W boson in these plots.

traverse the CAL at near the speed of light. No such requirements were applied to the MC because the calorimeter timing was not simulated.

- **Cosmic rejection**

Cosmic muons were further suppressed by rejecting events, in which two muon tracks were found back-to-back within 10° in both θ and ϕ . Events that contained only two tracks but two or more muons were also removed.

- $N_{\text{tracks}}^{\text{good}} > a * (N_{\text{tracks}} - 20)$

The relationship between the numbers of good tracks, $N_{\text{tracks}}^{\text{good}}$, defined as those associated with the primary vertex carrying a momentum above 0.2 GeV, and the total number of tracks in an event, N_{tracks} , helped to remove beam-gas interactions. These produced an abundance of low momentum tracks that could emanate from anywhere inside the beam-pipe. The condition on the relation between $N_{\text{tracks}}^{\text{good}}$ and N_{tracks} had to be tightened for the HERA II running periods. This was due to the addition of dead material in the ZEUS upgrade that increased the total number of tracks, whilst keeping the number of good tracks from ep interactions constant. In the analysis this was implemented by using a different value for the coefficient a in the two running periods, such that $a = 0.2$ for HERA I and $a = 0.25$ for HERA II. Additionally, in HERA II the definition of N_{trks} was narrowed to include only tracks with $P_T > 0.1$ GeV that passed superlayer 3 in the CTD.

- Z_{vtx}

Constraining the z -position of the reconstructed primary vertex removed non- ep events that were produced far away from the nominal interaction point. Events were accepted within a window of $|Z_{\text{vtx}}| < 50$ cm, which was tightened to 30 cm for events from HERA II to counteract the increase in the number of background tracks that could lead to a false reconstructed vertex. The Z_{vtx} distribution of the relevant SM Monte Carlos is shown in Fig. 6.1 a.

- $E - p_z$

The difference between the total energy and the total longitudinal momentum measured

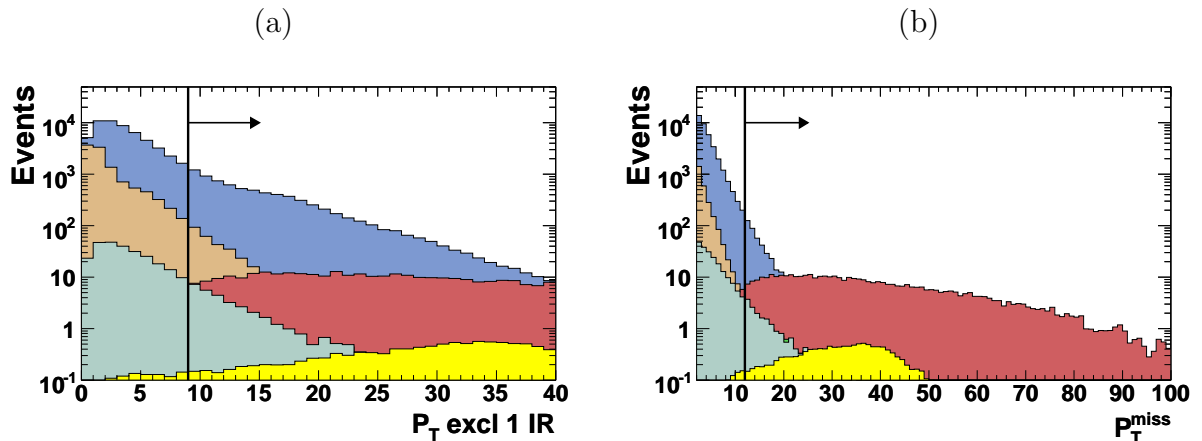


Figure 6.2: Distribution of MC events in the isolated electron search for the quantities P_T^{exl1IR} and P_T^{miss} . The W signal MC only comprises the electron decay channel of the W boson in these plots. The legend of Fig 6.1 applies.

by the CAL, denoted δ (see Eqn. 5.12), was used to discard NC DIS and non- ep events. For well measured NC DIS events, δ peaked at twice the electron-beam energy $2E_e = 55$ GeV, see Fig. 6.1 b. It fluctuated to larger values in cases where the CAL overestimated the energy, e.g. due to CAL sparks (see section 5.3.1), or where a NC DIS event was overlayed on top of non- ep background that deposited energy in the RCAL. On the other hand, very small values could occur as a consequence of holes or dead cells in the CAL (see section 5.3.1) or in the case of proton-beam-gas events since such events lacked a scattered electron.

In contrast, events containing a single W could have any value of δ up to about 60 GeV, as shown in Fig. 6.1 b. So, to remove a sufficient number of background events without losing too much of the signal, δ was restricted to $\delta < 70$ GeV for the muon channel and was tightened in the electron channel to $5 < \delta < 50$ GeV to remove the NC background and proton-beam-gas events that affected the electron channel.

- $\mathbf{P_T^{\text{exl1IR}}}$

It was required that $P_T^{\text{exl1IR}} > 9$ GeV, in order to select events away from the trigger threshold at 7 GeV and to suppress events, in which large P_T^{miss} arose from a mis-measurement of the proton remnant. How this constraint affected the different Monte Carlo contributions can be seen in Fig. 6.2 a.

- $\mathbf{P_T^{\text{miss}}}$

The overall transverse momentum imbalance of the event had to be above 12 GeV. This constraint removed all photoproduction events and a large amount of the lepton pair and NC DIS backgrounds, as can be seen in Fig. 6.2 b.

- $\mathbf{P_T^X}$

The hadronic transverse momentum was required to satisfy $P_T^X > 12$ GeV in the muon channel due to a trigger threshold, which prevented the measurement of muon events below that value.

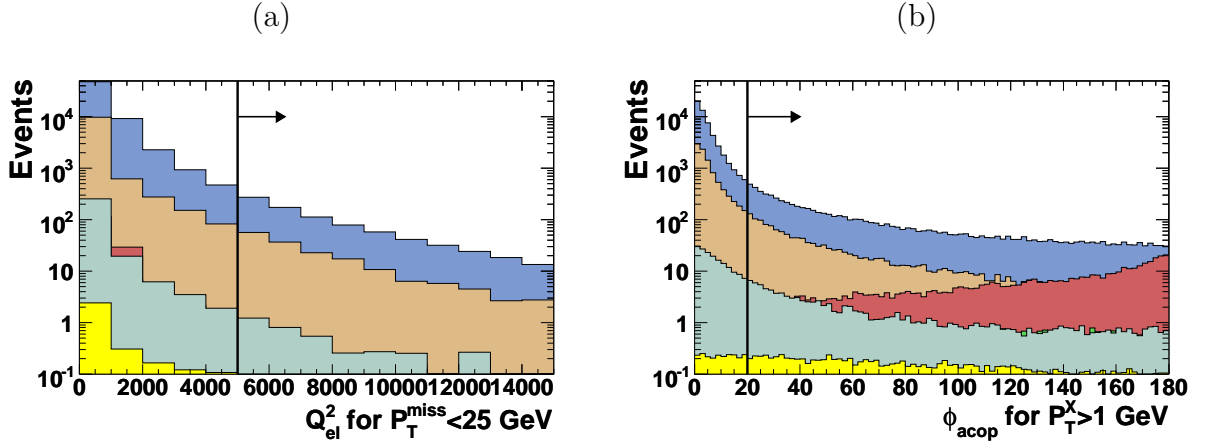


Figure 6.3: Distribution of MC events in the isolated electron search for the quantities ξ_e^2 ($= Q_{el}^2$ for NC) and ϕ_{acop} . The W signal MC only comprises the electron decay channel of the W boson in these plots. The legend of Fig 6.1 applies.

- ξ_e^2
In the electron channel, Neutral Current DIS formed a large background in the region $P_T^{\text{miss}} < 25$ GeV, see Fig. 6.3 a, whilst being negligible in the muon channel (c.f. Table 6.4). This background was controlled by requiring $\xi_e^2 > 5000$ GeV² for events with $P_T^{\text{miss}} < 25$ GeV. The criterion exploits the fact that for NC events $\xi_e^2 = Q^2$, where Q^2 denotes the virtuality of the exchanged boson. So it suppresses NC processes at low Q^2 , where the cross section increases rapidly with Q^{-4} .
- ϕ_{acop}
In the muon channel, the lepton pair and NC DIS backgrounds were further suppressed by requiring that $\phi_{acop} > 10^\circ$, see Fig. 6.3b. In the electron channel, where the NC background was more significant, this was tightened to $\phi_{acop} > 20^\circ$ for events with a well defined P_T^X above 1 GeV, otherwise the requirement was dropped, since ϕ_{acop} relies on a well reconstructed P_T^X .
- V_{ap}/V_p
The azimuthal momentum balance in the event had to satisfy $V_{ap}/V_p < 0.5$ to reduce the NC DIS background in the electron channel and the lepton pair background in the muon channel. A more stringent condition of $V_{ap}/V_p < 0.15$ was applied in the high-background regions of $P_T^e < 25$ GeV in the electron channel and $P_T^X < 25$ GeV in the muon channel.

It was required that an electron or a muon candidate was found in the event with the EM (see Section 5.2.1) or MV finder (see Section 5.2.2), respectively. The following selection criteria were then applied to ensure that the candidate was isolated and well reconstructed:

- **Candidate probability**
The lepton identity was selected with an EM electron probability of $P_{EM}^e > 0.001$ (Fig. 6.5 a) or an MV muon probability of $P_{MV}^\mu > 0.6$. Above these thresholds the candidate was very likely to be an electron or a muon, respectively. The probability threshold of EM is two orders of magnitude smaller than that of MV due to the different

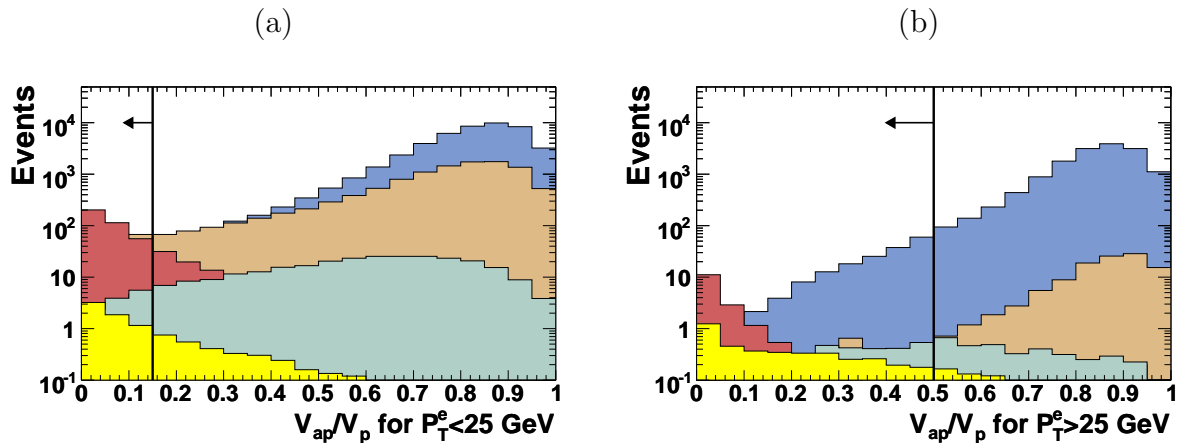


Figure 6.4: Distribution of MC events in the isolated electron search for the quantity V_{ap}/V_p below and above the P_T^e threshold. The W signal MC only comprises the electron decay channel of the W boson in these plots. The legend of Fig 6.1 applies.

methods used to compute the overall candidate probability, described in Sections 5.2.1 and 5.2.2, respectively. MV provides a single overall probability, whereas EM computes several subprobabilities from the signature of the candidate and takes the product of these to obtain the final candidate probability.

- P_T^l

The lepton momentum had to satisfy $P_T^l > 10$ GeV, see Fig. 6.5 b ¹ For electrons this was measured by the CAL, whereas for muons P_T^l was obtained from the track measurement in the CTD.

- **Lepton track**

The lepton candidate had to have a matching CTD track that originated from the primary vertex. In HERA II, where the non- ep background was higher, the track also had to pass the third CTD superlayer.

- $P_T^{e, \text{trk}}$

The electron track, Fig. 6.5 c, had to satisfy $P_T^{e, \text{trk}} > 5$ GeV in order to reject low-momentum electrons that passed the above P_T^l cut because of a mis-measurement in the CAL.

- **DCA**

To avoid mismatching the electron track, to e.g. a CAL deposit of a photon, the distance of closest approach of the track to the EMC cluster had to be less than 10 cm, as shown in Fig. 6.5 d.

- E_e

Reflecting the requirement on the electron transverse momentum and to avoid noisy cells and other fluctuations in the CAL, the electron's energy (corrected for dead material, non-uniformity etc as described in Section 5.3.2) was required to be at least 8 GeV, see Fig. 6.5 e.

¹The histogram of the W signal only contains the electron channel. However, the corresponding plots for the muon channel look very similar.

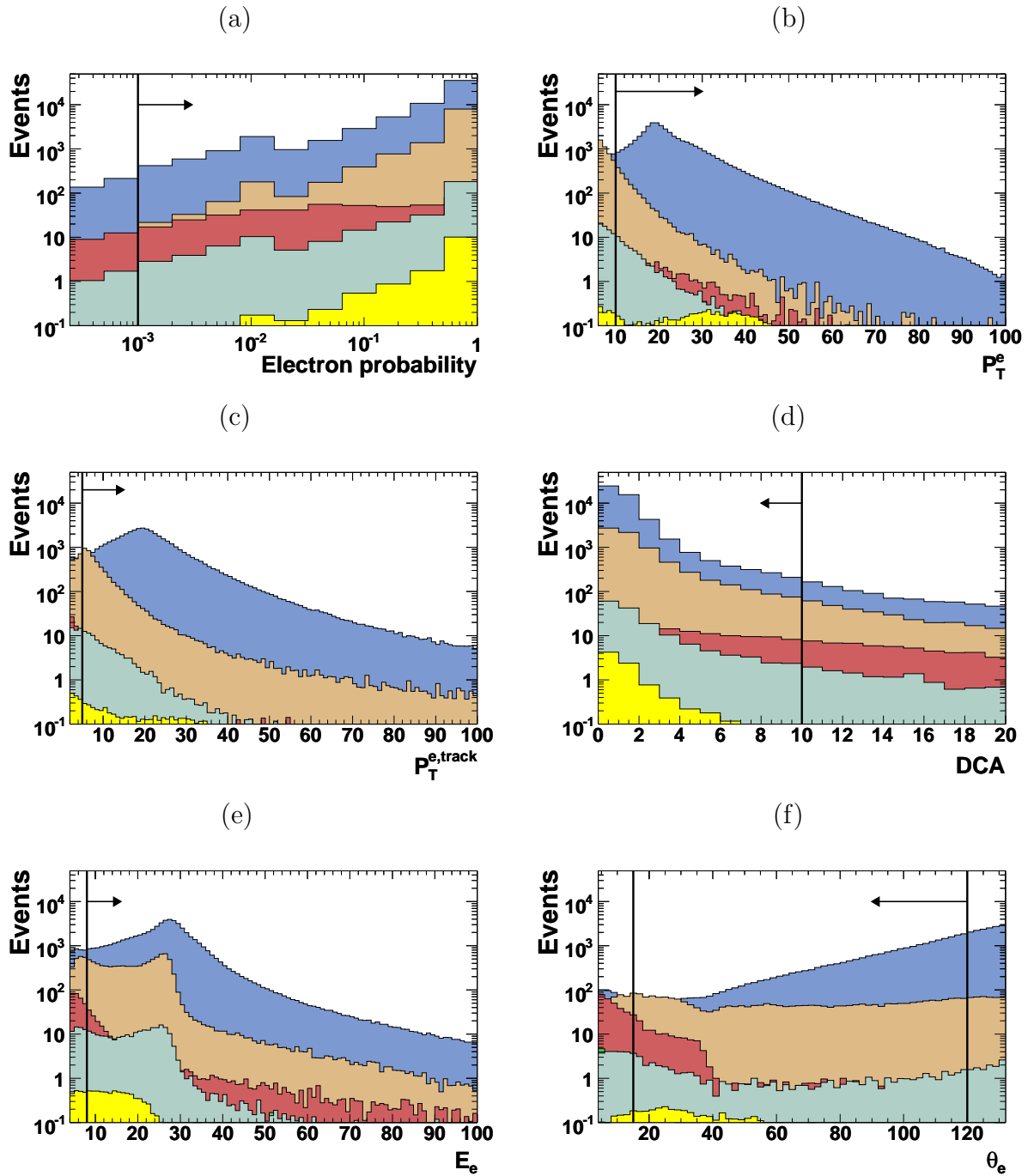


Figure 6.5: Distribution of MC events for various properties of the isolated electron. The W signal MC only comprises the electron decay channel of the W boson in these plots. The legend of Fig 6.1 applies.

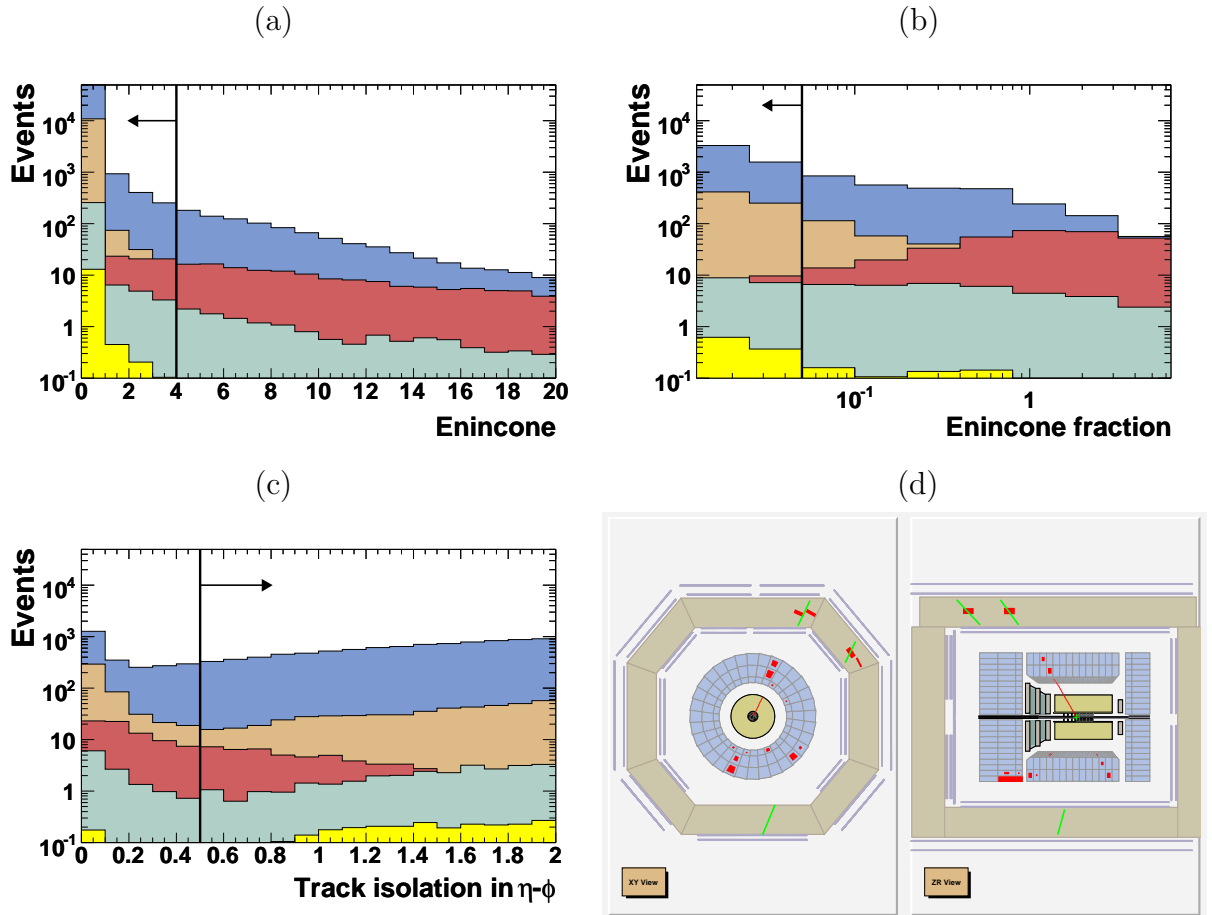


Figure 6.6: (a)–(c) Distribution of MC events for various properties of the isolated electron. The W signal MC only comprises the electron decay channel of the W boson in these plots. The legend of Fig 6.1 applies. (d) Cosmic muon event that passed the event selection and had to be rejected ‘by hand’.

- θ_l
The lepton polar angle, Fig. 6.5 f, was restricted to $15^\circ < \theta_l < 120^\circ$ to ensure that the two channels were measured over the same angular range.
- **Track isolation**
Misidentified hadrons close to jets were a significant source of fake leptons. To reject such events the lepton track had to be isolated from other primary vertex tracks with $P_T^{\text{trk}} > 0.2$ GeV and $15^\circ < \theta_{\text{trk}} < 164^\circ$, by at least 0.5 units in $\{\eta, \phi\}$ space, as shown in Fig. 6.6 c. In the electron channel, this condition was waived for electrons with $\theta_e < 45^\circ$ to maintain efficiency in the forward region.
- **CAL isolation**
The fake signal rate from jets was particularly problematic in the muon channel as the CAL energy of muons was small and hadronic deposits could easily be misidentified as MIPs. This was controlled by requiring that the muon was isolated by one unit in $\{\eta, \phi\}$ space from jets with $E_T^{\text{jet}} > 5$ GeV and $|\eta^{\text{jet}}| < 3$. In the electron channel,

electromagnetic clusters from background processes were rejected by demanding that the energy not associated with the electron (termed ‘Enincone’ in Fig. 6.6 a) in an $\{\eta, \phi\}$ cone of radius 0.8 did not exceed 4 GeV and additionally, that it was less than 5% of the electron’s energy, see Fig. 6.6 b).

- **Multi-isolated-muon veto**

It was extremely unlikely to find two genuine isolated leptons other than the scattered beam electron in an event. In the muon channel, events with two isolated leptons could arise if the scattered beam electron was identified as an additional isolated electron. However, the probability of finding a second genuine isolated muon was extremely rare. Therefore, events in the muon channel were removed if they contained, in addition to the isolated muon, one with probability $P_{MV}^{\mu} > 0.6$ and a matching track with $P_T^{\mu} > 1$ GeV. In HERA II the track of this additional muon had to pass the third superlayer before the event was discarded.

In the electron channel, an additional isolated electron could arise from the scattered beam electron, therefore, events with two isolated electrons were not vetoed. However, an additional isolated muon implied a misidentification or the case where an event belonging to the muon channel entered the selection because the scattered beam electron was misidentified as the isolated electron. Therefore, fake signals of this type in the electron channel were suppressed by rejecting events, in which an additional isolated muon was found. This was implemented by rejecting the event if there was an additional muon with $P_{MV}^{\mu} > 0.6$, which was isolated from jets by one unit in $\{\eta, \phi\}$ space and satisfied $P_T^{\mu} > 2$ GeV.

The data events passing these requirements were scrutinised by eye with the ZEUS Event Display, which revealed that one event was in fact due to cosmic muons traversing the detector, see Fig 6.6 d. The event was thus explicitly rejected from the event selection.

6.2 Results of the isolated lepton search

After applying the requirements, detailed above, 32 isolated electron and 8 isolated muon candidate events remained in the data. In the MC the corresponding number of events (normalised to the data luminosity) that passed the selection were 38 and 10, respectively. The data results were therefore considered slightly lower than expected but still in agreement with the MC prediction. The isolated muon sample was much smaller than set of isolated electrons due to the low efficiency of reconstructing muons, which relied on the identification of the minimum ionising particle’s small deposit in the calorimeter.

The selected MC events comprised about 6.8 (0.05) Charged Current, 4.8 (0.001) Neutral Current, 1.3 (2.0) lepton pair and 25.2 (7.5) single W boson production events in the isolated electron (muon) search. Hence, the dominant part of the MC expectation was formed by single W boson production in both channels. Charged and Neutral Current were the main backgrounds in the isolated electron search but negligible in the selection of isolated muons where lepton pair production, containing mostly muon-pairs, formed the only significant background.

Isolated e Candidates	$P_T^X < 12$ GeV	$12 < P_T^X < 25$ GeV	$P_T^X > 25$ GeV
ZEUS e^-p 208 pb $^{-1}$	9/10.6 \pm 1.2 (58%)	5/3.7 \pm 0.5 (58%)	3/3.7 \pm 0.5 (59%)
ZEUS e^+p 296 pb $^{-1}$	7/12.0 \pm 1.6 (73%)	5/4.1 \pm 0.6 (69%)	3/3.9 \pm 0.5 (78%)
ZEUS $e^\pm p$ 504 pb $^{-1}$	16/22.6 \pm 2.7 (66%)	10/7.8 \pm 1.0 (64%)	6/7.6 \pm 0.9 (69%)

Isolated μ Candidates	$12 < P_T^X < 25$ GeV	$P_T^X > 25$ GeV
ZEUS e^-p 208 pb $^{-1}$	1/1.7 \pm 0.3 (75%)	2/2.1 \pm 0.3 (86%)
ZEUS e^+p 296 pb $^{-1}$	2/2.3 \pm 0.4 (76%)	3/3.4 \pm 0.6 (81%)
ZEUS $e^\pm p$ 504 pb $^{-1}$	3/3.9 \pm 0.6 (76%)	5/5.5 \pm 0.8 (83%)

Table 6.2: Results of the search for isolated electrons (top) and for isolated muons (bottom). The observed number of data events is compared to the SM prediction (data/SM). The fraction of the SM expectation arising from single W boson production is given in parentheses. The errors comprise statistical and systematic uncertainties added in quadrature. Small discrepancies in the tables are due to rounding to a single decimal place.

The results of the isolated electron search are presented in Table 6.2 in three bins of P_T^X for the e^-p , e^+p and the combined $e^\pm p$ data sets. The summary of the isolated muon search, also in Table 6.2, only comprises two bins of P_T^X due to a trigger threshold near $P_T^X = 12$ GeV. The 15% uncertainty of the NLO prediction for single W boson production is included in the quoted errors.

The number of isolated electron candidates is lower than the MC prediction for e^+p data in the lowest bin of P_T^X , but is in good agreement with the MC in all other bins. In particular, at the highest P_T^X there is no indication of any excess of data above the MC expectation. The purity of single W boson production in the MC is significantly lower for e^-p data than for e^+p . This is due to the increased background from Charged Current events whose cross section in e^-p data is twice as large as in e^+p data.

Tables 6.3–6.4 detail the contribution of the different background MCs to the Standard Model expectation of the isolated lepton search in bins of P_T^X . Charged Current formed the dominant contribution in the electron search due to its large cross section and genuine P_T^{miss} . In the medium P_T^X bin, the NC background was dominant. This is the region where the scattered beam electron entered the angular acceptance of the electron search and could be identified as the isolated lepton if mis-measurement of the hadronic system lead to P_T^{miss} . The lepton pair background contributed little compared to CC and NC. Electron pair production was entirely eliminated by the event requirements since such events lacked genuine P_T^{miss} and electrons could be detected very efficiently in ZEUS. Muon pairs were more likely to contribute due to the small CAL deposits that were hard to detect and could lead to large missing transverse momentum. The contribution of tau pairs was larger than that of muons due to the genuine P_T^{miss} and the genuine isolated leptons created in the tau decay. However, its effect was lessened by the fact that its cross section was smaller than that of muon pair production and that only about 35% of taus decayed into electrons or muons, furthermore, a fraction of those daughter leptons did not pass the P_T threshold.

In the isolated muon search the Charged and Neutral Current backgrounds were negligible, as can be seen in Table 6.4. At first sight, this is surprising given that a particle from

Isolated electrons						
Background fractions in e^-p						
Bkgd.	$P_T^X < 12$ GeV		$12 < P_T^X < 25$ GeV		$P_T^X > 25$ GeV	
CC	2.8 ± 0.3	26 %	0.5 ± 0.1	14 %	1.1 ± 0.2	31 %
NC	1.4 ± 0.3	13 %	0.8 ± 0.1	22 %	0.3 ± 0.04	9 %
l^+l^-	0.4 ± 0.1	3 %	0.2 ± 0.1	6 %	0.04 ± 0.02	1 %
$\mu^+\mu^-$	0.1 ± 0.1	1 %	0.1 ± 0.1	4 %	0.004 ± 0.004	0 %
$\tau^+\tau^-$	0.2 ± 0.1	2 %	0.1 ± 0.04	2 %	0.03 ± 0.02	1 %
Background fractions in e^+p						
Bkgd.	$P_T^X < 12$ GeV		$12 < P_T^X < 25$ GeV		$P_T^X > 25$ GeV	
CC	1.7 ± 0.2	14 %	0.3 ± 0.1	7 %	0.3 ± 0.1	8 %
NC	1.0 ± 0.3	9 %	0.9 ± 0.1	21 %	0.4 ± 0.1	10 %
l^+l^-	0.5 ± 0.1	4 %	0.1 ± 0.03	2 %	0.2 ± 0.1	4 %
$\mu^+\mu^-$	0.1 ± 0.04	1 %	0.02 ± 0.01	1 %	0.1 ± 0.03	1 %
$\tau^+\tau^-$	0.4 ± 0.1	3 %	0.1 ± 0.03	1 %	0.1 ± 0.01	3 %
Background fractions in $e^\pm p$						
Bkgd.	$P_T^X < 12$ GeV		$12 < P_T^X < 25$ GeV		$P_T^X > 25$ GeV	
CC	4.5 ± 0.4	20 %	0.8 ± 0.2	11 %	1.5 ± 0.2	19 %
NC	2.4 ± 0.4	11 %	1.7 ± 0.2	22 %	0.7 ± 0.1	10 %
l^+l^-	0.8 ± 0.1	4 %	0.3 ± 0.1	4 %	0.2 ± 0.1	3 %
$\mu^+\mu^-$	0.2 ± 0.1	1 %	0.2 ± 0.1	2 %	0.1 ± 0.03	1 %
$\tau^+\tau^-$	0.6 ± 0.1	3 %	0.1 ± 0.1	2 %	0.1 ± 0.1	2 %

Table 6.3: Different background contributions with their statistical uncertainties to the search for isolated electrons in e^-p , e^+p and $e^\pm p$ data. The contributions are given for every bin of P_T^X in terms of number of events (first column) and as a percentage of the total SM expectation (second column). The lepton pair production is further split into muon and tau pairs (electron pairs did not contribute any events).

the hadronic system might naively be considered more likely to imitate the signature of a MIP than an electron. However, it can be explained by the stricter isolation requirements in the CAL that are imposed by the muon finder on MIP candidates. Muon pair production formed the dominant background in this search channel due to the genuine isolated muons in the event and the relatively high probability of ‘missing’ the second MIP deposit in the calorimeter. Tau pairs contributed little in comparison due to their smaller production cross section and the fact that the branching ratio to leptons is only 35%.

After applying the selection requirements the resultant data and MC distributions were compared for the quantities θ_e , ϕ_{acop} , P_T^l , P_T^X , P_T^{miss} , M_T . These are shown in Figs. 6.7–6.9 for the e^-p , e^+p and the combined $e^\pm p$ data sets of the isolated electron search. The equivalent distributions are shown in Fig. 6.10 for isolated muons but due to the reduced statistics only for the combined $e^\pm p$ data set. The distributions for the quantities P_T^μ and M_T had to be grouped into an overflow bin at high values in order to take into account the large errors associated with the CTD momentum measurement at high momenta, where the track curvature was small. Due to the dependence of M_T on the muon transverse momentum, large values of M_T above 120 GeV originated from these poorly measured P_T^μ in the overflow bin and where therefore also grouped into a single bin.

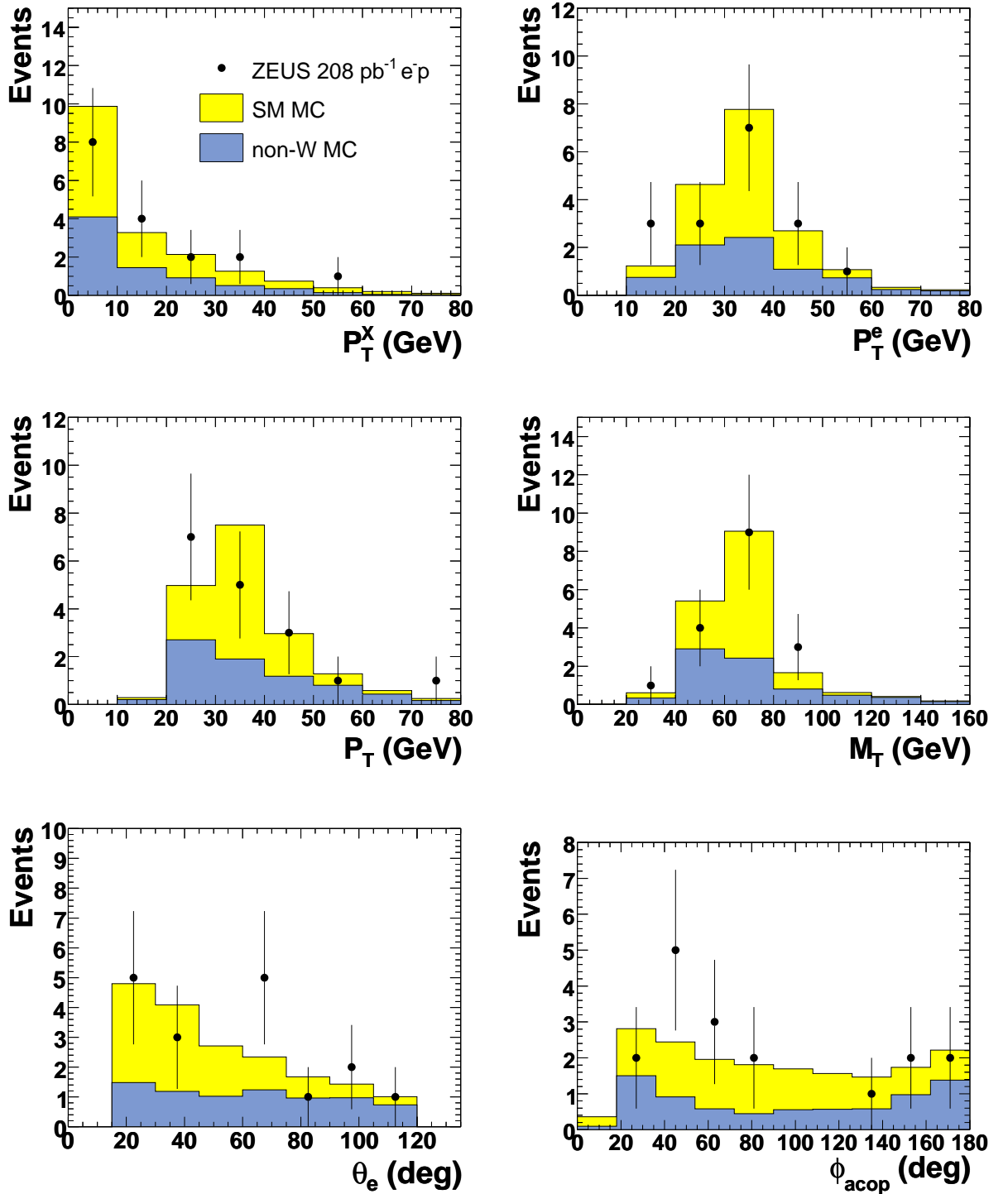


Figure 6.7: Comparison of the data distributions of isolated electrons (points) to the SM expectation for the e^-p collision samples. The light-shaded (yellow) histogram represents the **total** Standard Model MC prediction, the dark-shaded (blue) area the predicted contribution from events not arising from $ep \rightarrow lWX$. The background to the isolated lepton search is thus shown in dark (blue) and above this, the band of the SM MC histogram (yellow) arises from single W boson production. The error bars on the data points correspond to \sqrt{N} , where N is the number of events.

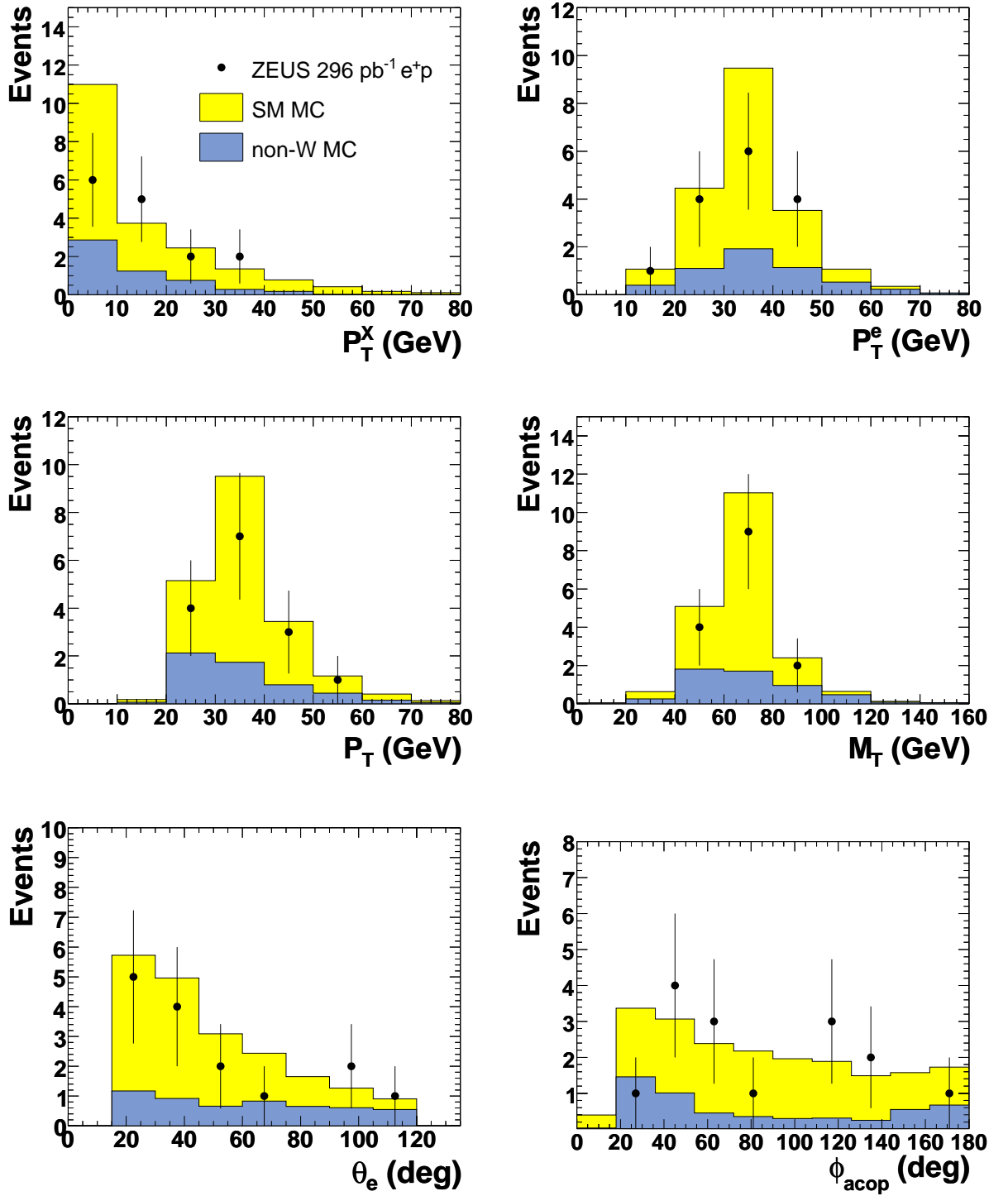


Figure 6.8: Comparison of the data distributions of isolated electrons (points) to the SM expectation for the e^+p collision samples. All other details as in Fig. 6.7.

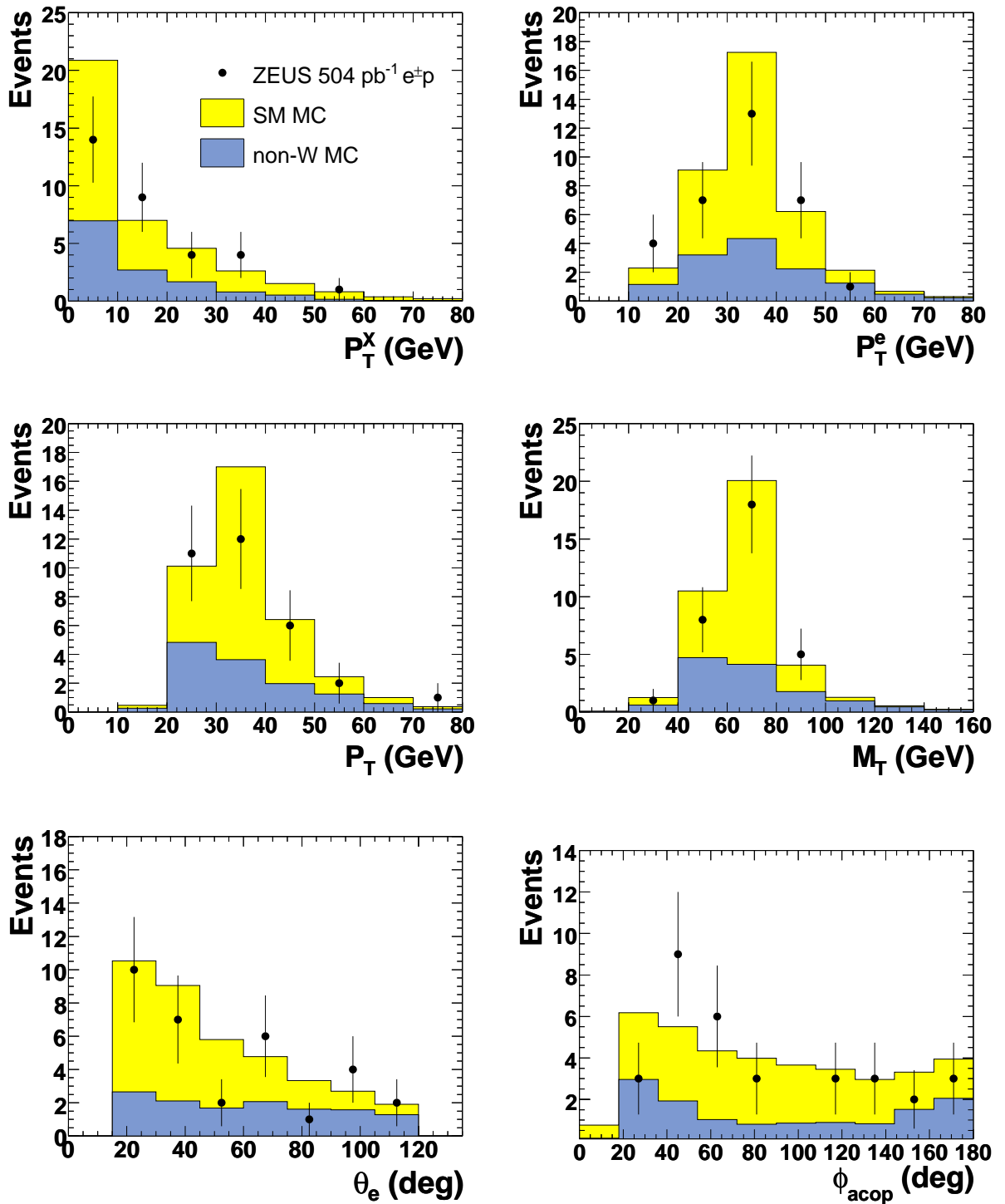


Figure 6.9: Comparison of the data distributions of isolated electrons (points) to the SM expectation for the $e^\pm p$ collision samples. All other details as in Fig. 6.7.

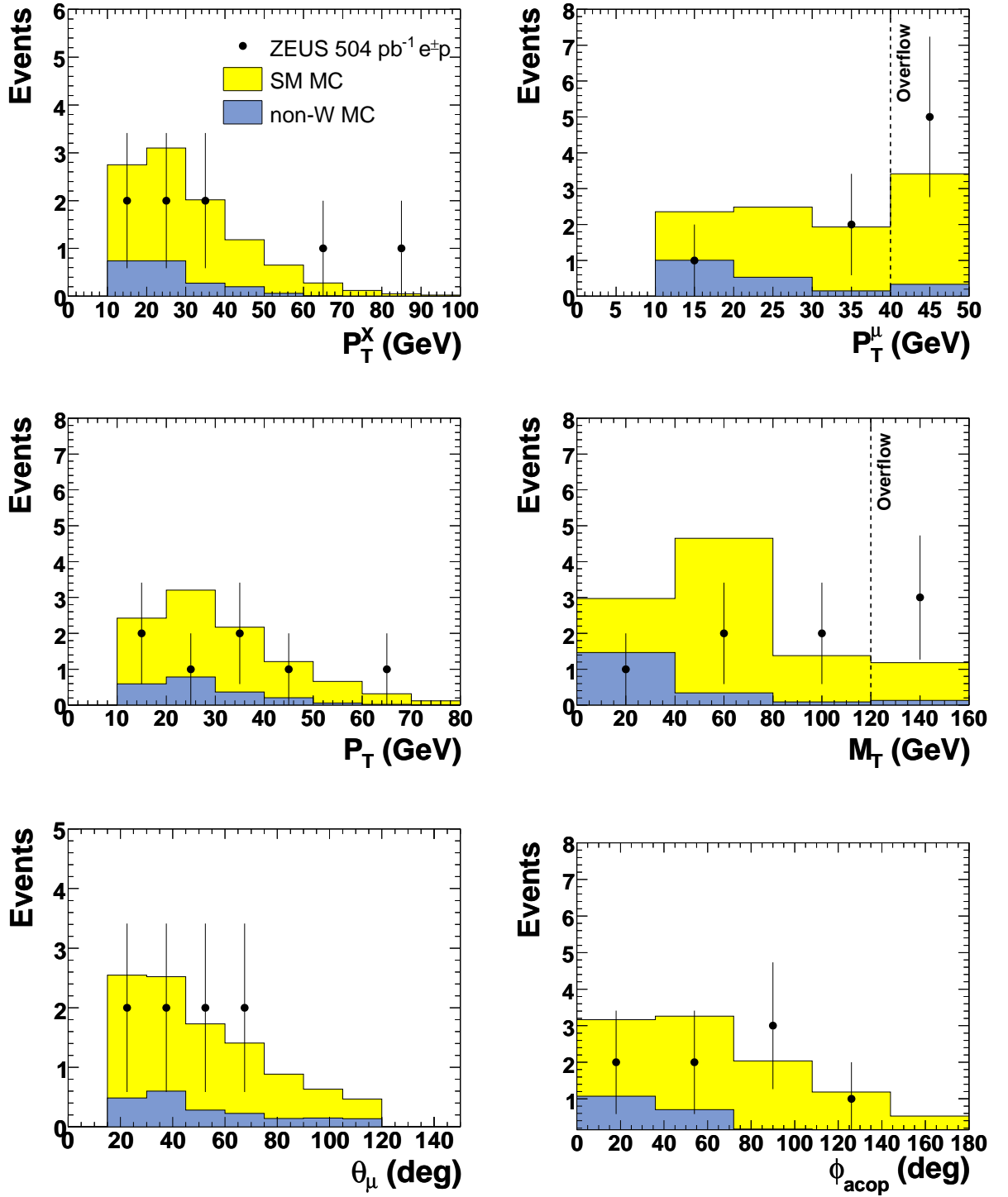


Figure 6.10: Comparison of the data distributions of isolated muons (points) to the SM expectation for the $e^\pm p$ collision samples. All other details as in Fig. 6.9.

Isolated muons				
Background fractions in e^-p				
Bkgd.	$12 < P_T^X < 25$ GeV		$P_T^X > 25$ GeV	
CC	0.005 ± 0.005	0 %	0.005 ± 0.005	0 %
NC	0.001 ± 0.001	0 %	no events	0 %
l^+l^-	0.4 ± 0.1	24 %	0.3 ± 0.1	13 %
$\mu^+\mu^-$	0.4 ± 0.1	21 %	0.2 ± 0.1	9 %
$\tau^+\tau^-$	0.1 ± 0.02	3 %	0.1 ± 0.04	4 %
Background fractions in e^+p				
Bkgd.	$12 < P_T^X < 25$ GeV		$P_T^X > 25$ GeV	
CC	0.02 ± 0.01	1 %	0.02 ± 0.02	1 %
NC	no events	0 %	no events	0 %
l^+l^-	0.5 ± 0.1	23 %	0.6 ± 0.1	18 %
$\mu^+\mu^-$	0.4 ± 0.1	20 %	0.5 ± 0.1	15 %
$\tau^+\tau^-$	0.1 ± 0.04	3 %	0.1 ± 0.1	3 %
Background fractions in $e^\pm p$				
Bkgd.	$12 < P_T^X < 25$ GeV		$P_T^X > 25$ GeV	
CC	0.02 ± 0.01	1 %	0.03 ± 0.02	0 %
NC	0.001 ± 0.001	0 %	no events	0 %
l^+l^-	1.0 ± 0.2	23 %	1.0 ± 0.2	16 %
$\mu^+\mu^-$	0.8 ± 0.2	20 %	0.7 ± 0.2	13 %
$\tau^+\tau^-$	0.1 ± 0.1	3%	0.2 ± 0.1	3 %

Table 6.4: Different background contributions with their statistical uncertainties to the search for isolated muons in e^-p , e^+p and $e^\pm p$ data. The contributions are given for every bin of P_T^X in terms of number of events (first column) and as a percentage of the total SM expectation (second column). The lepton pair production is further split into muon and tau pairs (electron pairs did not contribute any events).

The agreement of the data with the MC distribution is reasonable in all data sets and for both types of isolated lepton. In the electron channel, the M_T distribution peaks in both data and MC just below 80 GeV as expected for single W boson production, which contributes the majority of events in the MC. The electron data appear systematically low in e^+p data, but most bins still agree within statistical errors with the MC prediction.

For the isolated muon distributions, meaningful comments are difficult to make due to the limited statistics of the data sample. In the regions of low M_T the data appear lower than expected, but can still be attributed to statistical fluctuations, so that in general the agreement is acceptable.

There are two muon events in data that display very large hadronic transverse momenta, 82 GeV and 65 GeV. The corresponding isolated muon momenta are 37 GeV and > 40 GeV, respectively. Unfortunately, the latter muon momentum falls into the overflow bin and cannot be determined more precisely due to the large errors associated with the CTD momentum measurement in that region. So, overall its not possible to conclude from this data set if the region above 60 GeV is an indication of a true excess of isolated muons over the MC expectation or merely a mis-measurement or statistical fluctuation. However, the latter possibilities

seem likely when one considers that there are no events in the region $40 < P_T^X < 60$ GeV.

6.3 Cross section measurement

In the absence of an excess of data above the MC expectation in the isolated lepton search, the event selection formed a good basis for the measurement of the cross section for single W boson production, which accounted for 60–70% of the SM expectation in the electron channel and 75–85% in the muon channel. In order to suppress the NC background in the electron channel in the lowest bin of P_T^X , it was required that $\theta_e < 90^\circ$. This removed 3 (3) events in data compared to 2.3 (2.2) events in the MC prediction for e^-p (e^+p) collisions, see Table 6.5.

The cross section was measured in two slightly different regions of phase space for the electron and muon decay channels of the W boson, namely, the region of $15^\circ < \theta_e < 90^\circ$, $P_T^e > 10$ GeV and $P_T^{\text{miss}} > 12$ GeV for the $W \rightarrow e\nu_e$ channel and the region of $15^\circ < \theta_e < 120^\circ$, $P_T^\mu > 10$ GeV, $P_T^{\text{miss}} > 12$ GeV and $P_T^X > 12$ GeV for the $W \rightarrow \mu\nu_\mu$ channel.

The cross sections for the inclusive process $ep \rightarrow eWX$ and the separate electron and muon decay channels of the W boson were calculated using two different methods: a simple background subtraction method and a more refined scheme, in which the cross section was obtained from a likelihood distribution. They are described in the following sections.

The branching ratio $\mathcal{BR}_i = \mathcal{BR}(W \rightarrow l_i\nu)$, used in the cross section measurements, was assumed to be 10.8% per lepton [4]. The acceptance, A_i , was calculated separately for each channel using the single W MC samples. It was obtained from the ratio of the reconstructed to the generated number of signal events for a given channel, $A_i = N_{\text{rec}}^i/N_{\text{gen}}^i$, with the following caveat: The muon channel used the number of events generated in the region $P_T^X > 12$ GeV to measure the specific cross section of $W \rightarrow \mu\nu_\mu$ in that region (2nd row in Tables 6.6 and 6.7), but used the total number of generated events (i.e. $P_T^X > 0$ GeV) to measure the inclusive cross sections (3rd row onwards in Tables 6.6 and 6.7).

The small contribution of leptonically decaying taus from the W boson was taken into account as follows: Events were counted as reconstructed if they passed the full event selection, described in Section 6.1, for the lepton in question. Thus, the quantity N_{rec}^i contained a small admixture of $W \rightarrow \tau\nu_\tau$ events, whereas, events that entered N_{gen}^i were required to be purely $W \rightarrow e\nu_e$ or $W \rightarrow \mu\nu_\mu$, respectively. This increased the acceptance slightly and thus

Isolated e Candidates	$P_T^X < 12$ GeV	$12 < P_T^X < 25$ GeV	$P_T^X > 25$ GeV
ZEUS e^-p 208 pb $^{-1}$	8/9.1 \pm 1.1 (65%)	5/3.4 \pm 0.4 (58%)	1/3.2 \pm 0.4 (60%)
ZEUS e^+p 296 pb $^{-1}$	5/10.7 \pm 1.4 (78%)	5/3.7 \pm 0.5 (72%)	2/3.4 \pm 0.5 (77%)
ZEUS $e^\pm p$ 504 pb $^{-1}$	13/19.8 \pm 2.4 (72%)	10/7.0 \pm 0.9 (65%)	3/6.6 \pm 0.9 (69%)

Table 6.5: Results of the search for isolated electrons in the reduced phase space used in the cross section measurement. The observed number of data events is compared to the SM prediction (data/SM). The fraction of the SM expectation arising from single W production is given in parentheses. The errors comprise statistical and systematic uncertainties added in quadrature.

Process	$P_T^X > (\text{GeV})$	$\sqrt{s} (\text{GeV})$	Acc.	$\sigma_{\text{meas}}^{\text{BS}} (\text{pb})$	$\sigma_{\text{SM}} (\text{pb})$
$e^\pm p \rightarrow l W X,$ $W \rightarrow e \nu_e$	0	316	35 %	$0.090_{-0.029}^{+0.040}(\text{stat.}) \pm 0.007(\text{syst.})$	0.13
$e^\pm p \rightarrow l W X,$ $W \rightarrow \mu \nu_\mu$	12	316	28 %	$0.044_{-0.019}^{+0.035}(\text{stat.}) \pm 0.004(\text{syst.})$	0.05
$e^+ p \rightarrow l W X$	0	315	23 %	$0.80_{-0.28}^{+0.36}(\text{stat.}) \pm 0.07(\text{syst.})$	1.2
$e^- p \rightarrow l W X$	0	318	22 %	$1.08_{-0.43}^{+0.54}(\text{stat.}) \pm 0.10(\text{syst.})$	1.3
$e^\pm p \rightarrow l W X$	0	316	22 %	$0.92_{-0.24}^{+0.29}(\text{stat.}) \pm 0.08(\text{syst.})$	1.2

Table 6.6: Cross section results using method no.1, described in Section 6.3.1. The columns indicate the process and the beam types, the region of hadronic transverse momentum (P_T^X) of the measurement, the centre of mass energy (\sqrt{s}) of the beams, the acceptance (Acc.), the measured cross section from background subtraction ($\sigma_{\text{meas}}^{\text{BS}}$) with statistical and systematic uncertainties and the Standard Model expectation for the cross section (σ_{SM}). The value of σ_{SM} is given at the luminosity-weighted mean of \sqrt{s} for the data samples used and for a mean lepton beam polarisation of 0.

also reduced the measured cross section in proportion to the expected contribution from the tau decay channel of the W .

6.3.1 Cross sections from background subtraction

In this method, the cross section for the signal process was obtained by subtracting the expected background, N_{bkgd} , from the observed number of data events, N_{data} , and correcting the results for the branching ratio of the measured process, \mathcal{BR} , the detector acceptance, A , and the luminosity, \mathcal{L} , according to:

$$\sigma = \frac{N_{\text{data}} - N_{\text{bkgd}}}{\mathcal{BR} A \mathcal{L}} \quad (6.1)$$

For the measurement of the individual W decay channels $\mathcal{BR} = \mathcal{BR}_i$ was used, whereas, the inclusive cross sections that combined the electron and muon decay channels for the measurement used $\mathcal{BR} = 2\mathcal{BR}_i$. The results of this method are shown in Table 6.6 along with the Standard Model expectation for the cross sections. The statistical error on the data events was taken to be the classical frequentist central interval covering 68.3%, as a consequence, the statistical errors are asymmetric. The value of σ_{SM} for the combined e^+p and e^-p data sets is give for the luminosity-weighted mean of the e^+p and e^-p cross sections.

6.3.2 Cross sections from the likelihood method

In a different approach, the cross section was determined from the likelihood of observing n_i events in each search channel. This method estimated the number of signal events using a Poisson distribution and combined the two leptonic decay channels of the W as a product of their likelihoods:

$$L(\sigma) = \prod_i \frac{e^{-m_i} m_i^{n_i}}{n_i!} \quad (6.2)$$

Process	$P_T^X > (\text{GeV})$	$\sqrt{s} (\text{GeV})$	Acc.	$\sigma_{\text{meas}}^L (\text{pb})$	$\sigma_{\text{SM}} (\text{pb})$
$e^\pm p \rightarrow l W X,$ $W \rightarrow e \nu_e$	0	316	35 %	$0.090_{-0.025}^{+0.033}(\text{stat.}) \pm 0.008(\text{syst.})$	0.13
$e^\pm p \rightarrow l W X,$ $W \rightarrow \mu \nu_\mu$	12	316	28 %	$0.044_{-0.017}^{+0.024}(\text{stat.}) \pm 0.004(\text{syst.})$	0.05
$e^+ p \rightarrow l W X$	0	315	23 %	$0.80_{-0.26}^{+0.31}(\text{stat.}) \pm 0.06(\text{syst.})$	1.2
$e^- p \rightarrow l W X$	0	318	22 %	$1.09_{-0.39}^{+0.47}(\text{stat.}) \pm 0.10(\text{syst.})$	1.3
$e^\pm p \rightarrow l W X$	0	316	22 %	$0.93_{-0.23}^{+0.26}(\text{stat.}) \pm 0.08(\text{syst.})$	1.2

Table 6.7: Cross section results using method no.2, described in Section 6.3.2. All other details as in Table 6.6.

where i runs over the two leptonic decay channels of the W boson, n_i is the number of data events observed in a given channel and m_i stands for the expression:

$$m_i = N_{\text{bkgd}}^i + A_i \times \mathcal{BR}_i \times \mathcal{L} \times \sigma \quad (6.3)$$

The measured value of the cross section was that, which minimised $-\ln L(\sigma)$. The statistical errors were taken to be those that increased the negative log-likelihood distribution to $-\ln L(\sigma) + 0.5$. The results of this method are summarised in Table 6.7. The acceptances quoted for the total W cross sections are for the electron and muon decay channel combined, whereas the likelihood calculation used the individual values of 35% for the electron and 9% for the muon channel. The corresponding distributions of $-\ln L(\sigma)$ are shown in Figs. 6.11 and 6.12.

In principle, the likelihood method should be preferred to the formula described in Section 6.3.1 as it treats the electron and muon decay channel with the corresponding acceptance and backgrounds separately. This has the advantage that a large background in one channel does not dominate the measurement of the inclusive cross section. In this case, however, the two methods gave the same results ignoring negligible differences. So the outcome of Section 6.3.1 was used as a check that the likelihood method has been implemented correctly.

6.3.3 Cross sections from the likelihood method with Gaussian smearing

Finally, the second method was slightly refined to estimate the errors on the background expectation by introducing a Gaussian smearing around the expected number of background events with a resolution equal to the error on the background expectation. The likelihood function thus becomes:

$$L(\sigma) = \prod_i \left(\alpha_i \int_0^\infty G(x_i) \frac{e^{-x_i} x_i^{n_1}}{n_1!} dx \right) \quad (6.4)$$

where $G(x_i)$ is a standard Gaussian centred on m_i , as defined in Equation 6.3, with width δ_i and $\alpha_i = (\int_0^\infty G(x_i) dx)^{-1}$. However, this method proved to be a lot more CPU-intensive due to the additional integration that had to be performed, whilst giving the same results as the previous two methods. The simple likelihood method was thus given preference for the calculation of the systematic uncertainties.

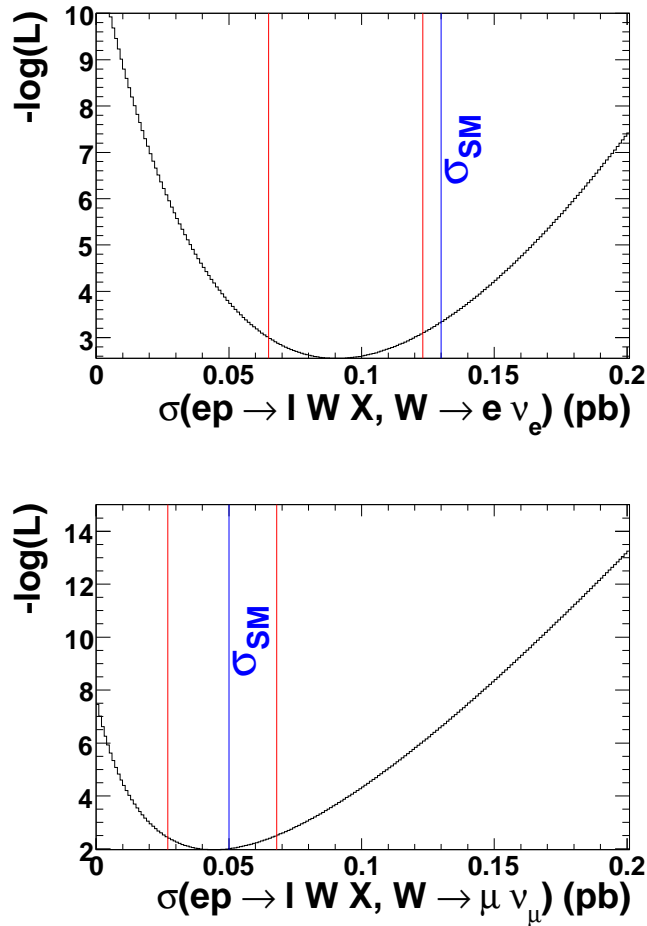


Figure 6.11: The negative of the log-likelihood distribution for the two exclusive processes of $ep \rightarrow l W X$ where $W \rightarrow e \nu_e$ (top) and $W \rightarrow \mu \nu_\mu$ (bottom). The minimum marks the measured cross section and the red lines indicate the statistical error bands and the blue line denotes the SM expectation.

6.4 Systematic uncertainties

The systematic uncertainties associated with the polarisation of the lepton beam were less than 5% (see Sections 3.1.6–3.1.5). Furthermore, the mean polarisation in the e^-p and e^+p data sets of the HERA II running phases was less than 4%. Therefore, the polarisation uncertainty was negligible for the isolated lepton search. For the cross section $\sigma(ep \rightarrow l W X)$ EPVEC predicted the effect of polarisation to be less than 1% and thus it was neglected in the cross section measurement as well.

The detailed results for the systematic uncertainties are shown in tables at the end of this chapter:

1. Tables 6.8–6.9 for the SM contribution to the search for isolated electrons,
2. Tables 6.10–6.11 for the search for isolated muon events,

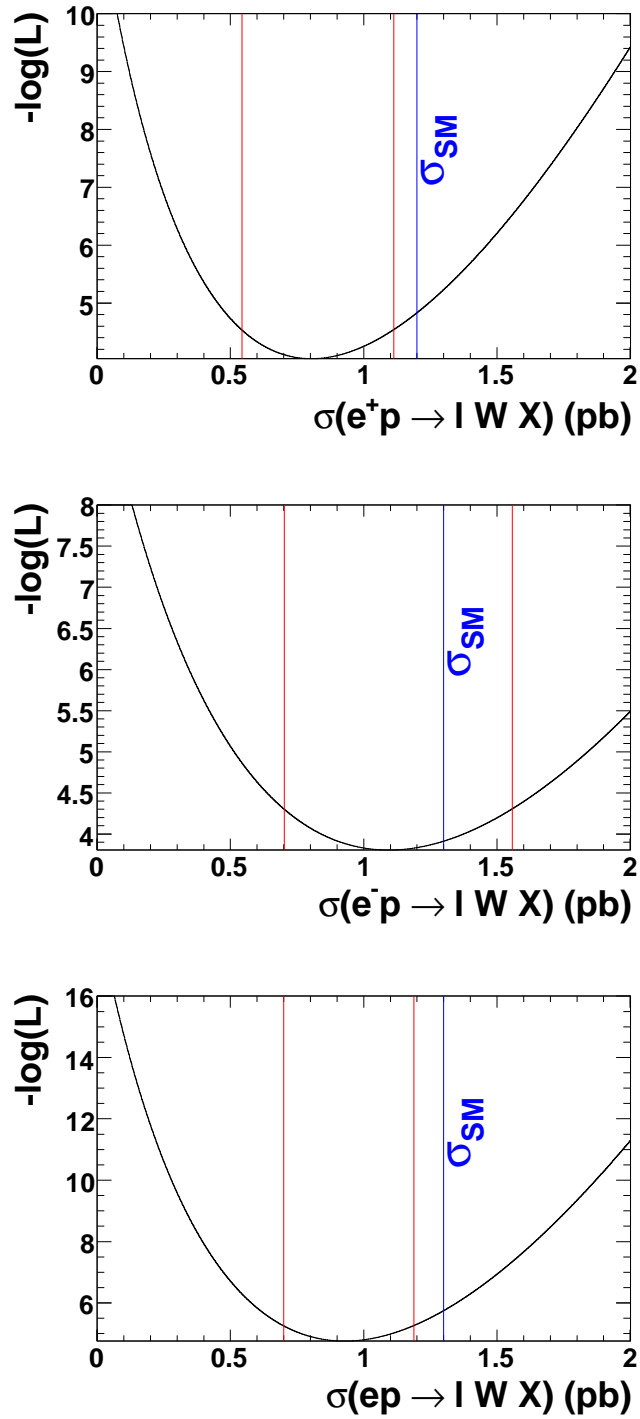


Figure 6.12: The negative of the log-likelihood distribution for the inclusive single W production cross section in e^+p (top), e^-p (middle) and $e^\pm p$ data (bottom). The minimum marks the measured cross section and the red lines indicate the statistical error bands and the blue line denotes the SM expectation.

3. Tables 6.12–6.13 for the sub-set of isolated electron events used in the electron-channel of the cross section measurements and
4. Tables 6.14–6.16 for cross section measurements.

The percentages shown in these tables are different from the values of the corresponding systematic uncertainties that are obtained in the following sections since the latter only affect a fraction of the total MC expectation in a given bin, e.g. a 15% uncertainty on the single W boson production (see Section 6.4.3) translates into a 9.9% uncertainty in the lowest P_T^X bin of the isolated electron search in $e^\pm p$ data in Table 6.9 since only 66% of the MC expectation in that bin comes from single W production (see Table 6.2).

6.4.1 Luminosity uncertainty

The luminosity measurement was mostly obtained by the PCAL, apart from cases where the PCAL was off, when the SPEC values were used. The two measurements are consistent within the respective uncertainties, however, the systematic uncertainty on the SPEC values is larger than the uncertainty on the PCAL values and therefore the former was taken as a conservative estimate of the total uncertainty on the luminosity measurement. The SPEC's luminosity uncertainty was 3.5%, as stated in Section 3.2.5. The luminosity value enters as a simple scaling factor of the MC contributions and therefore, the same value appears in Tables 6.8–6.10.

6.4.2 Energy scale

Previous studies established the relative uncertainty on the hadronic energy as measured by the ZEUS calorimeter to be 3% [131] and on the electron energy to be 2% [132]. Therefore, the effect of the systematic uncertainty on the calorimeter energy scale was assessed by varying the hadronic energy in the event by $\pm 3\%$ and the electromagnetic energy by $\pm 2\%$.

6.4.3 NLO uncertainty on single W boson production

The effect of the theoretical uncertainty of the NLO prediction for single W boson production was estimated by varying the MC contribution by 15%, which is the theoretical uncertainty on the cross section (see Section 2.7). For the systematic uncertainties on the isolated lepton search, this was implemented by varying the normalisation of the signal MC by $\pm 15\%$. In the case of the cross section measurement, the signal MC does not enter directly but is used to evaluate the acceptance, which is the ratio of the reconstructed to the generated events. In this ratio, a simple scale factor would cancel. So, the phase space was divided into $P_T^X > 12$ GeV, which is measured directly in both electron and muon channels, and $P_T^X < 12$, which is not measured in the muon channel but is obtained by extrapolation to give the total combined cross sections. To estimate the most extreme cases, the number of MC events (reconstructed and generated) at low P_T^X was scaled up whilst the number at high P_T^X was scaled down by 15% and vice versa.

6.4.4 Background uncertainties

In past analyses at ZEUS, uncertainties arising from the choice of hadronisation model were estimated by comparing results using a MC based on MEPS with one that relies on the CDM for the description of the QCD cascade (described in Section 4.3). This approach uses the different available models to obtain an uncertainty on the knowledge of parton showers that results in an uncertainty on the description of the final state. Its shortcoming is that it gives a measure of the agreement of different models rather than a direct measure of the uncertainty of the MC's description of nature.

To overcome this problem a data-driven method was used for the analyses presented here in order to replace the MEPS-CDM relative uncertainty. The objective of the new approach is to estimate the overall uncertainty on the dominant backgrounds that contribute to the event selections and thereby incorporate not just hadronisation model uncertainties, but others that are harder to estimate. It is based on the work undertaken during the lifetime of ZEUS to establish the validity of the MC's description in inclusive measurements, e.g. of Neutral and Charged Current as well as lepton pair production. The good performance of the MC in these cases was exploited to estimate its uncertainty in the specific region selected by the event requirements for isolated leptons and single W boson production, where e.g. NC and lepton pair events appear to carry large P_T^{miss} .

To obtain a more inclusive data sample, and hence one for which the MC description was considered reasonably trustworthy, some event requirements were lifted or modified to allow a certain type of background to pass. In these 'enriched' data sets the background under investigation dominated the MC estimate of the Standard Model contribution. The MC distribution in a given event variable was then fitted to the distribution of data events by varying a normalisation scale factor. The uncertainty on the MC background contribution was then taken as the sum of the resultant scale's deviation from unity and its uncertainty. The background contributions that were investigated with this method (and the final results for the uncertainty) are Neutral Current (15%), Charged Current (10%) and lepton pair production (20%), detailed in the following sections.

Neutral Current background

The electron channel of both the isolated lepton search and the cross section measurement were affected by a large number of Neutral Current events. These events contributed between 10–20% of the Standard Model expectation in the measured bins of P_T^X (see Table 6.3) and therefore an accurate estimate of the uncertainty on these types of events was important for the measurements. The following study was based on the HERA II $e^\pm p$ data set comprising 374 pb^{-1} .

Starting with the electron-channel event selection of the isolated lepton search, a Neutral Current enriched data set was obtained by removing all requirements that were specifically employed to reject NC events: the upper limit on the quantity δ , requirements on the ratio V_{ap}/V_p (standalone as well as combined with P_T^e) and the combined requirement on ξ^2 and P_T^{tot} . In order to enhance Neutral Current events relative to other backgrounds the lower limit on δ was tightened to $> 30 \text{ GeV}$, the criterion $P_T^X > 4 \text{ GeV}$ was added and the requirement on the acoplanarity angle was inverted to select events in which $\phi_{\text{acop}} < 20^\circ$.

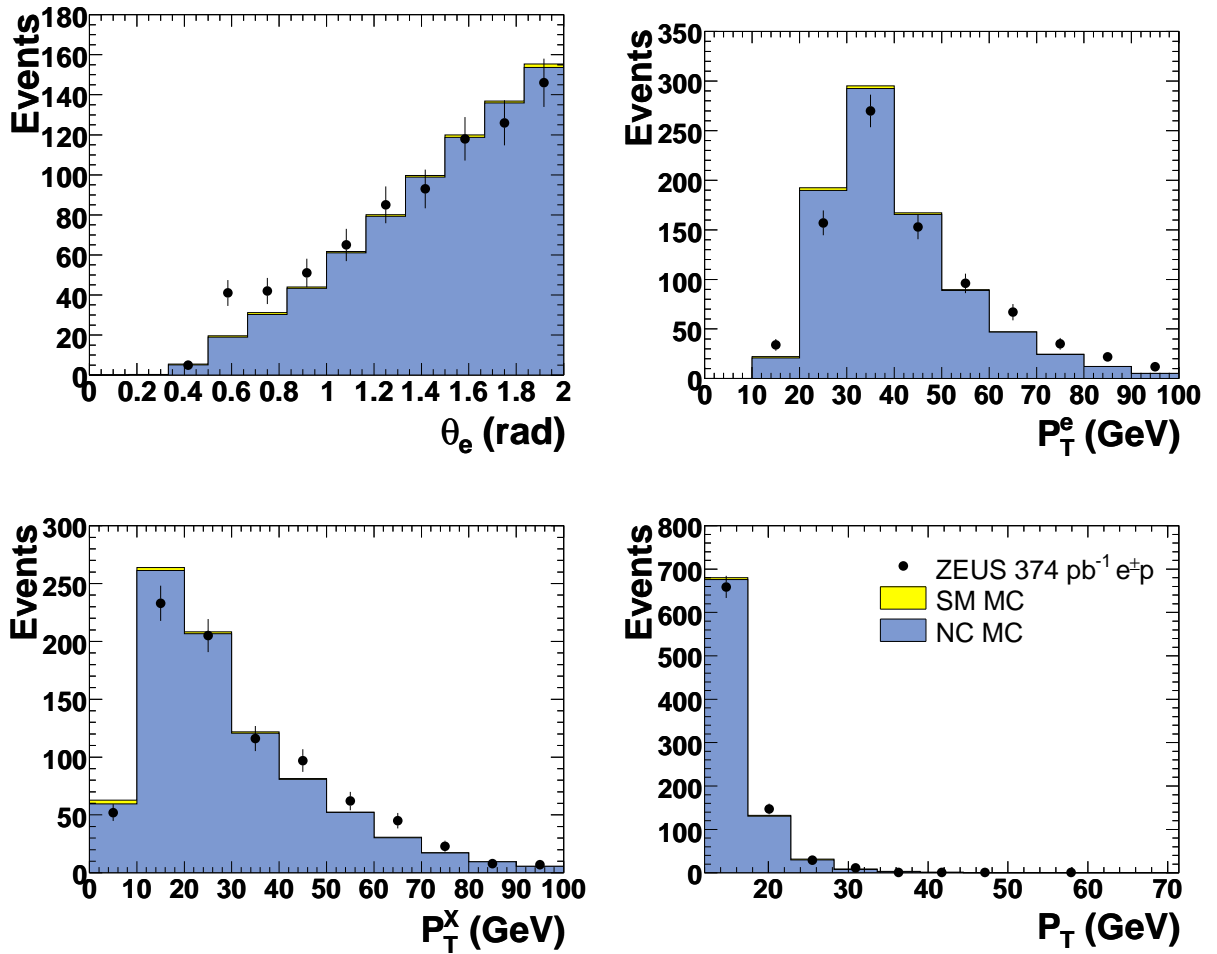


Figure 6.13: Neutral Current enriched data and MC samples: Distributions of the polar angle and transverse momentum of the electron, the hadronic transverse momentum and total missing transverse momentum in the event after the rescaling of the NC contribution.

This event selection resulted in 772 data events and 830 predicted (normalised) MC events, out of which 822 arose from Neutral Current. Hence, the Neutral Current enriched data sample was considered sufficiently pure. The Monte-Carlo distribution in θ_e was fitted to the data by performing a χ^2 fit with a scale factor for the normalisation of the Neutral Current background as a free parameter. The fit obtained this factor as 0.907 ± 0.033 with a $\chi^2/\text{NDF} \approx 17.44/9 = 1.94$. The uncertainty on the Neutral Current background was thus taken to be 15% to accommodate the shift in scale as well as the uncertainty on it.

Figure 6.13 shows the resultant distributions for the main kinematic variables with the NC contribution scaled by the factor obtained in the fit. The data and MC distributions are in reasonable agreement apart from a discrepancy in the region of $0.6 < \theta_e < 0.7$ rad, which corresponds to the gap between the FCAL and the BCAL. This discrepancy is likely to be due to an increased number of fake electrons in the data that occur when particles ‘scrape’ the BCAL, i.e. leave energy deposits on the forward face of the EMC in the BCAL, and then shower in the FCAL.

Charged Current background

In the isolated electron search 10–30% of the SM expectation was due to Charged Current events (see Table 6.3). To assess the uncertainty on this contribution, a background-enriched data sample was prepared and a χ^2 fit of the MC to the data distribution provided the estimate of the uncertainty. The procedure followed the example of the NC background, presented above.

Charged Current background events arose when a particle of the hadronic system mimicked the signature of an isolated electron. However, the hadronic system of CC events is identical in its properties to the hadronic system of NC events. This was exploited to accumulate a suitable test sample by selecting NC events, thereby profiting from the scattered beam electron in NC, which provided additional event information that could be used in the selection. The resultant set of events formed the base sample for this study.

From this, events were collected, which contained a second electron candidate, i.e. events, in which a particle of the hadronic system was a true electron or mimicked the electron signature. The basic isolation requirements used in the analysis were then applied to these second “electron candidates” and the events that passed were taken to be the background-enriched data sample to be used in the χ^2 fit. The resultant distributions of data and MC were compared and the uncertainty of the MC’s description was obtained from this fit.

Neutral Current events were selected using the requirements of the dedicated NC analysis at high Q^2 [22]. In addition to specialised constraints to reject non- ep background like beam-gas and cosmic muons, described in Section 6.1, the following criteria were applied:

- $|Z_{\text{vtx}}| < 30$ cm to further reduce beam-gas events.
- $P_T/\sqrt{E_T} < 4$ GeV^{1/2} rejects events with a large momentum imbalance, based on the fact that a perfectly measured NC event has $P_T = 0$ and that the resolution on the P_T measurement is approximately $\sqrt{E_T}$.
- $P_T/E_T < 0.7$ rejected the unphysical region where P_T is larger than E_T (allowed by the above criterion on $P_T/\sqrt{E_T}$).
- $y_{\text{JB}}(1 - x_{\text{DA}})^2 > 0.004$ discarded the region of very low y and high x where the MC is not valid due to missing higher order QED corrections [133]. The choice of the Jacquet-Blondel and Double Angle method for the kinematic variables reflects their suitability at low y and high x , respectively [131].
- $38 < \delta < 65$ GeV reduced photoproduction and other background events by exploiting the fact that in a perfectly measured NC event $\delta = 55$ GeV.
- $Q_{\text{DA}}^2 > 150$ GeV² restricted the events to high Q^2 , following the dedicated NC analysis.
- $y_{\text{el}} < 0.95$ reduced the photoproduction background. At low values of θ_e tracking was not available and a photon could be misidentified as an electron. In such cases the measured energy was usually low, so combined with a small value of θ_e this resulted in $y_{\text{el}} \approx 1$ (see Equation 5.26).
- $\eta_{\text{max}} > 2$ rejected a large fraction of the electron-pair and QED Compton backgrounds.

- QED Compton and electron pair rejection was performed by discarding events, in which two electron candidates (as found by EM without further requirements) were back-to-back within 10° and balanced in P_T such that $0.8 < P_T^{e1}/P_T^{e2} < 1.2$, and the event contained low hadronic energy satisfying $E_{\text{total}} - E_{e1} - E_{e2} < 3$ GeV.

The candidate assumed to be the scattered beam electron (i.e. the electron from which the quantities Q^2 , y etc. were calculated) had to satisfy:

- $P_{\text{EM}}^e > 0.001$, i.e. a sufficiently high electron candidate probability.
- $E_e > 8$ GeV to reject background from low energy pions that decay into photons, thereby ‘faking’ the electron signal in the EMC.
- Lepton track: The lepton candidate had to have a matching CTD track that originated from the primary vertex and approached its EMC energy deposit within 10 cm. Furthermore, the track had to pass the third CTD superlayer to be well reconstructed and carry $P_T^{\text{trk}} > 5$ GeV to avoid misidentification of other low energy charged particles.
- CAL isolation: The energy not associated with the electron in an $\{\eta, \phi\}$ cone of radius 0.8 had to be less than 4 GeV.

From this sample of NC events, those with more than one electron candidate were selected and the second electron candidate was required to satisfy the following criteria to be recognised as an electron:

- $P_{\text{EM}}^e > 0.001$, i.e. a sufficiently high electron candidate probability.
- $E_e > 8$ GeV
- $15^\circ < \theta_l < 120^\circ$, in order to select electrons in the same region as in the isolated lepton search.
- A matching CTD track that originated from the primary vertex and passed the third CTD superlayer.

Finally, the same isolation criteria were applied to the second candidate as in the isolated lepton search, namely:

- CAL isolation: The energy not associated with the electron in an $\{\eta, \phi\}$ cone of radius 0.8 had to be less than 4 GeV and less than 5% of the electron’s energy.
- Track isolation: The lepton track had to be isolated from other primary vertex tracks with $P_T^{\text{trk}} > 0.2$ GeV and $15^\circ < \theta_{\text{trk}} < 164^\circ$, by at least 0.5 units in $\{\eta, \phi\}$ space. This condition was waived for electrons with $\theta_e < 45^\circ$.

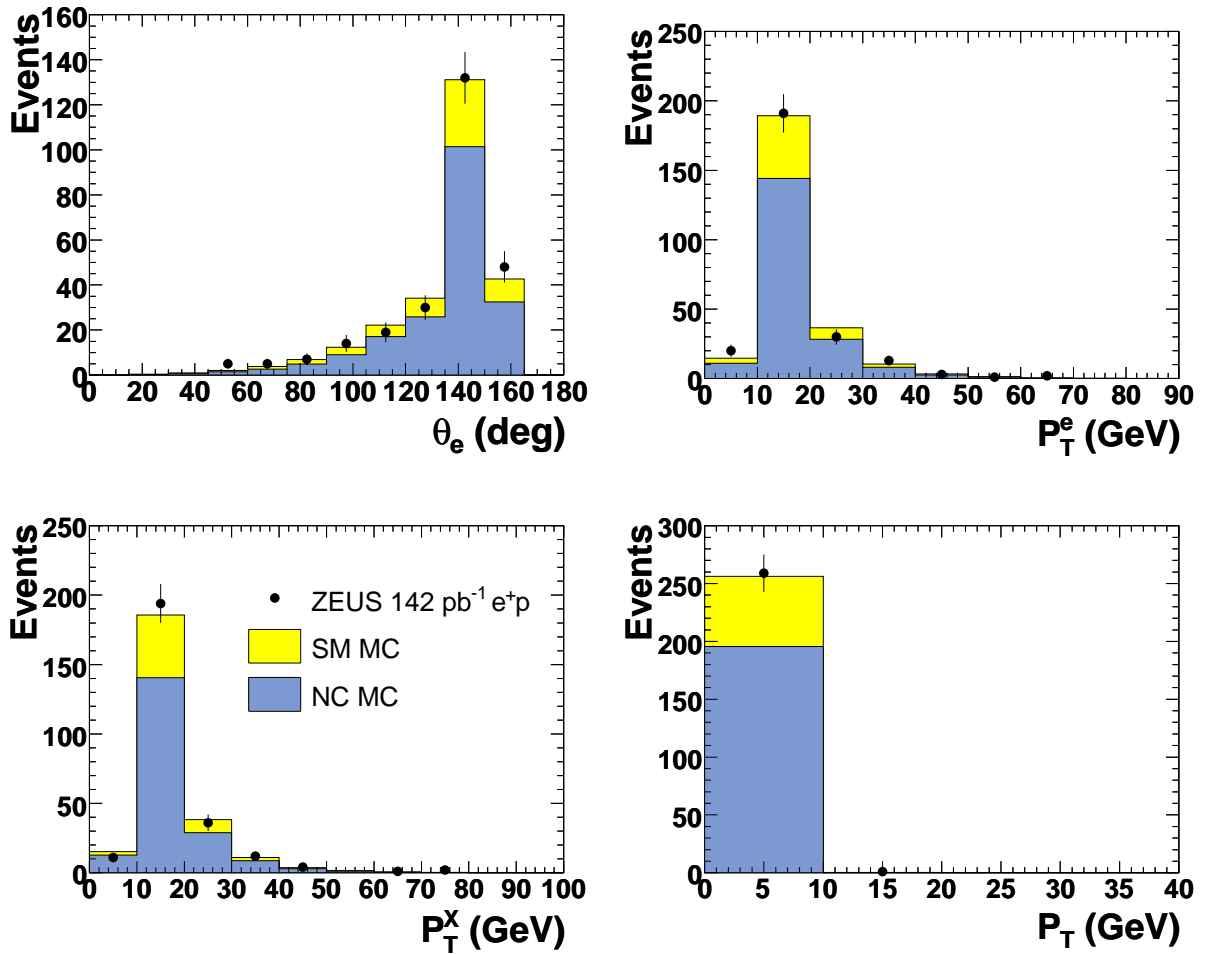


Figure 6.14: Neutral Current selection: Distributions of the polar angle and transverse momentum of the **DIS electron**, the hadronic transverse momentum and total missing transverse momentum in the event.

This event selection resulted in 260 data events and 257 predicted (normalised) MC events, out of which 196 arose from Neutral Current and 61 from QED Compton events. Figure 6.14 shows the resultant distributions from this event selection for the main kinematic variables of the scattered beam electron. The data and MC distributions are in good agreement.

In principle, it would be advantageous to reweight the NC events such that their Q^2 distribution is similar to the CC background that they have been selected to emulate in this study. However, there is a large admixture of QEDC in the sample, for which such a reweighting procedure would not be straightforward since these interactions have $Q^2 \approx 0$ but can be reconstructed with high Q^2 in the event (see Section 2.5). In the case of data, where it is not known which event is NC or QEDC and the reconstructed Q^2 can carry a large uncertainty, such a reweighting would introduce a significant systematic uncertainty into the study and hence was not applied here.

The Monte-Carlo distribution in θ_e of the second electron in the event was fitted to the data by performing a χ^2 fit with a scale factor for the normalisation of the Neutral

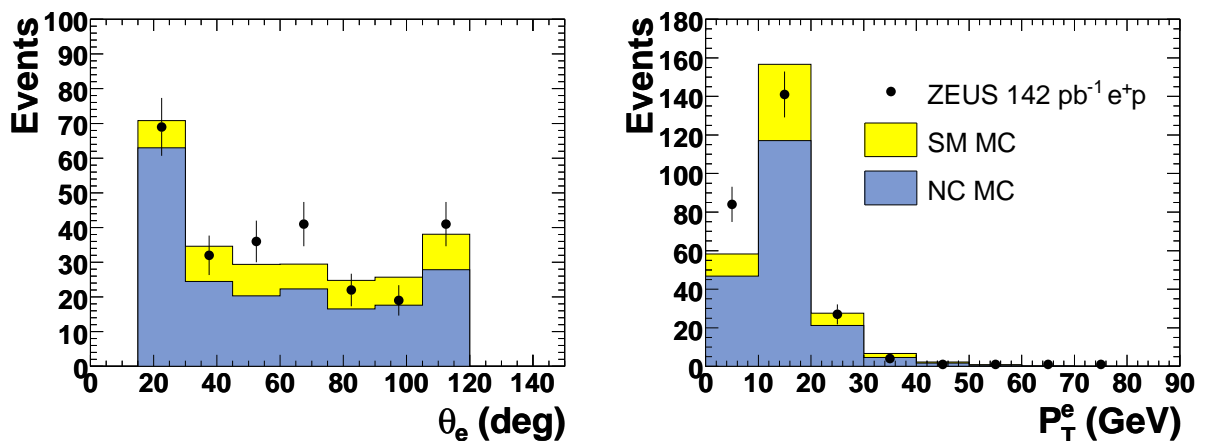


Figure 6.15: Neutral Current enriched data and MC samples: Distributions of the polar angle and transverse momentum of the **second (non-DIS) electron** after the rescaling of the NC contribution.

Current background as a free parameter. The fit obtained this factor as 0.982 ± 0.080 with a $\chi^2/\text{NDF} \approx 7.68/6 = 1.28$. The uncertainty on the Charged Current background was thus taken to be 10% to accommodate the shift in scale as well as the uncertainty on it. Figure 6.15 shows the resultant distributions in θ_e and P_T^e of the second electron in the event with the NC contribution scaled by the factor obtained in the fit.

Lepton pair production background

In the isolated muon search, lepton pair production contributed a significant background. In order to estimate the uncertainty on this background, a lepton pair enriched sample was selected from 374 pb^{-1} of $e^\pm p$ HERA II data. This selection was based on the criteria of the isolated muon search but lifted the requirements on P_T^X and the number of isolated muons found per event.

The lepton pair background was enhanced by inverting the requirement on the acoplanarity angle such that events with $\phi_{\text{acop}} < 20^\circ$ were selected and all events had to satisfy $V_{\text{ap}}/V_{\text{p}} < 0.2$. This selection resulted in 63 data events and 59 predicted (normalised) MC events, out of which 57 were due to lepton pair production. The main distributions for this enriched sample are shown in Fig. 6.16.

A χ^2 fit of the Monte-Carlo θ_μ distribution to the data obtained the scale factor for the normalisation of the lepton pair production background as 1.030 ± 0.134 with a $\chi^2/\text{NDF} \approx 2.16/5 = 0.43$. The uncertainty on the contribution of lepton pair production was then taken to be 20% to accommodate the shift in scale and its uncertainty, as well as make allowances for the reduced statistics of this enriched sample.

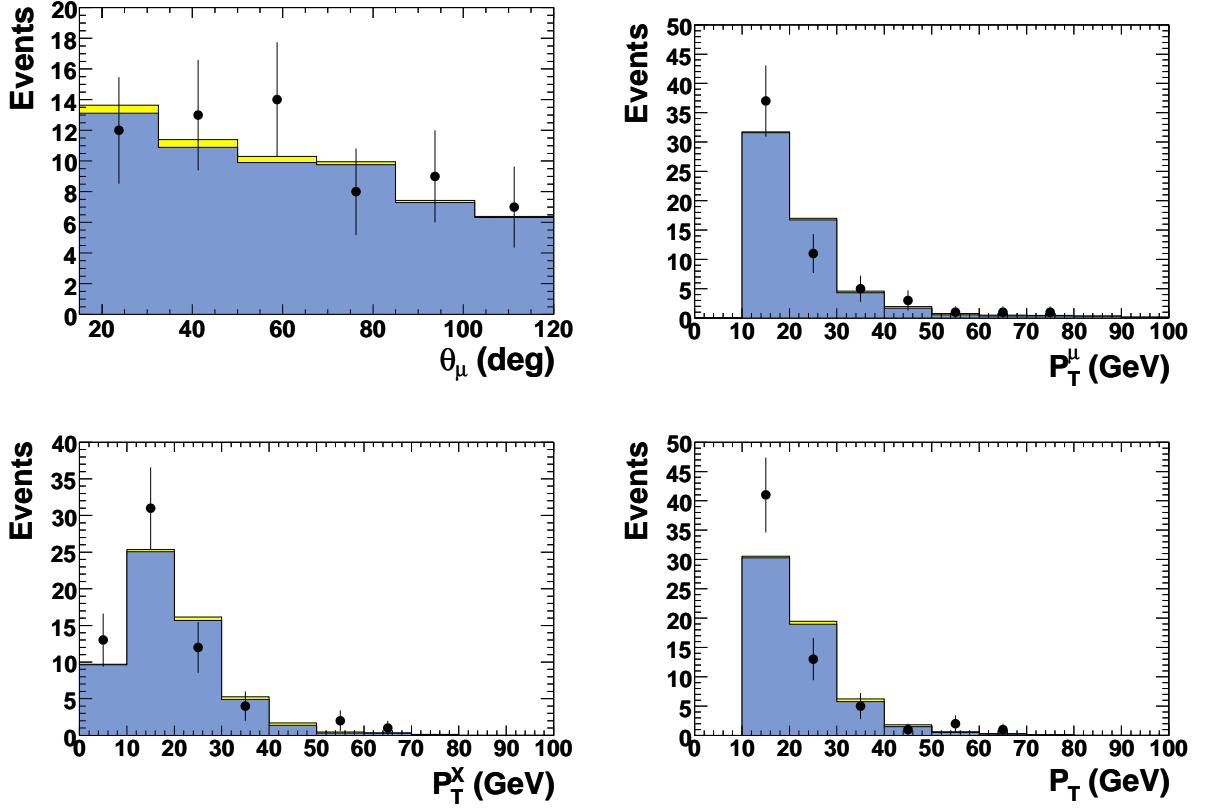


Figure 6.16: Distributions of the polar angle and transverse momentum of the muons, as well as the hadronic transverse momentum and total missing transverse momentum in the data and MC samples enriched with lepton pair production.

6.4.5 Muon finding efficiency

The measurement of the muon decay channel of the W relied on the assumption that the efficiency, with which muons were found was the same in data and MC. This was checked with a sample of muon pairs from electromagnetic interactions of the type depicted in Fig. 2.8. By selecting muon pairs from elastic processes a very clean sample could be obtained, which contained only two muons and no hadronic activity in the detector as the proton remained intact in these events. To measure the efficiency of the MV muon finder, the first muon was found with one of three other muon finders independent of MV. This defined the base set of events. The efficiency was then determined by the ratio of the number of events, in which MV found the second muon over the total number of events in the base set.

The data sample was obtained from a trigger chain that did not rely on a MIP at any level. The quality of the data set was ensured by requiring that there are only two tracks in the event and that both are long enough to be well reconstructed, i.e. stretching from the innermost CTD superlayer to at least the third. Additionally, the χ^2 per degree of freedom of the track had to be less than 10. Cosmic muons formed the main background in this study, but were removed by rejecting events, in which tracks were back-to-back within 15° in θ and ϕ and by requiring a tighter cut on the event vertex of $|Z_{vtx}| < 20$ cm.

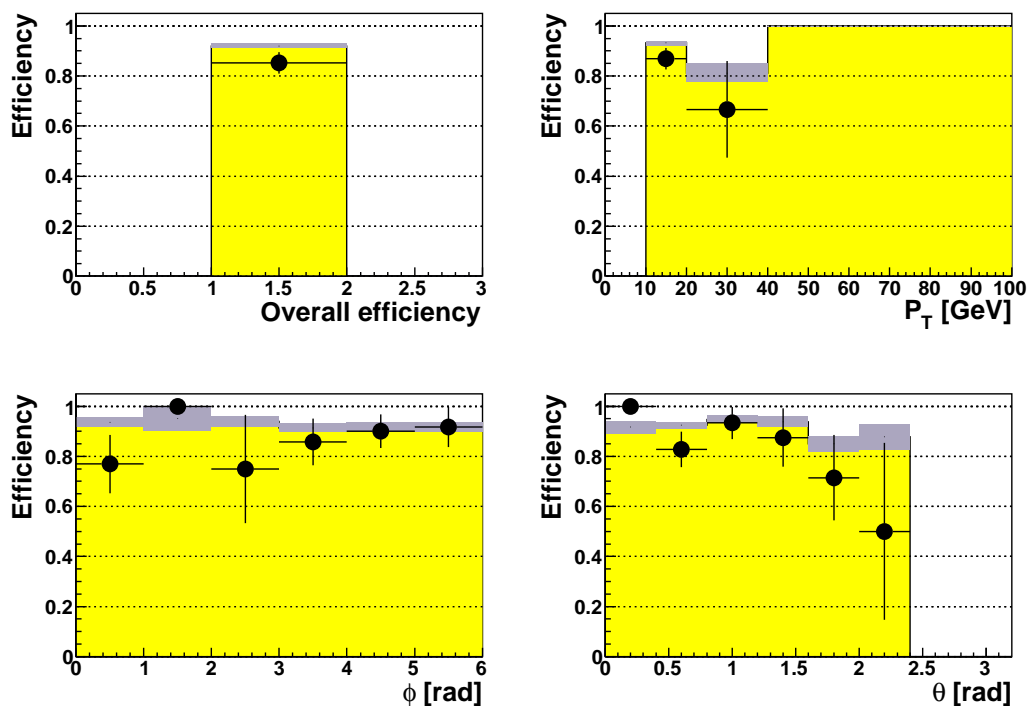


Figure 6.17: The efficiency of finding a muon with MV versus the azimuthal (ϕ) and polar angle (θ), as well as the transverse momentum of the muon (P_T). The top left plot is the efficiency overall. The points indicate the efficiency in data, whereas the yellow histograms with violet error bands indicate the efficiency in MC.

The first muon was found by one of the three finders GLOMU [134], MUBAC [135] or BREMAT [136]. The GLOMU finder used the muon chambers in the barrel and rear regions of the detector and identified muon candidates from a simple matching of CTD tracks to the muon chamber tracks. The same principle was used in the BREMAT finder, however, its algorithm was more sophisticated: It took full account of track-fit errors when matching the track segment in the muon chambers to the CTD track. Additionally, it also calculated the muon momentum from the track curvature due to the magnetic field in the iron yoke and used the result in the matching. The finder MUBAC looked for muon track segments in the backing calorimeter (BAC). It extrapolated central tracks from the event vertex to the BAC with a straight line approximation and required the distance of closest approach to the BAC track segments to be less than 50 cm.

The efficiency with which the second muon was found is shown in Fig. 6.17 in bins of the second muon's track ϕ , track θ , as well as its P_T in the region above 10 GeV, which is relevant for the measurement of single W production. At large P_T above 20 GeV there were only 5 data events in the base set, compared to 51 below 20 GeV, so the difference between data and MC in that bin could be attributed to a statistical fluctuation.

The overall efficiency of finding a muon with MV was obtained as 0.853 ± 0.043 in data and 0.920 ± 0.008 for the MC. This was taken into account by scaling down the MC expectation in the isolated muon search and in the muon channel of the cross section measurement by a value of $0.853/0.920 = 0.927$. The uncertainty of 0.046 on this scale factor was incorporated

Isolated e in e^-p	$P_T^X < 12$ GeV	$12 < P_T^X < 25$ GeV	$P_T^X > 25$ GeV
Result w. stat. error	10.64 ± 0.43	3.71 ± 0.20	3.69 ± 0.21
Luminosity	± 3.5 %	± 3.5 %	± 3.5 %
Hadronic energy +	-1.8 %	-1.4 %	$+3.5$ %
Hadronic energy -	$+3.1$ %	$+2.2$ %	-4.3 %
EM energy +	$+0.9$ %	$+5.5$ %	-0.1 %
EM energy -	-0.9 %	-1.1 %	-0.0 %
W NLO	± 8.6 %	± 8.7 %	± 8.9 %
NC background	± 2.0 %	± 3.3 %	± 1.4 %
CC background	± 2.6 %	± 1.4 %	± 3.1 %
lepton pair backgd.	± 0.7 %	± 1.2 %	± 0.2 %
Total systematic +	10.4 %	11.7 %	10.7 %
Total systematic -	10.1 %	10.3 %	11.0 %
Total uncertainty	1.19	0.48	0.46
Isolated e in e^+p	$P_T^X < 12$ GeV	$12 < P_T^X < 25$ GeV	$P_T^X > 25$ GeV
Result w. stat. error	11.96 ± 0.35	4.12 ± 0.17	3.93 ± 0.16
Luminosity	± 3.5 %	± 3.5 %	± 3.5 %
Hadronic energy +	-3.7 %	-0.6 %	$+2.4$ %
Hadronic energy -	$+1.7$ %	$+4.0$ %	-4.1 %
EM energy +	$+0.8$ %	$+3.2$ %	$+1.1$ %
EM energy -	-4.3 %	-1.3 %	$+1.2$ %
W NLO	± 10.9 %	± 10.4 %	± 11.6 %
NC background	± 1.3 %	± 3.2 %	± 1.5 %
CC background	± 1.4 %	± 0.7 %	± 0.8 %
lepton pair backgd.	± 0.8 %	± 0.4 %	± 0.9 %
Total systematic +	11.8 %	12.6 %	12.6 %
Total systematic -	12.9 %	11.5 %	12.9 %
Total uncertainty	1.58	0.55	0.53

Table 6.8: Systematic uncertainties on the SM contribution to the selection of isolated electrons in e^-p (top) and e^+p data (bottom). Individual uncertainties are explained in Sec. 6.4. The second row shows the results of Section 6.2 with statistical errors only. The bottom row of each table shows the total uncertainty, i.e. the statistical error and the larger total systematic uncertainty (plus or minus) added in quadrature, which is the error that is used in the tables of Section 6.2.

into the systematic uncertainties, listed as ‘MV efficiency’ in Tables 6.10–6.11.

Isolated e in $e^\pm p$	$P_T^X < 12$ GeV	$12 < P_T^X < 25$ GeV	$P_T^X > 25$ GeV
Result w. stat. error	22.64 ± 0.55	7.82 ± 0.26	7.61 ± 0.27
Luminosity	± 3.5 %	± 3.5 %	± 3.5 %
Hadronic energy +	-2.8 %	-1.0 %	$+2.9$ %
Hadronic energy -	$+2.4$ %	$+3.1$ %	-4.2 %
EM energy +	$+0.8$ %	$+4.3$ %	$+0.5$ %
EM energy -	-2.7 %	-1.2 %	$+0.6$ %
W NLO	± 9.9 %	± 9.6 %	± 10.3 %
NC background	± 1.6 %	± 3.2 %	± 1.4 %
CC background	± 2.0 %	± 1.1 %	± 1.9 %
lepton pair backgd.	± 0.7 %	± 0.8 %	± 0.5 %
Total systematic +	11.1 %	12.0 %	11.5 %
Total systematic -	11.5 %	10.9 %	11.9 %
Total uncertainty	2.66	0.97	0.94

Table 6.9: Systematic uncertainties on the SM contribution to the selection of isolated electrons in $e^\pm p$ data. All other details as stated in the caption of Table 6.8.

Isolated μ in e^-p	$12 < P_T^X < 25$ GeV	$P_T^X > 25$ GeV
Result w. stat. error	1.67 ± 0.11	2.12 ± 0.09
Luminosity	± 3.5 %	± 3.5 %
Hadronic energy +	-0.2 %	$+2.3$ %
Hadronic energy -	$+0.9$ %	-2.3 %
EM energy +	$+0.2$ %	-0.4 %
EM energy -	$+0.2$ %	-0.0 %
W NLO	± 11.3 %	± 12.9 %
NC background	± 0.0 %	± 0.0 %
CC background	± 0.0 %	± 0.0 %
lepton pair backgd.	± 4.9 %	± 2.7 %
MV efficiency	± 4.6 %	± 4.6 %
Total systematic +	13.6 %	14.6 %
Total systematic -	13.6 %	14.6 %
Total uncertainty	0.25	0.32
Isolated μ in e^+p	$12 < P_T^X < 25$ GeV	$P_T^X > 25$ GeV
Result w. stat. error	2.27 ± 0.14	3.39 ± 0.16
Luminosity	± 3.5 %	± 3.5 %
Hadronic energy +	-2.6 %	$+4.5$ %
Hadronic energy -	$+3.2$ %	-6.6 %
EM energy +	$+0.3$ %	$+0.1$ %
EM energy -	$+0.2$ %	$+0.2$ %
W NLO	± 11.4 %	± 12.2 %
NC background	± 0.0 %	± 0.0 %
CC background	± 0.1 %	± 0.1 %
lepton pair backgd.	± 4.6 %	± 3.6 %
MV efficiency	± 4.6 %	± 4.6 %
Total systematic +	14.0 %	14.7 %
Total systematic -	13.8 %	15.5 %
Total uncertainty	0.35	0.55

Table 6.10: Systematic uncertainties on the SM contribution to the selection of isolated muons in e^-p (top) and e^+p data (bottom). All other details as stated in the caption of Table 6.8.

Isolated μ in $e^\pm p$	$12 < P_T^X < 25$ GeV	$P_T^X > 25$ GeV
Result w. stat. error	3.94 ± 0.18	5.51 ± 0.18
Luminosity	± 3.5 %	± 3.5 %
Hadronic energy +	-1.6 %	$+3.6$ %
Hadronic energy -	$+2.2$ %	-4.9 %
EM energy +	$+0.2$ %	-0.1 %
EM energy -	$+0.2$ %	$+0.1$ %
W NLO	± 11.4 %	± 12.4 %
NC background	± 0.0 %	± 0.0 %
CC background	± 0.1 %	± 0.0 %
lepton pair backgd.	± 4.7 %	± 3.2 %
MV efficiency	4.6 %	4.6 %
Total systematic +	13.8 %	14.5 %
Total systematic -	13.7 %	14.9 %
Total uncertainty	0.57	0.84

Table 6.11: Systematic uncertainties on the SM contribution to the selection of isolated muons in $e^\pm p$ data. All other details as stated in the caption of Table 6.8.

$W \rightarrow e\nu$ in e^-p	$P_T^X < 12$ GeV	$12 < P_T^X < 25$ GeV	$P_T^X > 25$ GeV
Result w. stat. error	9.08 ± 0.32	3.35 ± 0.19	3.18 ± 0.19
Luminosity	± 3.5 %	± 3.5 %	± 3.5 %
Hadronic energy +	-1.7 %	-1.3 %	$+2.9$ %
Hadronic energy -	$+2.3$ %	$+3.9$ %	-5.2 %
EM energy +	$+0.4$ %	$+2.9$ %	-0.6 %
EM energy -	-1.7 %	-0.9 %	-0.8 %
W NLO	± 9.7 %	± 8.7 %	± 9.0 %
NC background	± 1.0 %	± 3.1 %	± 1.6 %
CC background	± 2.7 %	± 1.6 %	± 2.8 %
lepton pair backgd.	± 0.4 %	± 1.2 %	± 0.2 %
Total systematic +	11.0 %	11.2 %	10.6 %
Total systematic -	11.0 %	10.2 %	11.5 %
Total uncertainty	1.05	0.42	0.41
$W \rightarrow e\nu$ in e^+p	$P_T^X < 12$ GeV	$12 < P_T^X < 25$ GeV	$P_T^X > 25$ GeV
Result w. stat. error	10.72 ± 0.27	3.68 ± 0.15	3.35 ± 0.16
Luminosity	± 3.5 %	± 3.5 %	± 3.5 %
Hadronic energy +	-2.3 %	-2.5 %	$+1.4$ %
Hadronic energy -	$+1.8$ %	$+4.2$ %	-5.2 %
EM energy +	$+0.7$ %	$+1.3$ %	$+0.2$ %
EM energy -	-1.9 %	-0.6 %	$+0.9$ %
W NLO	± 11.6 %	± 10.8 %	± 11.6 %
NC background	± 0.7 %	± 3.0 %	± 1.6 %
CC background	± 1.5 %	± 0.7 %	± 0.7 %
lepton pair backgd.	± 0.5 %	± 0.2 %	± 0.9 %
Total systematic +	12.4 %	12.6 %	12.4 %
Total systematic -	12.6 %	12.0 %	13.3 %
Total uncertainty	1.38	0.49	0.47

Table 6.12: Systematic uncertainties on the SM contribution to the electron-channel of the cross section measurement in e^-p (top) and e^+p data (bottom). All other details as stated in the caption of Table 6.8.

$W \rightarrow e\nu$ in $e^\pm p$	$P_T^X < 12$ GeV	$12 < P_T^X < 25$ GeV	$P_T^X > 25$ GeV
Result w. stat. error	19.80 ± 0.42	7.03 ± 0.24	6.63 ± 0.24
Luminosity	± 3.5 %	± 3.5 %	± 3.5 %
Hadronic energy +	-2.1 %	-1.9 %	$+2.1$ %
Hadronic energy -	$+2.0$ %	$+4.1$ %	-5.2 %
EM energy +	$+0.6$ %	$+2.1$ %	-0.2 %
EM energy -	-1.8 %	$+0.8$ %	$+0.1$ %
W NLO	± 10.8 %	± 9.8 %	± 10.3 %
NC background	± 0.8 %	± 3.0 %	± 1.6 %
CC background	± 2.0 %	± 1.1 %	± 1.7 %
lepton pair backgd.	± 0.5 %	± 0.7 %	± 0.6 %
Total systematic +	11.8 %	11.9 %	11.3 %
Total systematic -	11.9 %	11.1 %	12.3 %
Total uncertainty	2.39	0.87	0.85

Table 6.13: Systematic uncertainties on the SM contribution to the electron-channel of the cross section measurement in $e^\pm p$ data. All other details as stated in the caption of Table 6.8.

$e^\pm p \rightarrow W$	$\sigma^{\text{BS}}(W \rightarrow e\nu_e)$	$\sigma^{\text{BS}}(W \rightarrow \mu\nu_\mu)$
Result	0.090 pb	0.044 pb
Luminosity	± 5.9 %	± 4.7 %
Hadronic energy +	$+2.1$ %	-3.3 %
Hadronic energy -	-1.5 %	-1.8 %
EM energy +	-2.4 %	-0.2 %
EM energy -	$+2.3$ %	-2.4 %
W NLO	± 0.4 %	0.0 %
NC background	± 3.0 %	0.0 %
CC background	± 3.8 %	± 0.1 %
lepton pair backgd.	± 1.1 %	± 6.0 %
MV efficiency	-	± 1.4 %
Total systematic +	8.3 %	7.7 %
Total systematic -	8.2 %	8.9 %
Total uncertainty	0.007	0.004

Table 6.14: Systematic uncertainties on the cross section measurements using method no.1 for the exclusive processes, in which the W decays to $e\nu_e$ (middle column) and $\mu\nu_\mu$ (right column). All other details as stated in the caption of Table 6.8.

$e^\pm p \rightarrow W$	$\sigma^L(W \rightarrow e\nu_e)$	$\sigma^L(W \rightarrow \mu\nu_\mu)$
Result	0.090 pb	0.044 pb
Luminosity +	-5.5 %	-4.5 %
Luminosity -	+6.7 %	+4.5 %
Hadronic energy +	+2.2 %	-4.5 %
Hadronic energy -	-1.1 %	-2.3 %
EM energy +	-2.2 %	0.0 %
EM energy -	+2.2 %	-2.3 %
W NLO	± 1.1 %	0.0 %
NC background +	-2.2 %	0.0 %
NC background -	+3.3 %	0.0 %
CC background +	-3.3 %	0.0 %
CC background -	+4.4 %	0.0 %
lepton pair backgd. +	-1.1 %	-6.8 %
lepton pair backgd. -	+1.1 %	+4.5 %
MV efficiency +	-	-2.3 %
MV efficiency -	-	0.0 %
Total systematic +	9.3 %	6.4 %
Total systematic -	7.4 %	10.1 %
Total uncertainty	0.008	0.004

Table 6.15: Systematic uncertainties on the cross section measurements using method no.2 for the exclusive processes, in which the W decays to $e\nu_e$ (middle column) and $\mu\nu_\mu$ (right column). All other details as stated in the caption of Table 6.8.

W production	$\sigma^{\text{BS}}(e^+ p \rightarrow W)$	$\sigma^{\text{BS}}(e^- p \rightarrow W)$	$\sigma^{\text{BS}}(e^\pm p \rightarrow W)$
Result	0.80 pb	1.08 pb	0.92 pb
Luminosity	± 5.3 %	± 5.9 %	± 5.6 %
Hadronic energy +	+1.2 %	+0.2 %	+0.7 %
Hadronic energy -	-1.5 %	-1.8 %	-1.6 %
EM energy +	-1.7 %	-1.7 %	-1.8 %
EM energy -	+0.6 %	+1.4 %	+1.0 %
W NLO	± 4.3 %	± 3.6 %	± 3.9 %
NC background	± 2.1 %	± 2.3 %	± 2.2 %
CC background	± 1.9 %	± 3.7 %	± 2.7 %
lepton pair backgd.	± 2.8 %	± 2.2 %	± 2.5 %
MV efficiency	± 0.5 %	± 0.3 %	± 0.4 %
Total systematic +	8.0 %	8.6 %	8.2 %
Total systematic -	8.2 %	8.8 %	8.4 %
Total uncertainty	0.07	0.10	0.08
W production	$\sigma^{\text{L}}(e^+ p \rightarrow W)$	$\sigma^{\text{L}}(e^- p \rightarrow W)$	$\sigma^{\text{L}}(e^\pm p \rightarrow W)$
Result	0.80 pb	1.09 pb	0.93 pb
Luminosity	± 5.2 %	± 5.9 %	± 5.6 %
Hadronic energy +	+1.2 %	+0.2 %	+0.8 %
Hadronic energy -	-1.5 %	-1.8 %	-1.6 %
EM energy +	-1.7 %	-1.7 %	-1.7 %
EM energy -	+0.6 %	+1.5 %	+1.0 %
W NLO	± 4.1 %	± 4.0 %	± 4.0 %
NC background	± 2.1 %	± 2.4 %	± 2.2 %
CC background	± 1.9 %	± 3.7 %	± 2.7 %
lepton pair backgd.	± 2.7 %	± 2.2 %	± 2.5 %
MV efficiency	± 0.5 %	± 0.4 %	± 0.4 %
Total systematic +	7.9 %	8.8 %	8.2 %
Total systematic -	8.0 %	9.0 %	8.4 %
Total uncertainty	0.06	0.10	0.08

Table 6.16: Systematic uncertainties on the cross section measurements using method no.1 (top) and no.2 (bottom) for the inclusive cross sections in $e^+ p$ (left column), $e^- p$ (middle column) and $e^\pm p$ (right column). All other details as stated in the caption of Table 6.8.

Chapter 7

Conclusions

All available data collected during the lifetime of the ZEUS experiment, with an integrated luminosity of 0.5 fb^{-1} , were used to search for high- P_T isolated electrons and muons in events with large missing transverse momentum. In the region of large hadronic P_T , the ZEUS data did not confirm the excess of events previously observed by the H1 Collaboration. In the region of $P_T^X > 25 \text{ GeV}$, 6 isolated electron events were found in $e^\pm p$ data compared to an expectation of 7.6, whilst 5 events with isolated muon passed the selection compared to 5.5 from Monte Carlo simulation. In total, 40 events matched the criteria in data compared to 48 in Monte Carlo. The overall number of data events was thus below the estimate from simulation but still compatible with the Standard Model expectation, comprising mostly single W boson production.

The isolated lepton events were subsequently used to measure the production cross section of single W bosons in $e^+ p$, $e^- p$ and $e^\pm p$ collisions, as well as the cross sections for the exclusive processes, in which the W subsequently decays via $W \rightarrow e\nu_e$ and $W \rightarrow \mu\nu_\mu$. The measured cross sections are all consistent with the predictions of the Standard Model.

The total production cross section for single W bosons was measured to be

$$\sigma(ep \rightarrow lWX) = 0.93_{-0.23}^{+0.26}(\text{stat.}) \pm 0.08(\text{syst.}) \text{ pb} \quad (7.1)$$

This measurement supersedes the previously published value of $0.9_{-0.7}^{+1.0}(\text{stat.}) \pm 0.2(\text{syst.}) \text{ pb}$, based on 48 pb^{-1} from ZEUS [15], with a four-fold increase in precision that is the result of an order-of-magnitude increase in luminosity obtained by the experiment.

The statistical significance of the measurement, as calculated from the probability of measuring an equal or larger cross section in data for a Standard Model prediction containing no single W boson production, was obtained as 8.3×10^{-7} (6.7×10^{-8}) for the case where the systematic uncertainties were (were not) taken into account. Hence, this measurement provides strong evidence for the production of single W bosons in ep collisions at HERA with a significance of 4.8σ (5.3σ).

The above statistical significance excluding systematic uncertainties was calculated in detail as follows:

1. All possible numbers of isolated electrons, n_e , and muons, n_μ , were collected that would have given a cross section less than what was observed in the measurement:

$(n_e = 0, n_\mu = 0)$, $(n_e = 0, n_\mu = 1)$ etc.

This was done by generating the likelihood distribution for each combination of n_e and n_μ and minimising $-\ln L(\sigma)$ to verify that the resultant cross section was less than 0.93.

2. The likelihood for obtaining one of the combinations of n_e and n_μ in absence of single W boson production was calculated using

$$L = \frac{e^{-m_e} m_e^{n_e}}{n_e!} \frac{e^{-m_\mu} m_\mu^{n_\mu}}{n_\mu!} \quad (7.2)$$

where $m_i = N_{\text{bkgd}}^i$ for each channel.

3. These likelihoods were summed over all possible combinations of n_e and n_μ that were collected in step 1. This sum corresponds to the probability of obtaining a cross section less than what was actually measured in a scenario where single W boson production does not contribute.
4. Subtracting this sum from unity, thus, gives the probability of measuring an *equal or larger cross section* than what was actually measured in a world where single W boson production does not contribute. This value is then the statistical significance of the measurement.

To obtain the statistical significance *including* systematic uncertainties a similar procedure was adopted, the only difference lay in the likelihood distribution that was generated in the first step: For each of the dominant systematic uncertainties a normalisation factor was generated with a Gaussian spread centered on unity and with width equal to the uncertainty. This normalisation factor was then applied to the corresponding Standard Model prediction in the likelihood function $L(\sigma)$. The value of the likelihood for a given σ was taken to be the average of 10^3 values generated using these normalisation factors.

The cross section result is limited by its statistical uncertainty. So, further improvement can only be gained from an increase in luminosity. After the shutdown of the experimental program in high-energy physics at DESY and the dismantling of HERA and the H1 and ZEUS detectors, the only possibility to increase the luminosity lies in combining the H1 and ZEUS data sets. This has been performed by collaborators from H1 and ZEUS and is in the process of being published [137]. The measurement is based on the combined H1 and ZEUS data sets comprising 0.98 fb^{-1} and obtains the total single W boson production cross section as [137]:

$$\sigma(ep \rightarrow l W X) = 1.06 \pm 0.16(\text{stat.}) \pm 0.07(\text{syst.}) \text{ pb} \quad (7.3)$$

This measurement is in agreement with the result presented in this thesis and constitutes a reduction of the statistical error by almost a factor $1/\sqrt{2}$, as expected from a two-fold increase in available luminosity.

Bibliography

- [1] J.J. Thomson. *Cathode Rays*. The London, Edinburgh, and Dublin Philosophical Magazine and Journal of Science, Fifth Series, p.296, 1897.
- [2] G.J. Stoney. *On the Physical Units of Nature*. Philosophical Magazine, Series 5, Volume 11:384, 1881.
- [3] DONUT Coll. , K. Kodama et al. *Observation of Tau Neutrino Interactions*. Phys. Lett., B 504:218, 2001. [arXiv:hep-ex/0012035](#).
- [4] C. Amsler et al. Phys. Lett., B 667:1, 2008.
- [5] SNO Coll. , Q.R. Ahmad et al. *Measurement of the rate $\nu_e + d \rightarrow p + p + e^-$ interactions produced by ^8B solar neutrinos at the Sudbury Neutrino Observatory*. Phys. Rev. Lett., 87:071301, 2001. [arXiv:nucl-ex/0106015](#).
- [6] H1 Coll. , C. Adloff et al. *Observation of Events with an Isolated High-Energy Lepton and Missing Transverse Momentum at HERA*. Eur. Phys. J., C 5:575, 1998. [arXiv:hep-ex/9806009](#).
- [7] H1 Coll. , V. Andreev et al. *Isolated electrons and muons with missing transverse momentum at HERA*. Phys. Lett., B 561:241–257, 2003. [arXiv:hep-ex/030130v1](#).
- [8] T. Kon, T. Kobayashi, S. Kitamura. *Is a high P_T muon of the $e^+p \rightarrow \mu^+X$ event observed at HERA a signature of the stop?*. Phys. Lett., B 376:227, 1996. [arXiv:hep-ph/9601338](#).
- [9] H. Fritzsche, D. Holtmannspötter. *The Production of Single t -Quarks at LEP and HERA*. Phys. Lett., B 457:186, 1999. [arXiv:hep-ph/9901411](#).
- [10] C. Diaconu et al. *High P_T Leptons and W Production at HERA*. J. Phys., G 25:1412, 1999. [arXiv:hep-ph/9901335](#).
- [11] W. Rodejohann, K. Zuber. *Signatures of heavy Majorana neutrinos and HERA's isolated lepton events*. Phys. Rev., D 62:094017, 2000. [arXiv:hep-ph/0005270](#).
- [12] H1 Coll. , C. Adloff et al. *A Search for Excited Fermions at HERA*. Eur. Phys. J., C 17:567, 2000. [arXiv:hep-ex/0007035](#).
- [13] A. Belyaev. *Single Top Quark in the SM and Beyond*. In *8th International Workshop on Deep-Inelastic Scattering (DIS 2000)*. [arXiv:hep-ph/0007058](#).
- [14] T. Kon et al. *Single Sbottom/Scharm Production at HERA in an R-Parity Breaking Supersymmetric Model*. Phys. Lett., B 494:280, 2000. [arXiv:hep-ph/0007200](#).
- [15] ZEUS Coll. , J. Breitweg et al. *W Production and the Search for Events with an Isolated High-Energy Lepton and Missing Transverse Momentum at HERA*. Phys. Lett., B 471:411, 2000. [arXiv:hep-ex/9907023](#).
- [16] ZEUS Coll. , S. Chekanov et al. *Search for single-top production in ep collisions at HERA*. Phys. Lett., B 559:153, 2003. [arXiv:hep-ex/0302010](#).
- [17] ZEUS Coll. , S. Chekanov et al. *Isolated tau leptons in events with large missing transverse momentum at HERA*. Phys. Lett., B 583:41, 2004. [arXiv:hep-ex/0302010](#).
- [18] H1 Coll. , A. Aktas et al. *Tau Lepton Production in ep Collisions at HERA*. Eur. Phys. J., C48:699–714, 2006. [arXiv:hep-ex/0604022](#).

- [19] ZEUS Coll. , S. Chekanov et al. *Search for events with an isolated lepton and missing transverse momentum and a measurement of W production at HERA*. Phys. Lett., B 672:106–115, 2009. arXiv:0807.0589v3 [hep-ex].
- [20] UA1 Coll. , G. Arnison et al. *Experimental Observation of Isolated Large Transverse Energy Electrons with Associated Missing Energy at $\sqrt{s} = 540$ GeV*. Phys. Lett., B 122:103, 1983.
- [21] M. Klein, T. Riemann. *Electroweak Interactions Probing the Nucleon Structure*. Z. Phys., C 24:151, 1984.
- [22] ZEUS Coll. , S. Chekanov et al. *Measurement of High- Q^2 Neutral Current Deep Inelastic e^-p Scattering Cross Sections with a Longitudinally Polarised Electron Beam at HERA*. Eur. Phys. J., C 62:625–658, 2009. arXiv:0901.2385v1 [hep-ex].
- [23] A. Cooper-Sarkar R. Devenish. *Deep Inelastic Scattering*. Oxford University Press, 2004.
- [24] H1 and ZEUS Coll. . *Compiled H1 and ZEUS NC and CC plots for conferences*. ZEUS-prel-09-001.
- [25] J.A.M. Vermaseren. *Two Photon Processes at very High Energies*. Nucl. Phys., B 229:347, 1983.
- [26] U. Baur, J.A.M. Vermaseren, D. Zeppenfeld. *Electroweak Vector Boson Production in High-Energy ep Collisions*. Nucl. Phys., B 375:3, 1992.
- [27] C. Schwanenberger K-P. Diener, M. Spira. *Photoproduction of W Bosons at HERA: QCD Corrections*. Eur. Phys. J., C 25, 25:405–411, 2002.
- [28] G.A. Voss, B.H. Wiik. *The Electron proton collider HERA*. Ann. Rev. Nucl. Part. Sci., 44:413, 1994.
- [29] B.H. Wiik. *HERA status*. In W. Buchmüller, G. Ingelman, editors, *Proc. Workshop on Physics at HERA*, volume 1, pages 1–16. DESY, Hamburg, Germany, 1992.
- [30] D.A. Diver. *A Plasma Formulary for Physics, Technology, and Astrophysics*. pp. 46–48, Wiley-VCH, 2001.
- [31] H1 Coll. , I. Abt et al. *The H1 Detector at HERA*. Nucl. Inst. Meth., A 386:310, 1997.
- [32] *The ZEUS Detector*. Status Report (unpublished), DESY, 1993.
- [33] R.G. Milner on behalf of the HERMES Collaboration. *The HERMES Experiment*. Nucl. Phys., A 622:16–30, 1997.
- [34] E. Hartouni et al. *An Experiment to Study CP Violation in the B System Using an Internal Target at the HERA Proton Ring*. Design Report, DESY-PRC 95/01, 1995.
- [35] F. Willeke. *HERA Status and Perspectives of Future Lepton-Hadron Colliders*. In *Proceedings of EPAC 2002*. Paris, France, 2002. <http://epaper.kek.jp/e02/PAPERS/TUYGB001.pdf>.
- [36] K. Oliver et al. *A Minimum Bias Z Vertex Distribution for 2005-2007 eP interactions at ZEUS*. ZEUS Internal Note, ZEUS-07-008, 2007.
- [37] C.W. Schimdt. *Review of negative hydrogen ion sources*. In *Proceedings of 1990 Linear Accelerator Conference*. Albuquerque, USA, 1991. <http://lss.fnal.gov/archive/linac/fermilab-lu-166.pdf>.
- [38] A.A. Sokolov, I.M. Ternov. *On Polarization and Spin Effects in the Theory of Synchrotron Radiation*. Sov. Phys. Dokl., 8:1203, 1964.
- [39] D.P. Barber et al. *The first achievement of longitudinal spin polarization in a high energy electron storage ring*. Phys. Lett., B 343:436–443, 1995.
- [40] D.P. Barber et al. *High Spin Polarization at the HERA Electron Storage Ring*. Nucl. Inst. Meth., A 338:166, 1994.
- [41] M. Klein, R. Yoshida. *Collider Physics at HERA*. Progress in Particle and Nuclear Physics, 61:343–393, 2008.
- [42] K. Long, K.P. Schüller. *Polarisation measurements on e^\pm beams*. Nucl. Inst. Meth., A 494:75–80, 2002.
- [43] T. Behnke et al. *A New Analysis for the Transverse Polarimeter at HERA II*. POL2000 Group, DESY, July 2004. <http://www.desy.de/~pol2000/tpol/analysis/JennyEPS2003paper.ps.gz>.

- [44] D.P. Barber et al. *The HERA polarimeter and the first observation of electron spin polarization at HERA*. Nucl. Inst. Meth., A 329:79, 1993.
- [45] Encyclopedia of Laser Physics, Technology. http://www.rp-photonics.com/pockels_cells.html.
- [46] J. Böhme. *Precision measurement with the transverse polarimeter at HERA II*. Eur. Phys. J., C 33:1067–1069, 2004.
- [47] ZEUS Coll. , S. Chekanov et al. *Measurement of Charged Current Deep Inelastic Scattering Cross Sections with a Longitudinally Polarised Electron Beam at HERA*. Eur. Phys. J., C 61:223, 2009. [arXiv:0812.4620v3](https://arxiv.org/abs/0812.4620v3) [hep-ex].
- [48] F. Corriveau et al. *Calibration of the HERA Transverse Polarimeter for the 2003/2004 Data*. POL2000 Group, DESY, 2004. http://www.desy.de/~pol2000/documents/tpolcalib2004_v3.1.pdf.
- [49] M. Beckmann et al. *The Longitudinal Polarimeter at HERA*. Nucl. Inst. Meth., A 479:334–348, 2002. [arXiv:physics/0009047v1](https://arxiv.org/abs/physics/0009047v1) [physics.ins-det].
- [50] A. Airapetian, R. Fabbri, B. Zihlmann. *Data Quality of LPOL Measurements*. POL2000 Group, DESY, 2004. <http://www.desy.de/~pol2000/documents/lpol2004dq.ps.gz>.
- [51] A. Andresen et al. *Construction and Beam Test of the ZEUS Forward and Rear Calorimeter*. Nucl. Inst. Meth., A 309:101, 1991.
- [52] M. Derrick et al. *Design and Construction of the ZEUS Barrel Calorimeter*. Nucl. Inst. Meth., A 309:77, 1991.
- [53] A. Bernstein et al. *Beam Tests of the ZEUS Barrel Calorimeter*. Nucl. Inst. Meth., A 336:23, 1993.
- [54] A. Bamberger et al. *The Presampler for the Forward and Rear Calorimeter in the ZEUS Detector*. Nucl. Inst. Meth., A 382:419, 1996.
- [55] ZEUS Coll. . *A Presampler for the ZEUS Barrel Calorimeter*. ZEUS Internal Note, ZEUS-95-133, 1995.
- [56] B. Foster et al. *The Design and Construction of the ZEUS Central Tracking Detector*. Nucl. Inst. Meth., A 338:254, 1994.
- [57] B. Foster et al. *The Performance of the ZEUS Central Tracking Detector z-by-Timing Electronics in a Transputer Based Data Acquisition System*. Nucl. Phys. Proc. Suppl., B 32:181, 1993.
- [58] R. Hall-Wilton et al. *The CTD Tracking Resolution*. ZEUS Internal Note, ZEUS-99-024, 1999.
- [59] T. Haas et al. *The ZEUS microvertex detector*. Nucl. Inst. Meth., A 549:37–43, 2005.
- [60] A. Polini et al. *The design and performance of the ZEUS micro vertex detector*. Nucl. Inst. Meth., A 581:656, 2007. [arXiv:0708.3011v1](https://arxiv.org/abs/0708.3011v1) [physics.ins-det].
- [61] U. Koetz et al. *Silicon strip detectors with capacitive charge division*. Nucl. Inst. Meth., A 235:481, 1985.
- [62] H. Bethe, W. Heitler. *On the Stopping of fast particles and on the creation of positive electrons*. Proc. Roy. Soc. Lond., A146:83, 1934.
- [63] K. J. Gaemers, M. van der Horst. *The Process $e^- p \rightarrow \gamma e^- p$ as a Fast Luminosity Monitor for the Hera Collider*. Nucl. Phys., B 316:269, 1989.
- [64] K. Piotrkowski, M. Zachara. *Determination of the ZEUS Luminosity in 1994*. ZEUS Internal Note, ZEUS-95-138, 1995.
- [65] ZEUS Luminosity Group, J. Andrusków et al. *Luminosity Measurement in the ZEUS Experiment*. ZEUS Internal Note, ZEUS-01-004, 2001.
- [66] J. Andrusków et al. *Luminosity Measurement in the ZEUS Experiment*. Acta Phys. Pol., B 32:2025, 2001.
- [67] ZEUS Luminosity Group, J. Chwastowski et al. *Aerogel Cherenkov detectors for the luminosity measurement at HERA*. ZEUS Internal Note, ZEUS-02-013, 2002.
- [68] J. Chwastowski et al. *Aerogel Cherenkov detectors for the luminosity measurement at HERA*. Nucl. Inst. Meth., A 504:222–227, 2003.

- [69] S.D. Paganis. *A Luminosity Spectrometer for the ZEUS Experiment at HERA*, 2000. Talk at *9th Int. Conf. on Calorimetry in Particle Physics, Annecy, France, Oct. 2000*, arXiv:hep-ex/0011080.
- [70] M. Helbich et al. *The Spectrometer System for Measuring ZEUS Luminosity at HERA*. Nucl. Inst. Meth., A 565:572, 2005. arXiv:physics/0512153v1 [physics.ins-det].
- [71] H. Helbich et al. *The Spectrometer System for Measuring ZEUS Luminosity at HERA*. ZEUS Internal Note, ZEUS-06-002, 2006.
- [72] Y. Ning et al. *Luminosity Spectrometer Measurement*. ZEUS Internal Note, ZEUS-05-006, 2005.
- [73] ZEUS Coll. , R. Carlin et al. *The Trigger of ZEUS, a Flexible System for a High Bunch Crossing Rate Collider*. Nucl. Inst. Meth., A 379:542, 1996.
- [74] Catherine L. Fry. *Measurement of spin-dependent charged current deep inelastic scattering cross sections using the ZEUS detector at HERA*. Ph.D. thesis, Imperial College London, 2007.
- [75] P. Allfrey et al. *The design and performance of the ZEUS global tracking trigger*. Nucl. Inst. Meth., A 580:1257, 2007.
- [76] W.H. Smith et al. *The ZEUS Calorimeter First Level Trigger*. Nucl. Inst. Meth., A 355:278, 1995.
- [77] G.P. Heath et al. *The ZEUS First Level Tracking Trigger*. Nucl. Inst. Meth., A 315:431, 1992.
- [78] B.G. Bylsma et al. *A Fast Cluster Finding Processor for the ZEUS Calorimeter*. Nucl. Inst. Meth., A 337:512, 1994.
- [79] A. Quadt et al. *The Design and Performance of the ZEUS Central Tracking Detector Second Level Trigger*. Nucl. Inst. Meth., A 438:472, 1999.
- [80] G.F. Hartner. *VCTRAK Briefing: Program and Math*. ZEUS Internal Note, ZEUS-98-058, 1998.
- [81] G.F. Hartner. *VCTRAK(3.07/04): Offline Output Information*. ZEUS Internal Note, ZEUS-97-064, 1997.
- [82] H. Beier, A. Caldwell. *Track-CAL Matching with Parametrized CAL Resolution and Inactive Material Effects*. ZEUS Internal Note, ZEUS-95-040, 1995.
- [83] Available at http://www-zeus.desy.de/ZEUS_ONLY/analysis/orange/.
- [84] R. Brun et al. GEANT3. Technical Report CERN-DD/EE/84-1, CERN, 1987.
- [85] H. Stadie et al. *Monte Carlo mass production for the ZEUS experiment on the Grid*. Nucl. Inst. and Meth., A559:43, 2006.
- [86] D. J. Griffiths. *Introduction to Electrodynamics*. Addison Wesley, 1999.
- [87] B. Andersson et al. *Parton Fragmentation and String Dynamics*. Phys. Rep., 97:31, 1983.
- [88] G. Altarelli. Phys. Rep., 81:1, 1982.
- [89] Yu. L. Dokshitzer. *Basics of Perturbative QCD*. Editions Frontiers, 1991.
- [90] B. R. Webber. *A QCD model for jet fragmentation including soft gluon interference*. Nucl. Phys., B 238:492, 1984.
- [91] H. Plothow-Besch. *PDFLIB, CERN Program Library Entry W5051*. CERN, Geneva, 2000.
- [92] U. Baur, J.A.M. Vermaseren, D. Zeppenfeld. *Electroweak Vector Boson Production in High-Energy ep Collisions*. Nucl. Phys., B 375:3, 1992.
- [93] H.L. Lai et al. *Improved Parton Distributions from Global Analysis of Recent Deep Inelastic Scattering and Inclusive Jet Data*. Phys. Rev., D 55:1280, 1997.
- [94] CTEQ Coll. , H.L. Lai et al. *Global QCD Analysis of Parton Structure of the Nucleon: CTEQ5 Parton Distributions*. Eur. Phys. J., C 12:375, 2000. arXiv:hep-ph/9903282v3.
- [95] M. Glück, E. Reya, A. Vogt. *Parton Distributions for High Energy Collisions*. Z. Phys., C 53:127, 1992.
- [96] E. Reya M. Glück, A. Vogt. *Dynamical Parton Distributions of the Proton and Small x Physics*. Z. Phys., C 67:433, 1995.

- [97] T. Sjöstrand, M. Bengtsson. *The Lund Monte Carlo for Jet Fragmentation and e^+e^- Physics: JETSET Version 6.3: An Update*. Comp. Phys. Comm., 43:367, 1987.
- [98] T. Sjöstrand. *High-Energy Physics Event Generation with PYTHIA 5.7 and JETSET 7.4*. Comp. Phys. Comm., 82:74, 1994.
- [99] K.-P. Diener, C. Schwanenberger, M. Spira. *Photoproduction of W Bosons at HERA: Reweighting Method for implementing QCD Corrections in Monte Carlo Programs*. 2003. [arXiv:hep-ex/0302040v1](https://arxiv.org/abs/hep-ex/0302040v1).
- [100] P. Aurenche et al. *Higher order QCD corrections to the photoproduction of a direct photon at HERA*. Z. Phys., C 56:589, 1992.
- [101] J.P. Guillet P. Aurenche, M. Fontannaz. *Parton Distributions in the Photon*. Z. Phys., C 64:621, 1994.
- [102] H. Spiesberger. *HERACLES and DJANGO: Event Generation of ep Interactions at HERA Including Radiative Processes*, 2005. <http://wwwthep.physik.uni-mainz.de/~hspiesb/djangoh/djangoh.html>.
- [103] A. Edin G. Ingelman, J. Rathsmann. LEPTO 6.5: *A Monte Carlo Generator for Deep Inelastic Lepton-Nucleon Scattering*. Comp. Phys. Comm., 101:108, 1997.
- [104] L. Lönnblad. *ARIADNE Version 4 – A Program for Simulation of QCD Cascades Implementing the Colour Dipole Model*. Comp. Phys. Comm., 71:15, 1992.
- [105] T. Abe. *GRAPE-DILEPTON (Version 1.1) – A Generator for Dilepton Production in ep Collisions*. Comp. Phys. Comm., 136:126, 2001. [arXiv:hep-ph/0012029](https://arxiv.org/abs/hep-ph/0012029).
- [106] T. Ishikawa et al. *GRACE Manual: Automatic Generation of Tree Amplitudes in Standard Models: Version 1.0*. KEK-92-19, 1993.
- [107] G. Marchesini et al. *HERWIG: A MONTE CARLO EVENT GENERATOR FOR SIMULATING HADRON EMISSION REACTIONS WITH INTERFERING GLUONS*. Comp. Phys. Comm., 67:465, 1992.
- [108] ZEUS Coll. , J. Breitweg et al. *Comparison of ZEUS Data with Standard Model Predictions for $e^+p \rightarrow e^+X$ Scattering at High x and Q^2* . Z. Phys., C 74:207, 1997. [arXiv:hep-ex/9702015](https://arxiv.org/abs/hep-ex/9702015).
- [109] A. Kappes. *Verwendung Neuronaler Netze zur Identifikation des gestreuten Elektrons in ep -Ereignissen mit hohem Q^2 bei ZEUS*. Diploma thesis, Universität Bonn, Bonn, Germany, 1997.
- [110] A. López-Durán Viani, S. Schlenstedt. *Electron Finder Efficiencies and Impurities. A Comparison Between SINISTRA95, EM and EMNET*. ZEUS Internal Note, ZEUS-99-077, 1999.
- [111] V. Kuzmin for the ZEUS Coll. . *Identification of leptons by the ZEUS Calorimeter*. Nucl. Inst. Meth., A 453:336, 2000.
- [112] A. Geiser. *GMUON - a general ZEUS muon finder*. ZEUS Internal Note, ZEUS-06-016, 2006.
- [113] S. Catani et al. *Longitudinally Invariant $K(T)$ Clustering Algorithms for Hadron-Hadron Collisions*. Nucl. Phys., B406:187, 1993.
- [114] S.D. Ellis, D.E. Soper. *Successive Combination Jet Algorithm for Hadron Collisions*. Phys. Rev., D 48:3160, 1993.
- [115] J.E. Huth et al. *Toward a Standardization of Jet Definitions*. In E.L. Berger, editor, *Research Directions for the Decade. Proceedings of Summer Study on High Energy Physics, 1990*, page 134. World Scientific, 1992.
- [116] Y.I. Azimov et al. *Hump-Backed QCD Plateau in Hadron Spectra*. Z. Phys., C 31:213, 1986.
- [117] J. Engelen S. Bentvelsen, P. Kooijman. *Reconstruction of (x, Q^2) and Extraction of Structure Functions in Neutral Current Scattering at HERA*. In W. Buchmüller, G. Ingelman, editors, *Proc. Workshop on Physics at HERA*, volume 1, page 23. DESY, Hamburg, Germany, 1992.
- [118] Y. Ri. *Measurement of e^-p Neutral Current Deep Inelastic Scattering Cross Sections with Longitudinally Polarized Electron Beams at $\sqrt{s} = 318$ GeV*. Ph.D. thesis, Tokyo Metropolitan University, 2007.
- [119] F. Jacquet, A. Blondel. *Detection of the Charged Current Event – Method II*. In U. Amaldi, editor, *Proceedings of the Study for an ep Facility for Europe*, page 391. Hamburg, Germany, 1979.

- [120] K. Horton. *Non-uniformity corrections for the BCAL electron energy*. ZEUS Internal Note, ZEUS-08-004, 2008.
- [121] S. Kananov. *The noise study for the 1995 data in the ZEUS Calorimeter*. ZEUS Internal Note, ZEUS-97-018, 1997.
- [122] A. Savin. *Study of Calorimeter Noise in the 1996 Data*. ZEUS Internal Note, ZEUS-98-007, 1998.
- [123] M. Martinez. *Calorimeter Noisy Cell Study for 1998-2000 ZEUS Data*. ZEUS Internal Note, ZEUS-00-016, 2000.
- [124] H. Lim. *Noise for 2002/2003 data*. Presentation at New Data Tools Meeting, DESY, February 2004.
- [125] A. Caldwell, W. Liu, B. Straub. *BCAL Electron Studies Part I: MC and Test Beam Energy Studies*. ZEUS Internal Note, ZEUS-98-02, 1998.
- [126] ZEUS Coll. , J. Breitweg et al. *Measurement of High- Q^2 Neutral Current e^+p Deep Inelastic Scattering Cross Sections at HERA*. Eur. Phys. J., C 11:427, 1999. [arXiv:hep-ex/9905032](https://arxiv.org/abs/hep-ex/9905032).
- [127] M. Wodarczyk. *Measurement of the F_2 Structure Function of the Proton at HERA from 1996 and 1997 ZEUS Data*. Ph.D. thesis, University of Wisconsin, 1999.
- [128] J. Grosse-Knetter. *Corrections for the Hadronic Final State*. ZEUS Internal Note, ZEUS-98-031, 1998.
- [129] ZEUS Coll. , A. Andresen et al. Calorimeter group. *Response of a Uranium-Scintillator Calorimeter to Electrons, Pions and Protons in the Momentum Range 0.5 – 10 GeV/c*. Nucl. Inst. Meth., A 290:95, 1990.
- [130] F. Willeke. *Summary of the HERA Proton-Positron Luminosity Run 2004*. HERA Note, HERA-04-01, 2004.
- [131] Syed Umer Noor. *Measurement of Neutral Current electron-proton cross sections with longitudinally polarised electrons using the ZEUS detector*. Ph.D. thesis, York University, Toronto, 2007.
- [132] ZEUS Coll. , S. Chekanov et al. *Measurement of the Neutral Current Cross-Section and F_2 Structure Function for Deep Inelastic e^+p Scattering at HERA*. Eur. Phys. J., C 21:443, 2001. [arXiv:hep-ex/0105090](https://arxiv.org/abs/hep-ex/0105090).
- [133] H. Spiesberger. *DJANGO6 Version 2.4 – A Monte Carlo Generator for Deep Inelastic Lepton Proton Scattering Including QED and QCD Radiative Effects*, 1996. <http://www.desy.de/~hspiesb/django6.html>.
- [134] G. Abbiendi et al. *Observation of $J/\Psi \rightarrow \mu^+\mu^-$ in the first 124 nb $^{-1}$ of 1993 run*. ZEUS Internal Note, ZEUS-93-120, 1993.
- [135] R. Ciesielski. *MuBac subroutine (v1.0)*. http://www-zeus.desy.de/~robertc/ZEUS_ONLY/mubac.html.
- [136] G. Abbiendi. *Global tracking of muons in the Barrel and Rear region*. ZEUS Internal Note, ZEUS-99-063, 1999.
- [137] H1 and ZEUS Collaborations, F.D. Aaron et al. *Events with an Isolated Lepton and Missing Transverse Momentum Measurement of W Production at HERA*. DESY-09-140, to be published in JHEP. [arXiv:0911.0858v1](https://arxiv.org/abs/0911.0858v1) [hep-ex].

List of Figures

1.1	Results of the H1 experiment's search for isolated leptons as published in 2003 [7]. The variables shown are the polar angle of the scattered lepton (top left), the difference in azimuthal angle between the lepton and the hadronic system (top right), the transverse mass (bottom left, see Equation 5.18 for the definition) and the hadronic transverse momentum (bottom right).	3
2.1	Electron-proton interaction in the Quark-Parton Model.	8
2.2	Deep inelastic scattering via (a) Neutral Current and (b) Charged Current.	9
2.3	Measurements with the ZEUS and H1 detectors of the Charged Current cross section with e^+p (blue) and e^-p (red) data versus lepton beam polarisation P_e in the region of $y < 0.9$ and $Q^2 > 400 \text{ GeV}^2$ [24]. The straight bands indicate the corresponding SM prediction and the uncertainty on it from the parton density functions.	11
2.4	Measurements from the ZEUS and H1 detectors of the Neutral Current (blue) and Charged Current (red) differential cross sections $d\sigma/dQ^2$ versus Q^2 in the region of $y < 0.9$ [24]. The curves indicate the corresponding SM prediction.	12
2.5	A typical Charged Current event measured by ZEUS.	13
2.6	Feynman diagrams of Photoproduction: (a) QCD Compton process, (b) boson-gluon fusion.	14
2.7	The QED Compton process	15
2.8	Feynman diagrams of lepton pair production: (a) Bethe-Heitler process, (b) Compton-like process.	16
2.9	Main Feynman diagrams for single W production: (a) and (b) are the dominant diagrams, (c) involves a triple gauge coupling, (d) and (e) contain off-shell W bosons, (f) and (g) contain a second W propagator and are therefore suppressed.	17
3.1	The HERA ring collider with the four experiments H1, HERMES, HERA-B and ZEUS and the pre-accelerator PETRA.	19
3.2	The luminosity delivered by HERA over the period 1992–2007. Run periods are split into high energy runs, denoted by HERA I and II, as well as medium (MER) and low energy runs (LER).	22

3.3	The position of the longitudinal and transverse polarimeter and the spin rotators around the experiments on the HERA ring. The direction of the lepton spin is indicated with black (transverse) and pink (longitudinal polarisation) arrows. . . .	23
3.4	Compton scattering of an incident photon with energy E_λ off an electron with energy E_e . The scattered photon travels with energy E_γ in the direction specified by θ_{lab} and ϕ	24
3.5	A cross sectional view of the ZEUS detector highlighting its subcomponents. The human on the left is drawn to indicate the scale.	27
3.6	The sub-divisions of the ZEUS calorimeter.	28
3.7	(a) Distribution of wires and the resultant field in a CTD cell. (b) The nine superlayers of the CTD with cells inclined by the Lorentz angle.	30
3.8	The bottom half of the MVD showing the ladders in the barrel, the forward wheels with silicon sensors on the left and the readout cables and services on the right. .	31
3.9	Layout of the MVD ladders around the beampipe in the cross sectional view (left) and an MVD half-module showing the r - ϕ and r - z strips (right).	32
3.10	Diagram of the luminosity measuring devices: the original photon calorimeter plus ‘electron tagger’ and the spectrometer consisting of the dipole magnet and the two calorimeters, CAL1 and CAL2.	33
3.11	The ZEUS three-level trigger system [74] and the in- and output rates at every level. Only the two main components of the ZEUS detector, CTD and CAL, are shown in detail, but other components that feed into the global trigger levels are similar. The CTD SLT was replaced by the Global Tracking Trigger (GTT) in 2006 [75]. .	35
4.1	The Monte Carlo event simulation and the data taking chains.	39
4.2	Feynman diagrams that contribute to the electroweak corrections: (a) Initial state radiation, (b) final state radiation, (c) vertex correction, (d) propagator correction.	40
4.3	Feynman diagrams of higher order QCD processes: (a) 2-jet production via boson-gluon fusion and (b) via gluon radiation, (c) 3-jet production through final and (d) through initial state radiation.	42
4.4	(a) The dependence of the total cross section for single W boson production and of the cross sections for individual production channels on the lepton beam polarisation at $s = 318$ GeV. (b) The dependence of these cross sections on u_{cut} at the same centre-of-mass energy.	44
4.5	The double differential cross section $d^2\sigma_{\text{EPVEC}}/dP_T^W dy_W$ (in units of pb/GeV) used by EPVEC (colours) and the NLO reweighting factors (numbers) for single W^\pm production in e^+p collisions at a centre of mass energy of 300 GeV. The quantities P_T^W and y_W are the transverse momentum and the rapidity of the W boson, respectively. Entries in bins are zero where not specified.	46

4.6	The double differential cross section $d^2\sigma_{\text{EPVEC}}/dP_T^W dy_W$ (in units of pb/GeV) used by EPVEC (colours) and the NLO reweighting factors (numbers) for single W^\pm production in e^+p collisions at a centre of mass energy of 318 GeV. All other details as in Fig. 4.5.	47
4.7	The double differential cross section $d^2\sigma_{\text{EPVEC}}/dP_T^W dy_W$ (in units of pb/GeV) used by EPVEC (colours) and the NLO reweighting factors (numbers) for single W^\pm production in e^-p collisions at a centre of mass energy of 318 GeV. All other details as in Fig. 4.5.	48
5.1	The muon finder output, P_μ^{MV} , for MC samples of 4×10^5 hadrons (filled histogram) and muons, respectively, with initial energy uniformly distributed in the region of 1–40 GeV [111]. The scale on the vertical axis is arbitrary.	55
5.2	The acoplanarity angle in the transverse plane.	58
5.3	Isolines of the scattered electron’s energy, E'_e , and polar angle, θ_e in the x - Q^2 kinematic plane [118]. The dashed lines in the background indicate isolines for the kinematic variable y	61
5.4	Isolines of the hadronic system’s transverse momentum, P_T^X , and energy and longitudinal momentum balance, δ_h in the x - Q^2 kinematic plane [118]. The dashed lines in the background indicate isolines for the kinematic variable y	62
5.5	Isolines of the hadronic system’s energy, E'_h , and polar angle, γ_h in the x - Q^2 kinematic plane [118]. The dashed lines in the background indicate isolines for the kinematic variable y	63
5.6	The mean of the Gaussian fit to the E_{DA}/E_{cor1} distribution versus (a) DME and (b) DCE for positrons in Monte Carlo and correspondingly for data in (c) and (d) [120]. The error bars on the points represent the error on the Gaussian mean and are smaller than the marker size.	66
5.7	Examples of background events: (a) cosmic muon, (b) cosmic shower, (c) halo-muon, (d) halo-muon and ep event.	69
6.1	Distribution of MC events in the isolated electron search for the quantities Z_{vtx} and $E - p_z$. The the W signal MC only comprises the electron decay channel of the W boson in these plots.	73
6.2	Distribution of MC events in the isolated electron search for the quantities P_T^{ex1IR} and P_T^{miss} . The W signal MC only comprises the electron decay channel of the W boson in these plots. The legend of Fig 6.1 applies.	74
6.3	Distribution of MC events in the isolated electron search for the quantities ξ_e^2 ($= Q_{\text{el}}^2$ for NC) and ϕ_{acop} . The W signal MC only comprises the electron decay channel of the W boson in these plots. The legend of Fig 6.1 applies.	75
6.4	Distribution of MC events in the isolated electron search for the quantity $V_{\text{ap}}/V_{\text{p}}$ below and above the P_T^e threshold. The W signal MC only comprises the electron decay channel of the W boson in these plots. The legend of Fig 6.1 applies.	76

6.5	Distribution of MC events for various properties of the isolated electron. The W signal MC only comprises the electron decay channel of the W boson in these plots. The legend of Fig 6.1 applies.	77
6.6	(a)–(c) Distribution of MC events for various properties of the isolated electron. The W signal MC only comprises the electron decay channel of the W boson in these plots. The legend of Fig 6.1 applies. (d) Cosmic muon event that passed the event selection and had to be rejected ‘by hand’.	78
6.7	Comparison of the data distributions of isolated electrons (points) to the SM expectation for the e^-p collision samples. The light-shaded (yellow) histogram represents the total Standard Model MC prediction, the dark-shaded (blue) area the predicted contribution from events not arising from $ep \rightarrow lWX$. The background to the isolated lepton search is thus shown in dark (blue) and above this, the band of the SM MC histogram (yellow) arises from single W boson production. The error bars on the data points correspond to \sqrt{N} , where N is the number of events.	82
6.8	Comparison of the data distributions of isolated electrons (points) to the SM expectation for the e^+p collision samples. All other details as in Fig. 6.7.	83
6.9	Comparison of the data distributions of isolated electrons (points) to the SM expectation for the $e^\pm p$ collision samples. All other details as in Fig. 6.7.	84
6.10	Comparison of the data distributions of isolated muons (points) to the SM expectation for the $e^\pm p$ collision samples. All other details as in Fig. 6.9.	85
6.11	The negative of the log-likelihood distribution for the two exclusive processes of $ep \rightarrow lWX$ where $W \rightarrow e\nu_e$ (top) and $W \rightarrow \mu\nu_\mu$ (bottom). The minimum marks the measured cross section and the red lines indicate the statistical error bands and the blue line denotes the SM expectation.	90
6.12	The negative of the log-likelihood distribution for the inclusive single W production cross section in e^+p (top), e^-p (middle) and $e^\pm p$ data (bottom). The minimum marks the measured cross section and the red lines indicate the statistical error bands and the blue line denotes the SM expectation.	91
6.13	Neutral Current enriched data and MC samples: Distributions of the polar angle and transverse momentum of the electron, the hadronic transverse momentum and total missing transverse momentum in the event after the rescaling of the NC contribution.	94
6.14	Neutral Current selection: Distributions of the polar angle and transverse momentum of the DIS electron , the hadronic transverse momentum and total missing transverse momentum in the event.	97
6.15	Neutral Current enriched data and MC samples: Distributions of the polar angle and transverse momentum of the second (non-DIS) electron after the rescaling of the NC contribution.	98
6.16	Distributions of the polar angle and transverse momentum of the muons, as well as the hadronic transverse momentum and total missing transverse momentum in the data and MC samples enriched with lepton pair production.	99

6.17	The efficiency of finding a muon with MV versus the azimuthal (ϕ) and polar angle (θ), as well as the transverse momentum of the muon (P_T). The top left plot is the efficiency overall. The points indicate the efficiency in data, whereas the yellow histograms with violet error bands indicate the efficiency in MC.	100
------	--	-----

List of Tables

2.1	The three generations of quarks and leptons with their corresponding quantum numbers of electromagnetic charge (Q_{EM}), strong 'colour' charge (Q_C) and weak isospin (I_W). The values of the latter stated above apply to the left-handed component of the fermions, whereas the right handed component carries $I_W = 0$	6
2.2	The mass of the quarks, fermions and bosons.	7
3.1	Data sets from different years with their beam type, luminosity delivered by HERA and gated by ZEUS and average lepton beam polarisation as measured at the ZEUS detector.	22
4.1	Details of the samples used to simulate single W production via NC in the DIS and resolved (res) modes, as well as via CC in the DIS, elastic (ela) and quasi-elastic (qela) modes. The columns indicate the beam type, the total number of generated events (N_{gen}), the cross section (σ) used before the NLO reweighting and the effective luminosity (\mathcal{L}). The numbers in brackets apply to the lower proton beam energy of 820 GeV. The value of N_{gen} is in some cases a nominal number that agrees with the actual value within 5%.	43
4.2	Details of the samples used to simulate CC and NC events. For the 96-97 data the NC Monte Carlo consisted only of the sample with $Q^2 > 400 \text{ GeV}^2$. All other details as in Table 4.1.	49
4.3	Details of the samples used to simulate lepton pair production via the DIS, elastic (ela) and quasi-elastic (qela) modes. The numbers in brackets indicate the numbers used for the HERA I data set. All other details as in Table 4.1.	50
4.4	(continued) Details of the samples used to simulate the DIS, elastic (ela) and quasi-elastic (qela) modes. All other details as in Table 4.1.	51
6.1	Event requirements for the isolated electron and muon search.	72
6.2	Results of the search for isolated electrons (top) and for isolated muons (bottom). The observed number of data events is compared to the SM prediction (data/SM). The fraction of the SM expectation arising from single W boson production is given in parentheses. The errors comprise statistical and systematic uncertainties added in quadrature. Small discrepancies in the tables are due to rounding to a single decimal place.	80

6.3	Different background contributions with their statistical uncertainties to the search for isolated electrons in e^-p , e^+p and $e^\pm p$ data. The contributions are given for every bin of P_T^X in terms of number of events (first column) and as a percentage of the total SM expectation (second column). The lepton pair production is further split into muon and tau pairs (electron pairs did not contribute any events).	81
6.4	Different background contributions with their statistical uncertainties to the search for isolated muons in e^-p , e^+p and $e^\pm p$ data. The contributions are given for every bin of P_T^X in terms of number of events (first column) and as a percentage of the total SM expectation (second column). The lepton pair production is further split into muon and tau pairs (electron pairs did not contribute any events).	86
6.5	Results of the search for isolated electrons in the reduced phase space used in the cross section measurement. The observed number of data events is compared to the SM prediction (data/SM). The fraction of the SM expectation arising from single W production is given in parentheses. The errors comprise statistical and systematic uncertainties added in quadrature.	87
6.6	Cross section results using method no.1, described in Section 6.3.1. The columns indicate the process and the beam types, the region of hadronic transverse momentum (P_T^X) of the measurement, the centre of mass energy (\sqrt{s}) of the beams, the acceptance (Acc.), the measured cross section from background subtraction ($\sigma_{\text{meas}}^{\text{BS}}$) with statistical and systematic uncertainties and the Standard Model expectation for the cross section (σ_{SM}). The value of σ_{SM} is given at the luminosity-weighted mean of \sqrt{s} for the data samples used and for a mean lepton beam polarisation of 0.	88
6.7	Cross section results using method no.2, described in Section 6.3.2. All other details as in Table 6.6.	89
6.8	Systematic uncertainties on the SM contribution to the selection of isolated electrons in e^-p (top) and e^+p data (bottom). Individual uncertainties are explained in Sec. 6.4. The second row shows the results of Section 6.2 with statistical errors only. The bottom row of each table shows the total uncertainty, i.e. the statistical error and the larger total systematic uncertainty (plus or minus) added in quadrature, which is the error that is used in the tables of Section 6.2.	101
6.9	Systematic uncertainties on the SM contribution to the selection of isolated electrons in $e^\pm p$ data. All other details as stated in the caption of Table 6.8.	102
6.10	Systematic uncertainties on the SM contribution to the selection of isolated muons in e^-p (top) and e^+p data (bottom). All other details as stated in the caption of Table 6.8.	103
6.11	Systematic uncertainties on the SM contribution to the selection of isolated muons in $e^\pm p$ data. All other details as stated in the caption of Table 6.8.	104
6.12	Systematic uncertainties on the SM contribution to the electron-channel of the cross section measurement in e^-p (top) and e^+p data (bottom). All other details as stated in the caption of Table 6.8.	105

6.13	Systematic uncertainties on the SM contribution to the electron-channel of the cross section measurement in $e^\pm p$ data. All other details as stated in the caption of Table 6.8.	106
6.14	Systematic uncertainties on the cross section measurements using method no.1 for the exclusive processes, in which the W decays to $e\nu_e$ (middle column) and $\mu\nu_\mu$ (right column). All other details as stated in the caption of Table 6.8.	106
6.15	Systematic uncertainties on the cross section measurements using method no.2 for the exclusive processes, in which the W decays to $e\nu_e$ (middle column) and $\mu\nu_\mu$ (right column). All other details as stated in the caption of Table 6.8.	107
6.16	Systematic uncertainties on the cross section measurements using method no.1 (top) and no.2 (bottom) for the inclusive cross sections in $e^+ p$ (left column), $e^- p$ (middle column) and $e^\pm p$ (right column). All other details as stated in the caption of Table 6.8.	108